1-1-2016

The Thermodynamics of Ligand Association and Molecular Recognition of Cationic and Metallated Porphyrins and Ruthenium Complexes with Model DNA Constructs

Jesse I. DuPont

The thermodynamics of ligand association and molecular recognition of cationic and metallated porphyrins and ruthenium complexes with model DNA constructs

By

Jesse Isaac DuPont

A Dissertation
Submitted to the Faculty of
Mississippi State University
in Partial Fulfillment of the Requirements
for the Degree of Doctor of Philosophy
in Chemistry
in the Department of Chemistry

Mississippi State, Mississippi

August 2016

The thermodynamics of ligand association and molecular recognition of cationic and metallated porphyrins and ruthenium complexes with model DNA constructs

By

Jesse Isaac DuPont

Approved:

_____

Edwin A. Lewis
(Major Professor)

_____

Joseph P. Emerson
(Committee Member)

_____

Nicholas C. Fitzkee
(Committee Member)

_____

Andrzej Sygula
(Committee Member)

_____

Keith T. Mead
(Committee Member)

_____

Stephen C. Foster
(Graduate Coordinator)

_____

Rick Travis
Interim Dean
College of Arts & Sciences

Name: Jesse Isaac DuPont

Date of Degree: August 12, 2016

Institution: Mississippi State University

Major Field: Chemistry

Major Professor: Edwin A. Lewis

Title of Study: The thermodynamics of ligand association and molecular recognition of cationic and metallated porphyrins and ruthenium complexes with model DNA constructs

Pages in Study 149

Candidate for Degree of Doctor of Philosophy

Molecular recognition, particularly as it applies to strong binding interactions between complementary ligand/receptor molecules in solution, is important in such varied areas as molecular biology, pharmacology, synthetic chemistry, and chemical detection. Strong binding is the additive result of a number of specific, weak, non-covalent interactions occurring between complementary molecules. This dissertation reports on the energetics of forming complexes between small molecules and model DNA constructs. Ligands included cationic and metallated cationic porphyrins and polyheterocyclic ruthenium compounds. DNA receptors included double stranded B-DNAs (hairpin and short linear sequences) as well G-quadruplex DNAs. Thermodynamic data were collected using isothermal titration calorimetry, circular dichroism spectropolarimetry, ultraviolet-visible spectroscopy, and mass spectrometry. The measured thermodynamic parameters included the changes in free energy, enthalpy and entropy for ligand/receptor complex formation as well as the stoichiometry of the stable complexes. The first section of this dissertation reports that the binding of cationic porphyrins to model G-quadruplex DNA may proceed through two pathways, end

stacking and intercalation. Modulating the number of pyridinium groups on a pyridinium substituted porphyrin yielded differing binding thermodynamics leading to the understanding that a balance of surface area, charge, and geometry affect the ability of a porphyrin to bind to G-quadruplex DNA. Further investigations into the binding of metallated porphyrins developed the understanding that the geometry of the central metal ion affected not only the thermodynamics but could also inhibit the intercalative mode. It was previously shown that the high affinity binding for binuclear polyheterocyclic ruthenium compounds proceeds through an intercalative mode. To further understand the binding process and the structure-function relationship of the ligand components, the binding of smaller mononuclear complexes that were representative of portions of the binuclear complex was examined in this dissertation. While limiting the intercalative ability lowered the binding affinity, the mononuclear complex with the full intercalating bridge was able bind to DNA with a higher affinity than the binuclear complex. These studies have been successful in part in determining the contributions of numerous weak interactions including: charge (Coulombic interactions), H-bonding, hydrophobic interactions, and solvent structure (solvation changes), to the overall energetics of this molecular recognition process. The first section of this dissertation reports that the binding of cationic porphyrins to model G-quadruplex DNA may proceed through two pathways, end stacking and intercalation. Modulating the number of pyridinium groups on a pyridinium substituted porphyrin yielded differing binding thermodynamics leading to the understanding that a balance of surface area, charge, and geometry affect the ability of a porphyrin to bind to G-quadruplex DNA. Further investigations into the binding of metallated porphyrins developed the understanding that the geometry of the central metal

ion affected not only the thermodynamics but could also inhibit the intercalative mode. It was previously shown that the high affinity binding for binuclear polyheterocyclic ruthenium compounds proceeds through intercalation. To further understand the binding process and the structure-function relationship of the ligand components, the binding of smaller mononuclear complexes that were representative of portions of the binuclear complex was examined in this dissertation. While limiting the intercalative ability lowered the binding affinity, the mononuclear complex with the full intercalating bridge was able bind to DNA with a higher affinity than the binuclear complex. These studies have been successful in part in determining the contributions of numerous weak interactions including: charge (Coulombic interactions), H-bonding, hydrophobic interactions, and solvent structure (solvation changes), to the overall energetics of this molecular recognition process.

DEDICATION

This dissertation is dedicated to my wife, Joy DuPont, and to my mother, Linda DuPont. Joy has been a constant support throughout my dissertation studies, even when I woke her up with 3 a.m. alarms to set up ITC experiments. Her selfless care of our daughter, Eleanor, allowed me to put in the extra time needed to finish my dissertation work.

Linda emphasized the importance of education and has been a source of encouragement and support throughout my studies. Her strength and persistence taught me to always push forward and strive for the best.

ACKNOWLEDGEMENTS

I would like to thank Dr. Gerald B. Rowland for his support and guidance during the initial phase of my graduate work. I would also like to thank Dr. Edwin A. Lewis for advising me during the remainder of my graduate studies and supporting my interest in drug binding in addition to organic chemistry. They both provided ample advice and encouragement when my research hit inevitable roadblocks.

I would also like to thank the professors on my committee, Drs. Emerson, Fitzkee, Mead, and Sygula, for the time they have spent advising my path and the reviews of my research they have performed. Dr. Emerson also helped a great deal throughout my studies and offered insightful thoughts during my metallated porphyrin research.

I owe a great deal of gratitude to Drs. Vu Le and Kate Henderson, who both guided me into the biophysical realm when I transitioned from organic synthesis. I would also like to thank Clinton Mikek for his help in the process and for becoming a great friend, even though I am faster on the draw with a pipette.

TABLE OF CONTENTS

LIST OF TABLES

LIST OF FIGURES

LIST OF SCHEMES

CHAPTER I

INTRODUCTION

1.1 Background

Cancer is the second most prevalent cause of death in the United States (1). The cellular basis for cancer, malignancy, occurs when damage to a cell's deoxyribonucleic acid (DNA) is greater than cellular repair ability. Primary views on the "hallmarks of cancer" established the following characteristics: sustaining proliferative signaling, enabling replicative immortality, inducing angiogenesis (formation of new blood vessels for the transport of nutrients), evading growth suppressors, resisting cell death, and activating invasion and metastasis (the spread of cancer from one location to another, e.g. liver to lung) (2). Recent "emerging hallmarks" have been added to the list: deregulating cellular energetics, avoiding immune destruction, genome instability and mutation, and tumor-promoting inflammation (3). While the emerging hallmarks have similarities to and basis in the seminal hallmarks, both groups offer insight into possible treatment mechanisms. As cancer is often caused by mutations within the genome, DNA offers an attractive target for therapies (4, 5).

1.2 Introduction to deoxyribonucleic acid (DNA)

DNA is possibly the most important aspect of an organism. This biomacromolecule codes for everything that an organism is or will become. The principal structure of DNA within a cell is that of its tertiary, double helical structure of

antiparallel strands as discovered by Watson and Crick (6). Hydrogen bonding between complementary purine and pyrimidine bases stabilizes this double helical structure (6, 7). The hydrogen bonding can primarily be seen between the purines adenine and guanine with the pyrimidines thymine and cytosine respectively. Three main types of DNA exist: A, B, and Z-form DNA (Figure 1.1). Of the three the most prevalent form of DNA, B-DNA, is most often used as a therapeutic target (8). Other, noncanonical intermolecular and intramolecular DNA structures are believed to exist *in vivo* including G-quadruplex, I-motif, triplex, hairpin, and cruciform DNA structures (9-11).

DNA has two primary responsibilities: replication, the semiconservative process by which two molecules of daughter DNA are formed from the parent DNA, as illustrated in Figure 1.2, and transcription, the process by which the DNA's coding is copied by messenger RNA (mRNA) to be translated into specific amino acid sequences to code for proteins, as illustrated in Figure 1.3 (9). Errors in either process may be phenotypically silent or may have dire consequences for the function of the organism and cause disease (3, 4). The binding of molecules to DNA is of intense interest in understanding the formation of diseases, as well as how to treat them (12). The sequence of the nucleotides that make up DNA allows distinct functional environments that influence the binding of other molecules to DNA, including environments that allow intercalation, negatively charged binding areas for cations, and grooves that allow for the burying of hydrophobic molecules away from water (5, 12, 13).

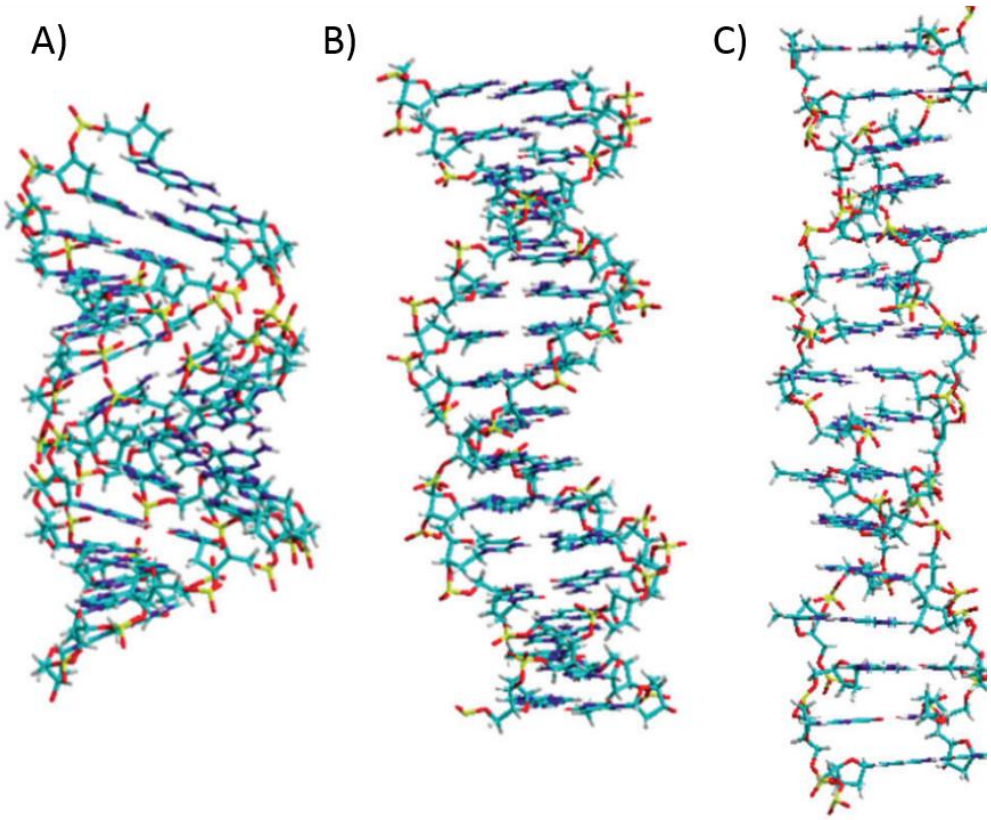

Figure 1.1 Stick structures of double helical DNA conformation.

Reproduced with permission from Wood, B. R., The importance of hydration and DNA conformation in interpreting spectra of cells and tissues. *Chemical Society Reviews* **2016** 45 (7) 1980-1998.
A) Stick diagram of A-DNA B) Stick diagram of B-DNA C) Stick diagram of Z-DNA. A-DNA is characterized by a widened minor groove relative to B-DNA and exhibits a complete turn every 11 base pairs, with base pairs being angled roughly 20 degrees from the axis perpendicular to the helical axis. The base pairs are separated with a distance of 2.55 Å. B-DNA exhibits a smaller minor groove and a larger major groove with 10.5 base pairs comprising a complete turn and a diameter of 20 Å. Distances between B-DNA base pairs are 3.4 Å. While A- and B-DNA are right handed, Z-DNA is characterized by a left handed double helical conformation with bases extending beyond the core of the helix and the presence of only one groove. One complete turn of Z-DNA comprises 12 base pairs with a 3.7 Å rise between base pairs and a helical diameter of 18 Å.

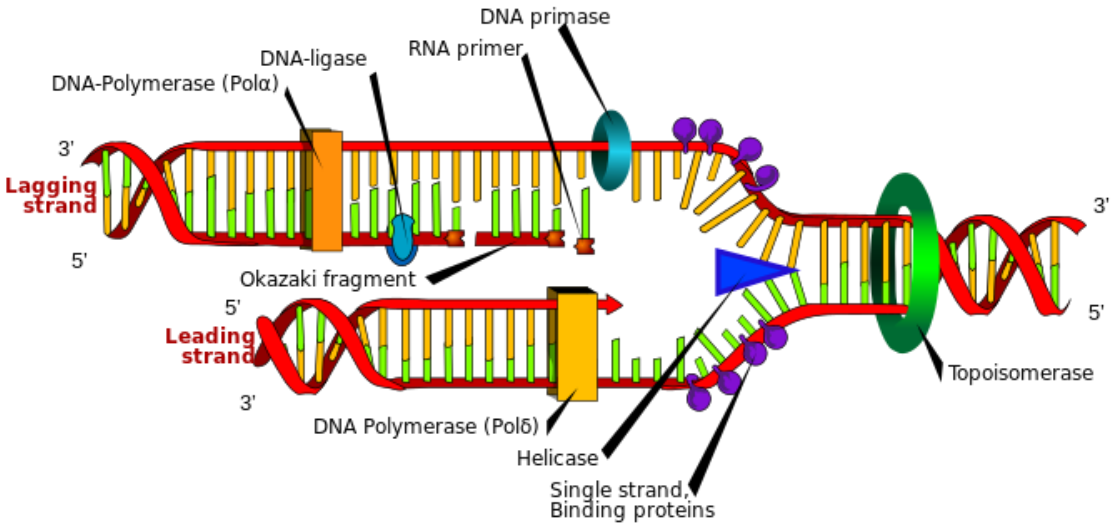

Figure 1.2 Model of the replication of DNA. Image created by Mariana Ruiz and is released to the public domain.

Topoisomerase causes a transient nicking of the DNA backbone to release the supercoil causing helical tension that occurs during replication. Helicase separates the lagging and leading strands as it propels itself forward along the strand. Single-strand DNA-binding (SSB) proteins bind to the single-stranded DNA directly behind the helicase, preventing the duplex from reforming. The SSB proteins bind without interfering with subsequent protein interactions. DNA polymerase polymerizes nucleotides in the 5' to 3' direction, using free mononucleotides as substrates for the leading strand, by addition of the 5' end of the nucleotide phosphate to the 3'-OH end of the deoxyribose. DNA primase introduces an RNA based primer on the lagging strand. DNA polymerase is then able to create Okazaki fragments in a 5' to 3' direction. Exonuclease, not pictured, removes the RNA primer. Additional Okazaki fragments are then formed further upstream. The 5' end of the former fragment is then joined with the 3'-OH of the newer fragment by DNA ligase. Through this semiconservative process, two new daughter strands are formed from the single parent template strand (9).

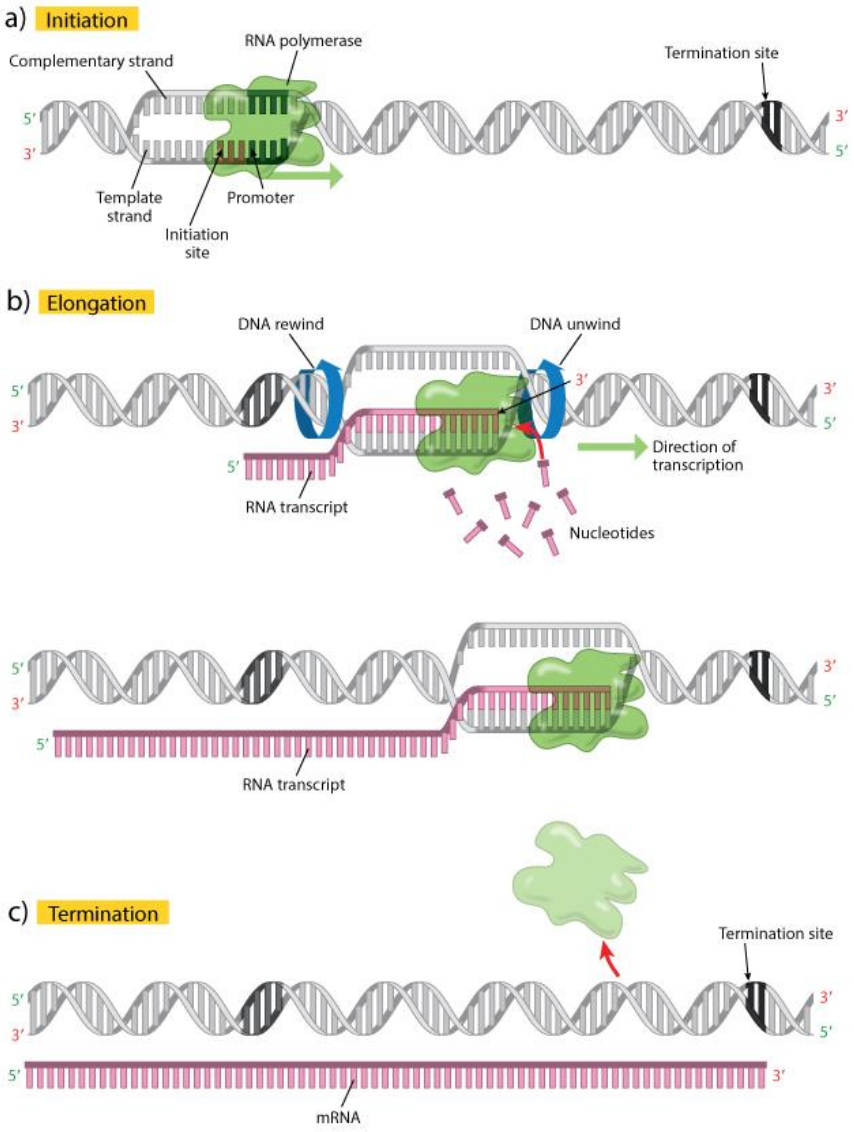

Figure 1.3 Model of the transcription of DNA into messenger RNA (mRNA).

Reused from Clancy, S., DNA transcription. Nature Education 2008, 1 (1:41) with permission (14).
A) Transcription factors bind to promoter regions upstream of the target DNA. RNA polymerase then binds at the initiation site of the template strand. B) RNA polymerase forms a transcription bubble by cleaving the hydrogen bonds which bind the two strands to each other. RNA polymerase proceeds down the DNA template strand in a 3' to 5' manner, matching ribonucleotides to the template strand and forming an RNA transcript strand in a 5' to 3' manner which matches the coding DNA strand complementary to the template strand. C) mRNA elongation ends when the polymerase extends to the termination site and the mRNA is separated from the template strand (14)

1.3 B DNA

DNA has several distinct conformations within the nucleus. However, for the bulk of therapies, double helical B-DNA provides several distinct possibilities as a target (15-17). Major grooves (22 Å wide) and minor grooves (12 Å wide) found in the phosphate backbone of DNA offer binding specificity, a feature that is exploited in DNA-protein binding (18). This specificity arises not only from steric constraints, but also from hydrogen bond acceptor and donor positioning among other intermolecular interactions, including π-stacking, halogen bonding, and cation-π interactions. The specific thymine-adenine and cytosine-guanine binding offers distinct differences in binding environments, as shown in Figure 1.4 (19).

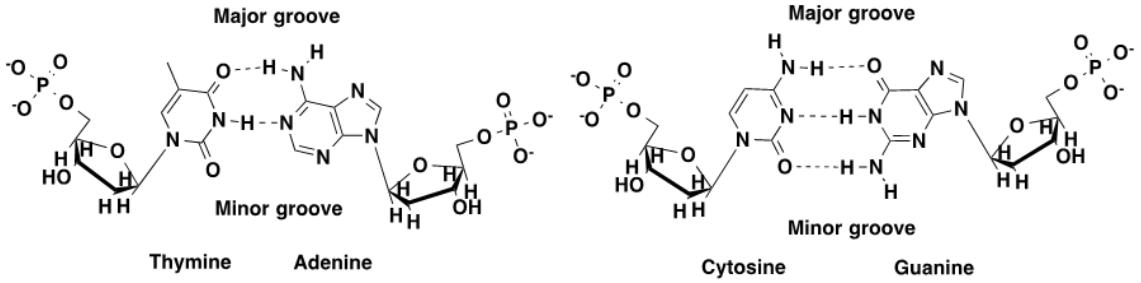

Figure 1.4 Diagram of the Watson-Crick base pairing of thymine with adenine and cytosine with guanine

Distinct functional environments are present in the major and minor grooves. The major groove displays a hydrogen bond acceptor at the O4 of thymine, donor at adenine N6 and acceptor at adenine N7. The minor groove exhibits a hydrogen bond acceptor at thymine O2 and adenine N3. This positioning of hydrogen bond acceptors and donors allows for some of the sequence specificity seen in DNA minor groove binding molecules

1.3.1 Alkylating agents

The first group of DNA targeting therapies in the modern era consisted of nitrogen mustards (12). These covalently modify DNA, offering inhibition of DNA processes and ultimately leading to cellular death. Their primary mechanism of action is alkylation of the N7 of guanine (5). This nitrogen is nucleophilic and able to react with the electron deficient carbon(s) of the mustard (5, 12). Further "generations" of alkylating/covalently modifying agents have involved transition metals, e.g. platinum in Cisplatin, a frontline cancer treatment. Cisplatin causes 1,2-intrastrand d(GpG) linkages through covalent modification of the N7 of guanine as the primary product, as shown in Figure 1.5 (20). The drawback of the majority of alkylating agents is their nonspecificity in targeting. Because of this, patients experience a myriad of side effects and even refuse treatment due to the negative effects of the drugs (21).

1.3.2 Minor groove binding agents

Advances in therapies have arisen through drugs that have sequence specificities or act solely on DNA (platins, mustards, and other alkylating agents are non-specific to DNA and are able to alkylate proteins and other intracellular and extracellular molecules) (5). Further research has evolved into numerous accounts of minor groove binding agents dependent on non-covalent interactions (5, 12, 19, 22-24). A large majority of these agents exhibit a characteristic "crescent shape" believed to enhance their ability to lie within the minor groove of DNA (5). In addition to the crescent shape, most minor groove binders are characterized by the presence hydrogen bond donors and acceptors, in addition to some amount of positive charge. The positive charge allows for favorable ionic interactions with the negative phosphate backbone (5, 12).

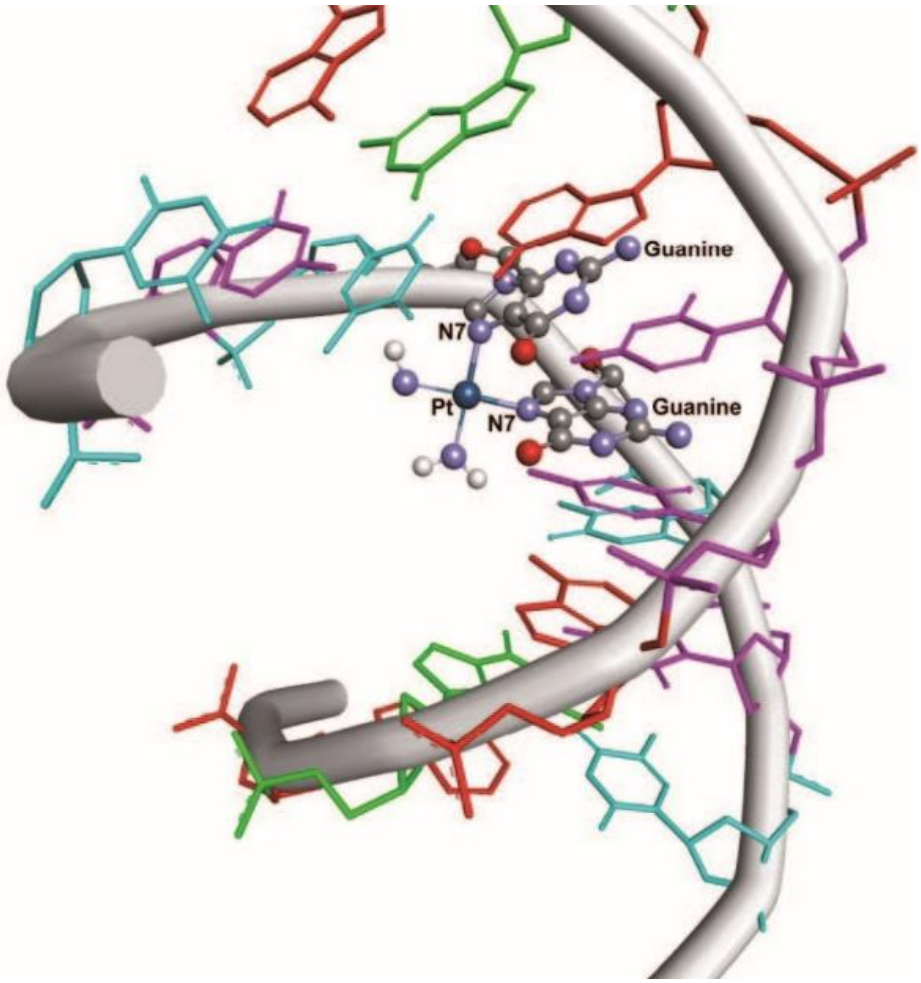

Figure 1.5 Crystal structure of the binding of cisplatin to DNA through the N7 position of adjacent guanines (1,2-intrastrand linkage).

Adapted with permission from Todd *et al.* (20).

Brostallicin, a polyamide, crescent shaped minor groove specific alkylating agent, shows specificity to 5'-AAAG-3' and alkylates the N3 of adenine. Brostallicin has an appreciable therapeutic index with an ED50 of 0.6-2 nM (as low as 0.46 nM in a cell line known for a high level of glutathione, a reducing agent commonly seen in hypoxic tumors). The binding affinity of Brostallicin for the minor groove of B-DNA arises from the hydrogen bond donating and accepting ability of secondary amides (hydrogen bond

donation from the amide proton and hydrogen bond accepting ability through a lone pair on the amide carbonyl oxygen) (15). Numerous studies have been performed on distamycin and related pyrrole polyamide crescent shaped minor grove binders that do not covalently modify DNA as Brostallicin does (5, 12, 19, 24, 25)

Thiazotropsin B, shown in Figure 1.6a is one such polyamide minor groove-binding drug. The polyamide skeleton gives crescent shape conformational ability as well as hydrogen bond acceptors and donors (16). Thiazotropsin B stabilizes dACGCGT to a greater extent than dACTAGT. Substitution of a pyrrole with imidazole and transformation of the aldehyde to a methyl ketone yields Thiazotropsin A, which has the reverse affinity for the two nucleotides (16, 19). This yields additional credence to the role of functional groups in base pair specificity. Additionally, Thiazotropsin B binding to DNA has a stoichiometry of 2:1 and binds in a "head to tail" directionality, as shown in Figure 1.6b. This is due to functional group association compatibility within the dimer formed from two Thiazotropsin B units. This binding mode increases the width of the minor groove. This binding driven widening of the minor groove compacts the major groove and offers allosteric inhibition of the binding of DNA binding proteins to the DNA major groove in this sequence, offering the potential of chemotherapeutic ability for this class of molecules (19).

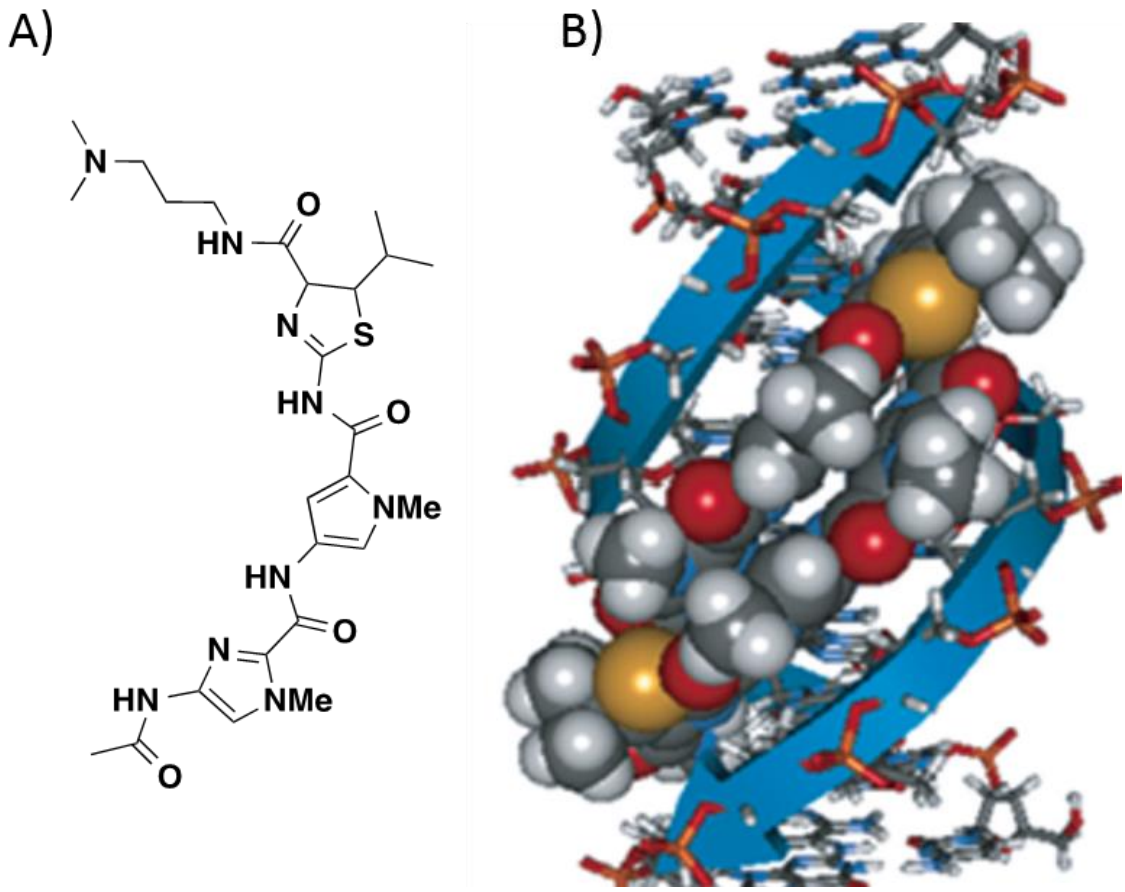

Figure 1.6 A) Structure of Thiazotropsin B. B) Cartoon of the solution structure for the 2:1 complex of Thiazotropsin B with d(CGACGCGTCG)$_2$. B) was reproduced with permission from Alniss *et al.* (2).

The two Thiazotropsin B ligands are self-associated as a dimer in a head to tail manner within the minor groove of the duplex. The presence of the ligand dimer causes substantial distortion of the duplex through widening of the minor groove and subsequent compaction and deepening of the major groove, which would allow for allosteric inhibition of protein binding to the major groove (2).

1.3.3 B-DNA intercalative agents

In addition to minor groove electrostatic interactions, molecules are able to intercalate between base pairs in several types of DNA, including B-form duplex DNA. The intercalation of molecules is due mostly to favorable π-π interactions. A planar,

conjugated molecule is able to insert into base pairs and exhibit π-orbital overlap with the planar, conjugated base pairs (12, 22).

Doxorubicin (Figure 1.7), another frontline drug, acts through this intercalative mode by selectively intercalating between cytosine and guanine, as shown in Figure 1.8 (22, 26). It also offers additional stabilization through hydrogen bonding from its amino sugar group to flanking base pairs, bonding to a cytosine deoxyribose and a thymine carbonyl. Binding to d(CGATCG) is tighter than that of d(CGTACG), where the thymine and adenine have been swapped. This specificity is believed to be due to the presence of the amino-sugar, and crystal structures support this hypothesis (22). Subtle differences in DNA configuration and ligand functional groups can have drastic changes in the binding ability of ligands; however, a major downfall to doxorubicin therapy is cardiomyopathy, which may arise due to the oxidative stress caused by the incomplete specificity in the action of doxorubicin (27, 28).

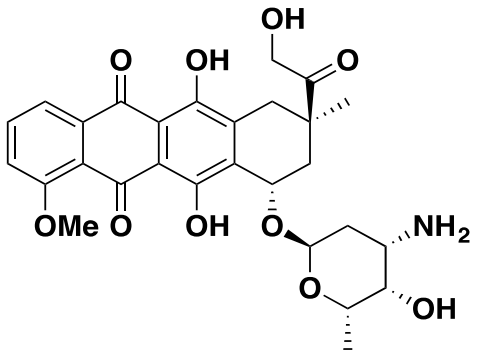

Figure 1.7 Chemical structure of doxorubicin.

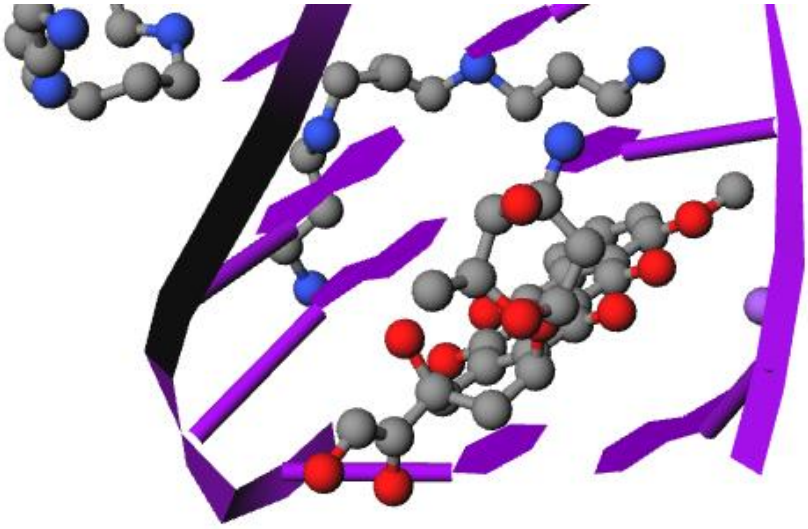

Figure 1.8 Crystal structure of the binding mode of doxorubicin with duplex DNA.

Adapted with permission from Frederick, C. A.; Williams, L. D.; Ughetto, G.; Van der Marel, G. A.; Van Boom, J. H.; Rich, A.; Wang, A. H. J., Structural comparison of anticancer drug-DNA complexes: adriamycin and daunomycin. *Biochemistry* **1990**, 29 (10), 2538-2549. 1990. American Chemical Society.
Association proceeds through intercalation between cytosine and guanine residues with additional stabilization from hydrogen bonding between the doxorubicin amino sugar and cytosine and thymine heteroatom.

1.4 G-quadruplex DNA

The G-quadruplex is a non-canonical four stranded DNA construct capable of forming from DNA sequences with high frequencies of guanine. G-quadruplexes offer an attractive therapeutic target as there are roughly 3.7 million guanine rich sequences within the human genome. These sequences occur in numerous areas including the c-MYC, BCL-2, KRAS, c-KIT, and VEGF oncogene promoter regions as well as the 3' overhang of DNA, the telomere (29).

The first report of guanine-guanine based associations was published by Ivar Bang in 1910 in which it was reported that millimolar concentrations of guanylic acid formed a gel (30). Further investigations demonstrated that self-assembly of guanylic

acids into tetrameric units able to form a helical structure was responsible for the gel-like properties (31). The link between guanylic acid gels and the formation of G-quadruplex structures from DNA was not made until Henderson *et al.* observed that guanine rich telomeric sequence oligonucleotides exhibited abnormally high stability under denaturing conditions (32). Since then, numerous investigations have shown through the use of G-quadruplex specific binding antibodies, as well as spectroscopic investigations, have shown that G-quadruplexes are able to form *in vitro* and are likely able to form *in vivo*, and are therefore a physiologically relevant target in drug therapies (29, 33-37).

G-quadruplexes are formed through non-Watson-Crick guanine-guanine based association. Hoogsteen hydrogen bonding among four separate guanine residues can form a square planar structure, a G-tetrad, shown in figure 1.9a (38). These tetrads are then able to self-assemble and stack through π-π stacking to form a G-quadruplex depending on the number of contiguous guanines within a sequence, as shown in Figure 1.9b. Monovalent cations present in the channel formed among the bases of the G-quadruplex offer additional stabilization and are often, at least in biologically relevant systems, sodium or potassium ions (39).

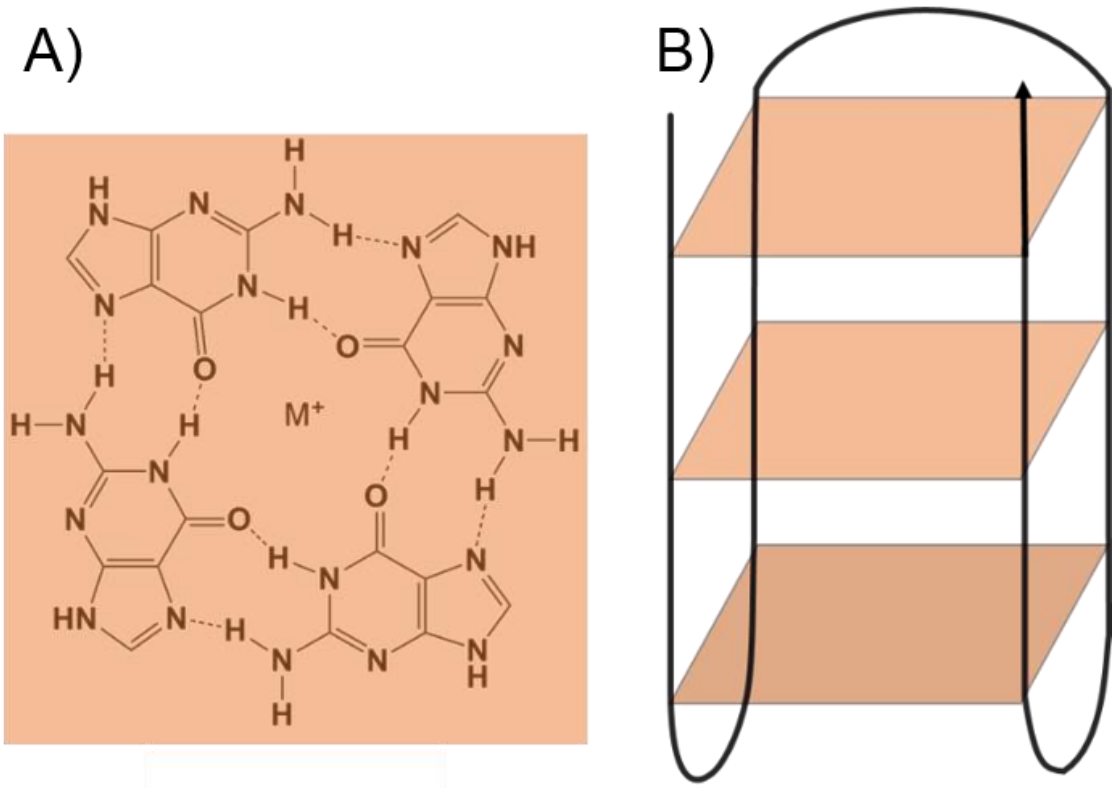

Figure 1.9 A) Chemical diagram of a G-tetrad. B) Simplistic cartoon of a G-quadruplex.

Hoogsteen hydrogen bonding among four guanine residues forms a square planar G-tetrad. G-tetrads are then able to form a G-quadruplex through π-π stacking. The presence of a monovalent metal ion in the central channel offers additional stabilization (39).

1.4.1 Quadruplex conformations and structural stability

G-quadruplex DNA is able to adapt a number of sequence orientations including parallel, antiparallel, and mixed conformations, as illustrated in figure 1.10 (38). Intramolecular and intermolecular G-quadruplexes can be formed, including unimolecular, bimolecular and tetramolecular structures. In general, G-quadruplexes formed in potassium solutions tend to favor a parallel conformation while G-quadruplexes formed in sodium solutions tend to form antiparallel G-quadruplexes, but

this is by no means the rule (40-42). The polymorphism of G-quadruplex structures in evident in that fact that in addition to the general trends, parallel G-quadruplexes may be seen in sodium solutions with antiparallel G-quadruplexes present in potassium solution.

Structural stability also varies as it is dependent upon not only the presence and identity of the cation present within the channel, but also on the number of nucleotides on both the 5' and 3' side of the structure as well as the number and composition of the nucleotides forming the loops within the complex. Higher concentrations of the supporting electrolyte help to stabilize the structure to a greater extent than lower concentrations. Dettler *et al.* reported that the first and second melting temperature for a 24 nucleotide long oligonucleotide c-MYC WT 24 mer (5'-TGGGGAGGGTGGGGAGGGTGGGGA-3') were 71.0 °C and 80.1 °C respectively in 30 mM K^+ and 78.8 °C and 93.1 °C respectively in 130 mM K^+ (44). Conversely, Blume *et al.* and other groups have reported that the presence of divalent cations causes a decrease in structural stability, even in the presence of potassium ions (45, 46).

1.4.2 Quadruplex binding ligands

G-quadruplexes may also be stabilized or destabilized by the presence of one or more bound small molecules that generally exhibit some type of conjugated or aromatic, planar core that is able to non-covalently bind to the G-quadruplex through π-π stacking. In addition to the conjugated or aromatic, planar core, a number of G-quadruplex binding small molecules also exhibit some degrees of cationic charge that is able to offer additional binding stability through ionic interactions with the negatively charged phosphate backbone of the G-quadruplex (47).

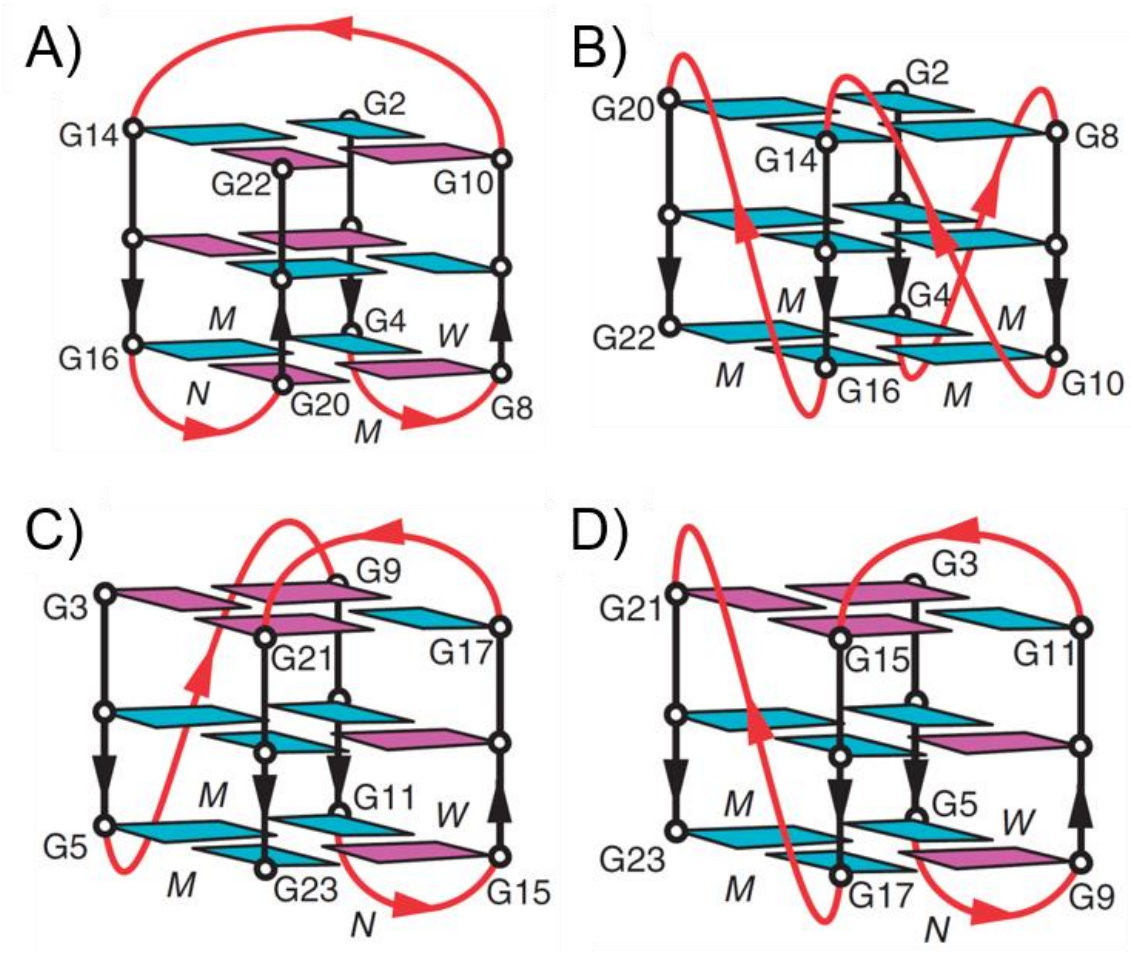

Figure 1.10 Diagram of the conformational heterogeneity possible with G-quadruplex structures. Reproduced from Phan *et al*. with permission (43).

The red lines in the figures represent the loops, cyan squares are syn- guanine residues and magenta colored squares are anti- oriented guanine residues. A) Figure for the conformation of residues 2 through 22 for d[AGGG(TTAGGG)$_3$] (hTel22) in Na^+ solution. B) Figure for the conformation of residues 2 through 22 for htel22 in K^+ crystal. C) Figure for the conformation of residues 3 through 23 for d[TAGGG(TTAGGG)$_3$] in K solution. D) Figure for the conformation of residues 3 through 23 for d[TAGGG(TTAGGG)$_3$TT] in K^+ solution (43).

Telomestatin (Figure 1.11a), a macrocycle first isolated from *Streptomyces anulatus*, inhibits the ability of telomerase to extend the TTAGGG telomeric repeat with an IC_{50} of 5 nM without interfering with DNA polymerase activity. The proposed mechanism of inhibition proceeds through the induction or stabilization of a basket type

antiparallel G-quadruplex with a 2:1 binding stoichiometry (2 equivalents of telomestatin to 1 equivalent of a 3 tetrad G-quadruplex) (48, 49). Diseleno sapphyrin (Figure 1.11c) binds to G-quadruplex DNA with a 1:1 stoichiometry and was found to convert preformed a preformed antiparallel basket type G-quadruplex to a hybrid, mixed parallel/antiparallel G-quadruplex (49). Braco-19 (Figure 1.11d), an aminoacridine based selective telomerase inhibitor, has been shown to cause growth inhibition in tumor cell lines as well as p21 and p53 mediated apoptosis (50).

TMPyP4 (Figure 1.11b), while not a serious drug candidate, has been extensively studied as a model G-quadruplex binding molecule and is the basis for many G-quadruplex binding studies. Han *et al.* found that binding of the cationic porphyrin proceeds via an *n+1* stoichiometry, where *n* is the number of tetrads present in a G-quadruplex (51). For a G-quadruplex containing three tetrads, the binding stoichiometry was found to be 4:1 (4 equivalents of TMPyP4 to 1 equivalent of a 3 tetrad G-quadruplex) and to proceed through two distinct binding modes. The first binding mode is driven by a favorable enthalpy change and proposed to be end-stacking, whereas the second mode is entropically driven and proposed to proceed through intercalation of the porphyrin between the tetrads of the G-quadruplex (52). Binding of TMPyP4 to a G-quadruplex forming sequence shifts the equilibrium between duplex and G-quadruplex formation for the binding of the G-quadruplex forming sequence to its complementary strand towards that of the G-quadruplex, effectively lowering the affinity of the G-quadruplex forming sequence for that of its complementary mate by 30% and slowing the rate constant for duplex formation by 32% (53).

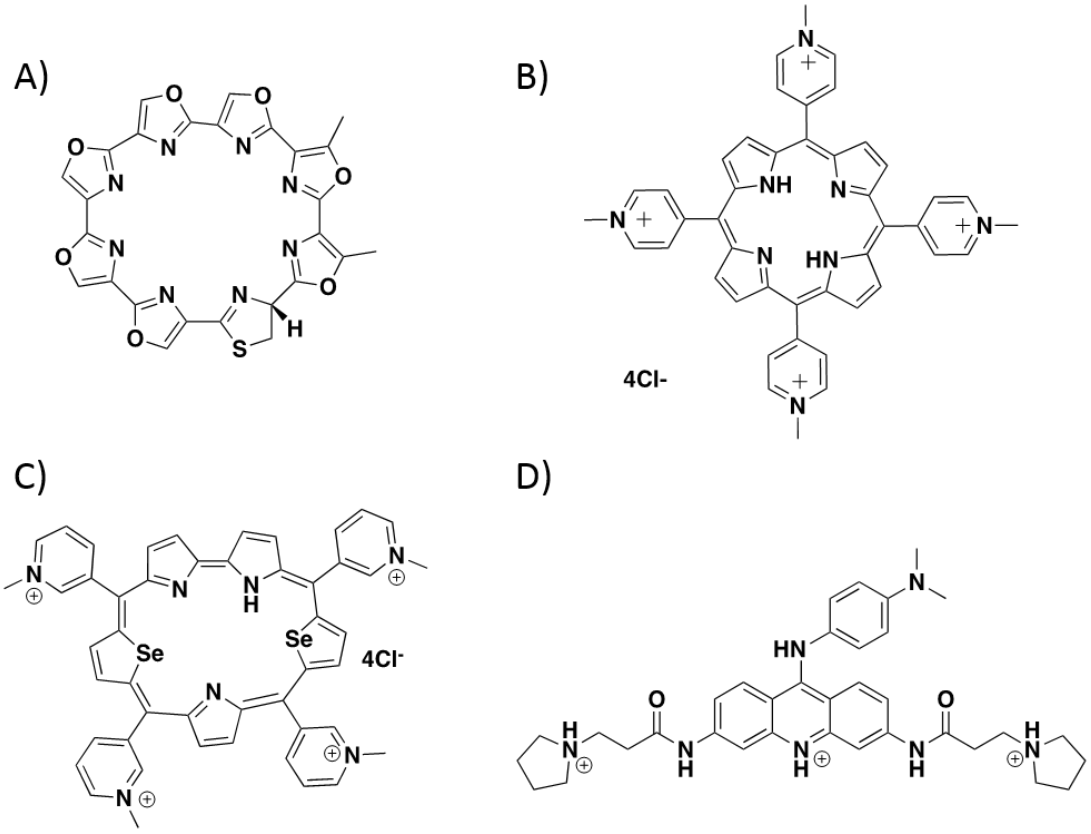

Figure 1.11 Chemical structures for the G-quadruplex interacting compounds: A) Telomestatin B) TMPyP4 C) Diseleno sapphyrin (Se_2SAP) D) Braco-19.

These G-quadruplex binding agents exhibit the general planar conjugated or aromatic core necessary for π-π stacking with the guanine residues of the quadruplex. Additionally TMPyP4, Se_2SAP, and Braco-19 display additional cationic charges that are able to offer additional binding stability through ionic interaction with the DNA's negatively charged phosphate backbone (47-53).

1.4.3 The implications of the interactions of G-quadruplex binding ligands with G-rich oncogenes

1.4.3.1 c-*MYC* NHE-III_1 G-quadruplex studies

The *c-MYC* proto-oncogene promoter c-*MYC* nuclease hypersensitivity element III_1 (c-*MYC* NHE III_1, Figure 1.12) is responsible for 80-90% of all *c-MYC* transcription (54). It is composed of a guanine (and complementary cytosine) rich sequence capable of

forming G-quadruplex (and complementary I-motif) structures located -142 to -145 base pairs upstream of the P_1 promoter and has been proposed as a chemotherapeutic target due to the overexpression of c-MYC in a variety of human cancer types including breast, colon, and ovarian cancers (55). The overexpression of c-MYC in malignant cells is precarious due to its role in regulating up to 15% of all gene expression (56). In the presence of c-MYC, genes already upregulated in tumor cells are amplified to a greater extent than gene with normal or low levels of expression (57).

The G-quadruplex forming ability of the c-*MYC* NHE III_1, region and its interactions with binding agents such as cationic porphyrins, has been investigated as a means by which to control c-MYC expression (44, 58-61). In fact TMPyP4 is able to suppress c-*MYC* transcription when the NHE-III_1 region is present, allowing it to act as a transcription silencing element. When the gene sequences lack the element, TMPyP4 does not suppress transcription, suggesting that G-quadruplex stabilizing compounds could potentially be effective chemotherapeutic agents (62).

Binding of TMPyP4 to a model c-*MYC* sequence (5'-GGGGAGGGTGGGGAGGGTGGGGAAGG-3') proceeds through two distinct binding modes, the first with an affinity of $5.4 * 10^6\ M^{-1}$ and the second with an affinity of $2.0 * 10^5\ M^{-1}$, as measured with isothermal titration calorimetry (ITC). Much like the TMPyP4 binding events discussed earlier, the stronger binding event is driven by a favorable change in entropy followed by a weaker event dependent on a favorable change in enthalpy and a binding stoichiometry of 2:1 for the first mode and 2:1 for the second mode. Titration experiments under varying salt concentrations show that as the concentration of the supporting electrolyte increases the binding affinity decreases (61).

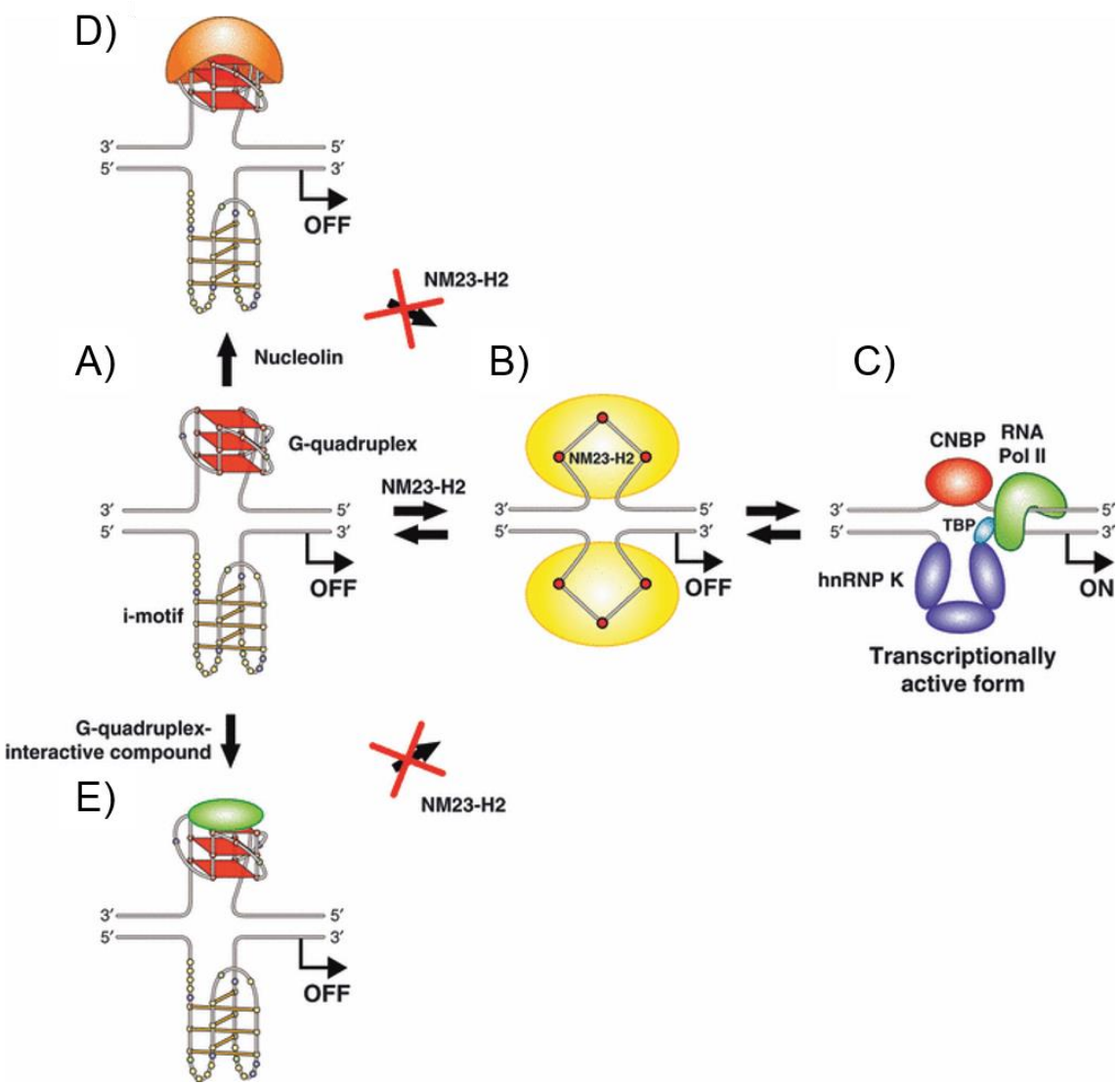

Figure 1.12 Cartoon diagram showing the route of c-*MYC* transcription silencing by G-quadruplex stabilizing compounds. Reproduced from Brooks *et al*. with permission (54).

A) The transcriptionally inactive form of the c-*MYC* NHE III_1 oncogene promoter region contains guanine and cytosine rich sequences which can form both G-quadruplex and I-motif structures, respectively. B) Resolution of the higher ordered DNA structures (G-quadruplex and I-Motif) by NM23-H2 allows c-*MYC* to transform into the transcriptionally active form. C) The transcriptionally active form allows for the binding of transcription factors to begin c-*MYC* transcription. D) A quadruplex binding protein such as nucleolin (shown in orange) is able to lock c-*MYC* NHE III_1 into the transcriptionally inactive form by binding to the G-quadruplex. E) G-quadruplex interactive compounds such as TMPyP4 can stabilize the c-*MYC* NHE III_1 G-quadruplex, also locking the promoter sequence in the transcriptionally inactive form (54).

1.4.3.2 *BCL*-2 G-quadruplex studies

B-cell lymphoma 2 (BCL-2) is an antiapoptotic protein coded for by the *BCL*-2 oncogene. Due to the overexpression of BCL-2 in number of cancers, malignant cells are less likely to undergo apoptosis in these cancers with upregulated antiapoptotic factors. This allows them to remain in a G_0 state until upregulated oncogenes, such as c-*MYC*, provide the necessary transcription factors to being replication (63). This BCL-2 upregulation has been proposed as a mechanism for the treatment resistance that often arises during treatment in certain cancer types. The presence of a G-quadruplex forming sequence in the promoter region, much like c-*MYC*, offers a potential chemotherapeutic target for the downregulation of *BCL*-2 compounds are able to interact with and stabilize the G-quadruplex (39).

Nagesh *et al.* has shown that TMPyP4 is able to interact with the *BCL*-2 promoter sequence G-quadruplex (5'-CGGGCGGGGGAGGAAGGGGGCGGGAGC-3') through two distinct modes. Mode I exhibits a binding affinity of $4.2 * 10^7$ M^{-1} and is driven by a favorable change in entropy, suggesting end stacking, while mode II proceeds with an affinity of $3.6 *10^5$ M^{-1} and is characterized by a favorable change in enthalpy, suggesting intercalation.

Planarity of the cationic porphyrin is necessary for optimum binding as reported by Le *et al.* It was found that the sterically induced non-planarity of the methyl pyridinium groups in TMPyP2 (Figure 1.13a) and TMPyP3 (Figure 1.13b) decreased the binding affinity of the porphyrin/G-quadruplex complex with respect to the planar TMPyP4. Additionally, the second binding mode of TMPyP4 (Figure 1.13c) type association was not seen in the TMPyP2 and TMPyP3 experiments (52). The single

binding mode seen for TMPyP3 and TMPyP2 associated proceeded through an entropically driven binding process, suggesting that the non-planarity of the ligands inhibits an intercalative binding mechanism (52, 64, 65).

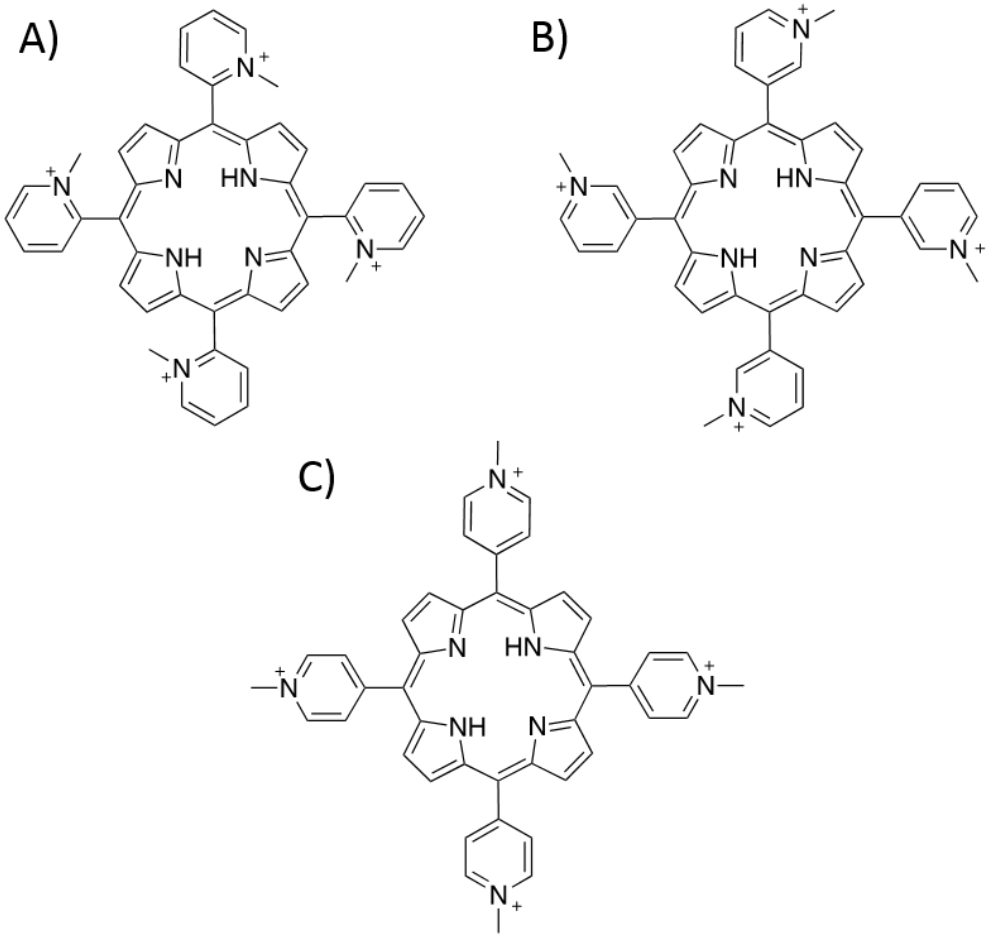

Figure 1.13 A) Chemical structure of TMPyP2. B) Chemical structure of TMPyP3. C) Chemical structure of TMPyP4.

1.5 Outline of this work

The work presented in this dissertation involved studying the binding of model DNA binding small molecules (ligands) with DNA constructs to further understand how

structural perturbations in model ligands affect the thermodynamics of the binding process. The thermodynamic studies presented in this dissertation primarily use isothermal titration calorimetry to analyze binding reactions to determine the full set of thermodynamic parameters associated with those reactions. Supplemental analytical techniques include UV-Vis and circular dichroism spectroscopies.

In Chapter 2, structural changes of a pyridinium substituted porphyrin core were investigated to determine charge, size, shape, and symmetry affect the thermodynamic parameters associated with the molecular recognition of planar aromatic molecules for G-quadruplex structures. This was performed by modulating the number or pyridinium groups on the porphyrin core. Cationic porphyrins of higher symmetry (TMPyP4 and A_2 trans) exhibited higher binding affinities against a model BCL sequence G-quadruplex when compared with porphyrins of lower symmetry (A_3 tris, A_2 cis, and A_1 mono).

Chapter 3 builds upon the study in Chapter 2 by investigating how substitution of metals into the porphyrin core would affect binding. Porphyrins containing Cu^{2+} and Ni^{2+} metal centers, with no or only weakly bound axial ligands, bound to a model human telomeric G-quadruplex with affinities equal to or greater than the unmetallated porphyrin, whereas the porphyrins containing Co^{3+} and Zn^{2+}, with one or two strongly bound axial ligands, exhibited markedly decreased binding affinities and lower saturation stoichiometries.

In Chapter 4, a series of cationic ruthenium containing polyheterocyclic molecules starting with a positively charged minor groove binder and leading to molecules with a greater intercalative abililty were investigated for their binding properties with B-DNA. It was found that $[Ru(phen)_2t(tatpp)]^{2+}$ exhibited a higher

binding affinity than $[(phen)_2Ru(tatpp)Ru(phen)_2]^{2+}$ for a model duplex, a likely source for the better IC_{50} exhibited by $[Ru(phen)_2t(tatpp)]^{2+}$.

These studies have been successful in part in determining the contributions of numerous weak interactions on the binding of ligands to model DNA constructs. The binding of porphyrins to G-quadruplex DNA was found to be greatly affected by charge, hydrophobic interactions, shape, symmetry, and solvent structure. Ruthenium(II) compounds were found to bind more tightly as the length of the intercalator increased (dependent on size, solvent accessible surface area, and π-bonding), but the additional charge of the second ruthenium center in the binuclear complexes actually caused a decrease in complex stability (dependent on charge and size).

1.6 References

1. Xu, J. Q. K., K. D.; Murphy, S. L., Mortality in the United States, **2012**. Statistics, N. C. f. H., Ed. 2014; Vol. 168.

2. Hanahan, D.; Weinberg, R. A., The Hallmarks of Cancer. *Cell* **2000**, 100 (1), 57-70.

3. Hanahan, D.; Weinberg, Robert A., Hallmarks of Cancer: The Next Generation. *Cell* **2011**, 144 (5), 646-674.

4. Alniss , H. Y.; Salvia, M.-V.; Sadikov, M.; Golovchenko, I.; Anthony, N. G.; Khalaf, A. I.; MacKay, S. P.; Suckling, C. J.; Parkinson, J. A., Recognition of the DNA Minor Groove by Thiazotropsin Analogues. *Chembiochem* **2014**, 15 (13), 1978-1990.

5. Puyo, S.; Montaudon, D.; Pourquier, P., From old alkylating agents to new minor groove binders. *Critical Reviews in Oncology/Hematology* **2014**, 89 (1), 43-61.

6. Watson, J. D.; Crick, F. H., Molecular structure of nucleic acids; a structure for deoxyribose nucleic acid. *Nature* **1953**, 171 (4356), 737-8.

7. Fonseca Guerra, C.; Bickelhaupt, F. M.; Snijders, J. G.; Baerends, E. J., Hydrogen Bonding in DNA Base Pairs: Reconciliation of Theory and Experiment. *Journal of the American Chemical Society* **2000**, 122 (17), 4117-4128.

8. Miyahara, T.; Nakatsuji, H.; Sugiyama, H., Helical Structure and Circular Dichroism Spectra of DNA: A Theoretical Study. *The Journal of Physical Chemistry A* **2013**, 117 (1), 42-55.

9. Alberts, B., DNA replication and recombination. *Nature* **2003**, 421 (6921), 431-5.

10. Kypr, J.; Kejnovská, I.; Renčiuk, D.; Vorlíčková, M., Circular dichroism and conformational polymorphism of DNA. *Nucleic Acids Research* **2009**, 37 (6), 1713-1725.

11. Potaman, V. N.; Sinden, R. R., DNA. In *DNA Conformation and Transcription*, Springer US: Boston, MA, 2005; pp 3-17.

12. Neidle, S.; Thurston, D. E., Chemical approaches to the discovery and development of cancer therapies. *Nature Reviews Cancer* **2005**, 5 (4), 285-296.

13. Alniss, H. Y.; Anthony, N. G.; Khalaf, A. I.; Mackay, S. P.; Suckling, C. J.; Waigh, R. D.; Wheate, N. J.; Parkinson, J. A., Rationalising sequence selection by ligand assemblies in the DNA minor groove: the case for thiazotropsin A. *Chemical Science* **2012**, 3 (3), 711-722.

14. Clancy, S., DNA transcription. *Nature Education* **2008**, 1 (1:41).

15. Lorusso, D.; Mainenti, S.; Pietragalla, A.; Ferrandina, G.; Foco, G.; Masciullo, V.; Scambia, G., Brostallicin (PNU-166196), a new minor groove DNA binder: preclinical and clinical activity. *Expert Opinion on Investigational Drugs* **2009**, 18 (12), 1939-1946.

16. Hampshire, A. J.; Khairallah, H.; Khalaf, A. I.; Ebrahimabadi, A. H.; Waigh, R. D.; Suckling, C. J.; Brown, T.; Fox, K. R., DNA sequence recognition by an imidazole-containing isopropyl-substituted thiazole polyamide (thiazotropsin B). *Bioorganic & Medicinal Chemistry Letters* **2006**, 16 (13), 3469-3474.

17. Fleming, F. F.; Yao, L.; Ravikumar, P. C.; Funk, L.; Shook, B. C., Nitrile-Containing Pharmaceuticals: Efficacious Roles of the Nitrile Pharmacophore. *Journal of Medicinal Chemist*ry **2010**, 53 (22), 7902-7917.

18. Wing, R.; Drew, H.; Takano, T.; Broka, C.; Tanaka, S.; Itakura, K.; Dickerson, R. E., Crystal structure analysis of a complete turn of B-DNA. *Nature* **1980**, 287 (5784), 755-758.

19. Alniss, H. Y.; Salvia, M. V.; Sadikov, M.; Golovchenko, I.; Anthony, N. G.; Khalaf, A. I.; MacKay, S. P.; Suckling, C. J.; Parkinson, J. A., Recognition of the DNA minor groove by thiazotropsin analogues. *Chembiochem* **2014**, 15 (13), 1978-90.

20. Todd, R. C.; Lippard, S. J., Structure of duplex DNA containing the cisplatin 1,2-$[Pt(NH3)_2]^{2+}$-d(GpG) cross-link at 1.77 A resolution. *Journal of inorganic biochemistry* **2010**, 104 (9), 902-8.

21. Frenkel, M., Refusing Treatment. *The Oncologist* **2013**, 18 (5), 634-636.

22. Frederick, C. A.; Williams, L. D.; Ughetto, G.; Van der Marel, G. A.; Van Boom, J. H.; Rich, A.; Wang, A. H. J., Structural comparison of anticancer drug-DNA complexes: adriamycin and daunomycin. *Biochemistry* **1990**, 29 (10), 2538-2549.

23. Stockert, J., Predictive Binding Geometry of Ligands to DNA Minor Groove: Isohelicity and Hydrogen-Bonding Pattern. In *Functional Analysis of DNA and Chromatin*, Stockert, J. C.; Espada, J.; Blázquez-Castro, A., Eds. Humana Press: **2014**; Vol. 1094, pp 1-12.

24. Uytterhoeven, K.; Sponer, J.; Van Meervelt, L., Two 1:1 binding modes for distamycin in the minor groove of d(GGCCAATTGG). *European Journal of Biochemistry* **2002**, 269 (12), 2868-77.

25. Nagle, P. S.; McKeever, C.; Rodriguez, F.; Nguyen, B.; Wilson, W. D.; Rozas, I., Unexpected DNA Affinity and Sequence Selectivity through Core Rigidity in Guanidinium-Based Minor Groove Binders. *Journal of Medicinal Chemistry* **2014**, 57 (18), 7663-7672.

26. Pérez-Arnaiz, C.; Busto, N.; Leal, J. M.; García, B., New Insights into the Mechanism of the DNA/Doxorubicin Interaction. *The Journal of Physical Chemistry B* **2014**, 118 (5), 1288-1295.

27. Octavia, Y.; Tocchetti, C. G.; Gabrielson, K. L.; Janssens, S.; Crijns, H. J.; Moens, A. L., Doxorubicin-induced cardiomyopathy: From molecular mechanisms to therapeutic strategies. *Journal of Molecular and Cellular Cardiology* **2012**, 52 (6), 1213-1225.

28. Minotti, G.; Menna, P.; Salvatorelli, E.; Cairo, G.; Gianni, L., Anthracyclines: Molecular Advances and Pharmacologic Developments in Antitumor Activity and Cardiotoxicity. *Pharmacological Reviews* **2004**, 56 (2), 185-229.

29. Balasubramanian, S.; Neidle, S., G-quadruplex nucleic acids as therapeutic targets. *Current Opinion in Chemical Biology* **2009**, 13 (3), 345-353.

30. Bang, I., Untersuchungen uber die Guanylsaure. *Biochemische Zeitschrif* **1910**, 26, 293-311.

31. Gellert, M.; Lipsett, M. N.; Davies, D. R., Helix formation by guanylic acid. *Proceedings of the National Academy of Sciences of the United States of America* **1962**, 48 (12), 2013-2018.

32. Henderson, E.; Hardin, C. C.; Walk, S. K.; Tinoco, I.; Blackburn, E. H., Telomeric DNA oligonucleotides form novel intramolecular structures containing guanine·guanine base pairs. *Cell* **1987**, 51 (6), 899-908.

33. Lipps, H. J.; Rhodes, D., G-quadruplex structures: *in vivo* evidence and function. *Trends in Cell Biology* 19 (8), 414-422.

34. Yuan, L.; Tian, T.; Chen, Y.; Yan, S.; Xing, X.; Zhang, Z.; Zhai, Q.; Xu, L.; Wang, S.; Weng, X.; Yuan, B.; Feng, Y.; Zhou, X., Existence of G-quadruplex structures in promoter region of oncogenes confirmed by G-quadruplex DNA cross-linking strategy. *Scientific Reports* **2013**, 3, 1811.

35. Henderson, A.; Wu, Y.; Huang, Y. C.; Chavez, E. A.; Platt, J.; Johnson, F. B.; Brosh, R. M.; Sen, D.; Lansdorp, P. M., Detection of G-quadruplex DNA in mammalian cells. *Nucleic Acids Research* **2014**, 42 (2), 860-869.

36. Rhodes, D.; Lipps, H. J., G-quadruplexes and their regulatory roles in biology. *Nucleic Acids Research* **2015**. *43* (18), 8627-37.

37. Salgado, G. F.; Cazenave, C.; Kerkour, A.; Mergny, J.-L., G-quadruplex DNA and ligand interaction in living cells using NMR spectroscopy. *Chemical Science* **2015**, 6 (6), 3314-3320.

38. Burge, S.; Parkinson, G. N.; Hazel, P.; Todd, A. K.; Neidle, S., Quadruplex DNA: sequence, topology and structure. *Nucleic Acids Research* **2006**, 34 (19), 5402-5415.

39. Patel, D. J.; Phan, A. T.; Kuryavyi, V., Human telomere, oncogenic promoter and 5′-UTR G-quadruplexes: diverse higher order DNA and RNA targets for cancer therapeutics. *Nucleic Acids Research* **2007**, 35 (22), 7429-7455.

40. Patel, P. K.; Hosur, R. V., NMR observation of T-tetrads in a parallel stranded DNA quadruplex formed by Saccharomyces cerevisiae telomere repeats. *Nucleic Acids Research* **1999**, 27 (12), 2457-2464.

41. Wang, Y.; Patel, D. J., Solution Structure of a Parallel-Stranded G-Quadruplex DNA. *Journal Molecular Biology* **1993**, 234 (4), 1171-1183.

42. Lim, K. W.; Ng, V. C. M.; Martín-Pintado, N.; Heddi, B.; Phan, A. T., Structure of the human telomere in Na^+ solution: an antiparallel (2+2) G-quadruplex scaffold reveals additional diversity. *Nucleic Acids Research* **2013**, 41 (22), 10556-10562.

43. Phan, A. T.; Kuryavyi, V.; Luu, K. N.; Patel, D. J., Structure of two intramolecular G-quadruplexes formed by natural human telomere sequences in K+ solution. *Nucleic Acids Research* **2007**, 35 (19), 6517-6525.

44. Dettler, Jamie M.; Buscaglia, R.; Le, Vu H.; Lewis, Edwin A., DSC Deconvolution of the Structural Complexity of c-MYC P1 Promoter G-Quadruplexes. *Biophysical Journal* **2011**, 100 (6), 1517-1525.

45. Blume, S. W.; Guarcello, V.; Zacharias, W.; Miller, D. M., Divalent Transition Metal Cations Counteract Potassium-Induced Quadruplex Assembly of Oligo(dG) Sequences. *Nucleic Acids Research* **1997**, 25 (3), 617-625.

46. Hardin, C. C.; Perry, A. G.; White, K., Thermodynamic and kinetic characterization of the dissociation and assembly of quadruplex nucleic acids. *Biopolymers* **2000**, 56 (3), 147-194.

47. Haq, I.; Trent, J. O.; Chowdhry, B. Z.; Jenkins, T. C., Intercalative G-Tetraplex Stabilization of Telomeric DNA by a Cationic Porphyrin. *Journal of the American Chemical Society* ***1999***, 121 (9), 1768-1779.

48. Shin-ya, K.; Wierzba, K.; Matsuo, K.-i.; Ohtani, T.; Yamada, Y.; Furihata, K.; Hayakawa, Y.; Seto, H., Telomestatin, a Novel Telomerase Inhibitor from Streptomyces anulatus. *Journal of the American Chemical Society* **2001**, 123 (6), 1262-1263.

49. Rezler, E. M.; Seenisamy, J.; Bashyam, S.; Kim, M.-Y.; White, E.; Wilson, W. D.; Hurley, L. H., Telomestatin and Diseleno Sapphyrin Bind Selectively to Two Different Forms of the Human Telomeric G-Quadruplex Structure. *Journal of the American Chemical Society* **2005**, 127 (26), 9439-9447.

50. Zhou, G.; Liu, X.; Li, Y.; Xu, S.; Ma, C.; Wu, X.; Cheng, Y.; Yu, Z.; Zhao, G.; Chen, Y., Telomere targeting with a novel G-quadruplex-interactive ligand BRACO-19 induces T-loop disassembly and telomerase displacement in human glioblastoma cells. *Oncotarget* **2016**, 7 (12), 14925-39.

51. Han, H.; Langley, D. R.; Rangan, A.; Hurley, L. H., Selective Interactions of Cationic Porphyrins with G-Quadruplex Structures. *Journal of the American Chemical Society* **2001**, 123 (37), 8902-8913.

52. Le, V. H.; Nagesh, N.; Lewis, E. A., Bcl-2 promoter sequence G-quadruplex interactions with three planar and non-planar cationic porphyrins: TMPyP4, TMPyP3, and TMPyP2. *PLoS One* **2013**, 8 (8), e72462.

53. Kumar, N.; Maiti, S., The effect of osmolytes and small molecule on Quadruplex–WC duplex equilibrium: a fluorescence resonance energy transfer study. *Nucleic Acids Research* **2005**, 33 (21), 6723-6732.

54. Brooks, T. A.; Kendrick, S.; Hurley, L., Making sense of G-quadruplex and i-motif functions in oncogene promoters. *FEBS Journal* **2010**, 277 (17), 3459-3469.

55. Wierstra, I.; Alves, J., The c-myc Promoter: Still MysterY and Challenge. In *Advances in Cancer Research*, Academic Press: **2008**; Vol. Volume 99, pp 113-333.

56. Gearhart , J.; Pashos , E. E.; Prasad , M. K., Pluripotency Redux — Advances in Stem-Cell Research. *New England Journal of Medicine* **2007**, 357 (15), 1469-1472.

57. Nie, Z.; Hu, G.; Wei, G.; Cui, K.; Yamane, A.; Resch, W.; Wang, R.; Green, Douglas R.; Tessarollo, L.; Casellas, R.; Zhao, K.; Levens, D., c-Myc Is a Universal Amplifier of Expressed Genes in Lymphocytes and Embryonic Stem Cells. *Cell* **2012** 151 (1), 68-79.

58. Grand, C. L.; Han, H.; Muñoz, R. M.; Weitman, S.; Von Hoff, D. D.; Hurley, L. H.; Bearss, D. J., The Cationic Porphyrin TMPyP4 Down-Regulates c-MYC and Human Telomerase Reverse Transcriptase Expression and Inhibits Tumor Growth in Vivo. *American Association for Cancer Research* **2002**, 1 (8), 565-573.

59. Cashman, D. J.; Buscaglia, R.; Freyer, M. W.; Dettler, J.; Hurley, L. H.; Lewis, E. A., Molecular modeling and biophysical analysis of the c-MYC NHE-III1 silencer element. *Journal of Molecular Modeling* **2008**, 14 (2), 93-101.

60. Dexheimer, T. S.; Carey, S. S.; Zuohe, S.; Gokhale, V. M.; Hu, X.; Murata, L. B.; Maes, E. M.; Weichsel, A.; Sun, D.; Meuillet, E. J.; Montfort, W. R.; Hurley, L. H., NM23-H2 may play an indirect role in transcriptional activation of c-myc gene expression but does not cleave the nuclease hypersensitive element III_1. *American Association for Cancer Research* **2009**, 8 (5), 1363-1377.

61. Freyer, M. W.; Buscaglia, R.; Kaplan, K.; Cashman, D.; Hurley, L. H.; Lewis, E. A., Biophysical Studies of the c-MYC NHE III_1 Promoter: Model Quadruplex Interactions with a Cationic Porphyrin. *Biophysical Journal* **2007**, 92 (6), 2007-2015.

62. González, V.; Hurley, L. H., The c-MYC NHE III1: Function and Regulation. *Annual Review of Pharmacology and Toxicology* **2010**, 50 (1), 111-129.

63. Vaux, D. L.; Cory, S.; Adams, J. M., Bcl-2 gene promotes haemopoietic cell survival and cooperates with c-myc to immortalize pre-B cells. *Nature* **1988**, 335 (6189), 440-442.

64. Nagesh, N.; Sharma, V. K.; Ganesh Kumar, A; and Lewis, E. A. Effect of Ionic Strength on Porphyrin Drug Interactions with Quadruplex DNA Formed by the Promoter Region of c-MYC and Bcl-2 Oncogenes. *Journal of Nucleic Acids*, **2009**, doi:10.4061/2010/146418.

65. Nagesh, N., Buscaglia, R., Dettler, J.M. and Lewis, E.A. Studies on the Site and Mode of TMPyP4 Interactions with Bcl-2 Promoter Sequence G- Quadruplexes. *Biophysical Journal*, **2010**, 98, 2628-2633.

CHAPTER II

THE EFFECT OF PYRIDYL SUBSTITUENTS ON TH ETHERMODYNAMICS OF PORPHYRIN BINDING TO G-QUADRUPLEX DNA

Previously published in *Bioorganic & Medicinal Chemistry* **2013**, 21, 7515-7522 and reproduced with permission.

2.1 Abstract

Most of the G-quadruplex interactive molecules reported to date contain extended aromatic flat ring systems and are believed to bind principally by π-π stacking on the end G-tetrads of the quadruplex structure. One such molecule, **TMPyP4**, (5,10,15,20-tetra(*N*-methyl-4-pyridyl)porphyrin), exhibits high affinity and some selectivity for G-quadruplex DNA over duplex DNA. Although not a realistic drug candidate, TMPyP4 is used in many nucleic acid research laboratories as a model ligand for the study of small molecule G-quadruplex interactions. This work reports on the synthesis and G-quadruplex interactions of four new cationic porphyrin ligands having only 1, 2, or 3 (N-methyl-4- pyridyl) substituents. The four new ligands are: **P(5)** (5-(*N*-methyl-4-pyridyl)porphyrin), **P(5,10)** (5,10-di(*N*-methyl-4-pyridyl)porphyrin), **P(5,15)** (5,15-di(*N*-methyl-4-pyridyl)porphyrin), and **P(5,10,15)** (5,10,15-tri(*N*-methyl-4-pyridyl)porphyrin). Even though these compounds have been previously synthesized, alternative synthetic routes that are more efficient and that result in higher yields were utilized. ITC, CD, and ESI-MS were used to explore the effects of the number of *N*-methyl-4-pyridyl

substituents and the substituent position on the porphyrin on the G-quadruplex binding energetics. The relative affinities for binding these ligands to the WT Bcl-2 promoter sequence G-quadruplex are: $K_{TMPyP4} \approx K_{P(5,15)} > K_{P(5,10,15)} >>> K_{P(5,10)}, K_{P(5)}$. The saturation stoichiometry is 2:1 for both **P(5,15)** and **P(5,10,15),** while neither **P(5)** nor **P(5,10)** exhibit significant complex formation with the WT Bcl-2 promoter sequence G-quadruplex. Additionally, binding of **P(5,15)** appears to interact by an *"intercalation mode"* while **P(5,10,15)** appears to interact by an *"end-stacking mode"*.

2.2 Introduction

Over expression of BCL-2 has been observed in a number of cancers including: breast, prostate, cervical, colorectal, and lung carcinoma (1). The human *BCL*-2 P1 promoter region is GC-rich and the G-rich strand is known to form a stable G-quadruplex structure (2). The stabilization of oncogene promoter sequence G-quadruplexes and telomere overhang repeat sequence G-quadruplexes by binding small molecules (e.g. ligands or drugs) is a subject of interest in cancer drug discovery. Ligands exhibiting structural recognition (selectivity) and high affinity for G-quadruplex DNA including several porphyrin based compounds have been explored for their potential as anti-cancer drugs (3-6). The porphyrin-based ligands have shown the ability to inhibit telomerase and they typically exhibit low cytotoxicity (5, 6). **TMPyP4**, (5,10,15,20-tetra(*N*-methyl-4-pyridyl)porphyrin), while not a serious drug candidate, has been used extensively as a model ligand in the characterization of the structure, stability, and ligand binding properties of oncogene promoter sequence G-quadruplexes (5-14).

The Lewis group has published several studies on the interactions of TMPyP4 with several oncogene promoter sequence G-quadruplexes including c-*MYC*, *BCL*-2, and *K-ras* (7-11). The Lewis group has also shown that that TMPyP4 binding to these G-quadruplexes results in a complex having 4 moles of TMPyP4 per mole of quadruplex and that the complex is stabilized significantly over the naked G-quadruplex. TMPyP4 binds to these G-quadruplexes by two distinctly different binding modes, a higher affinity mode which is driven by a favorable entropy change and a weaker mode which is accompanied by an unfavorable entropy change. We believe that these two modes represent first the end-binding of two moles of TMPyP4 followed by the intercalation of another two moles of TMPyP4 so that every G-tetrad is sandwiched between two planar porphyrin molecules. Le *et al.* recently reported on a study of the interactions of three related porphyrins, (TMPyP2, TMPyP3, and TMPyP4), with a WT 39-mer Bcl-2 promoter sequence G-quadruplex (7). Using CD, Fluorescence, ITC, and ESI-MS, it was shown that as the substituted porphyrin becomes non-planar, the intercalation binding mode is eliminated so that the saturation stoichiometry for binding TMPyP2 or TMPyP3 becomes 2:1 (15). In addition, the end-stacking mode is also weakened as the porphyrin ligand becomes increasingly less planar with the binding of TMPyP2 << TMPyP3. TMPyP4 like many other G- quadruplex interactive ligands reported to date are planar heterocyclic aromatic ring systems (16-25). The porphyrin ligand charge (e.g. +1, +2, +3, or +4), size (e.g. SASA (solvent accessible surface area)), shape (e.g. planarity) and symmetry (e.g. substitution pattern) may all play a role in establishing the selectivity and affinity for G-quadruplex complex formation. This study has begun to explore each of these effects by synthesizing new ligands that are systematically reduced in size, charge,

and symmetry in comparison to TMPyP4. The new ligands differ from the model TMPyP4 quadruplex interactive compound by having only one, two, or three (*N*-methyl-4-pyridyl) substituents.

ITC, CD, and ESI-MS were used to study the interactions of these new porphyrin ligands with a 27-mer WT *BCL*-2 P1 promoter sequence G-quadruplex. Although Goncalves *et al.* has already reported the synthesis for the **P(5)** (5-(*N*-methyl-4-pyridyl)porphyrin), **P(5,10)** (5,10-di(*N*-methyl-4-pyridyl)porphyrin), **P(5,15)** (5,15-di(*N*-methyl-4-pyridyl)porphyrin), and **P(5,10,15**) (5,10,15-tri(*N*-methyl-4-pyridyl)porphyrin) compounds (26), this work presents alternative synthetic routes that are more efficient and that result in higher yields. Goncalves *et al.* also reported SPR experiments from which they estimated the binding affinities for these same four ligands with a human telomere repeat sequence G-quadruplex (26). In these experiments, the G-quadruplex is different, but even more importantly, the complete set of thermodynamic parameters for the formation of these four porphyrin ligand complexes with a typical oncogene promoter sequence G-quadruplex have been determined. The ITC, CD, and ESI-MS data reported here have been analyzed to yield values for the free energy changes (ΔG), the enthalpy changes (ΔH), the entropy changes ($-T\Delta S$), and the saturation stoichiometry (n) for the formation of the WT *BCL*-2 27-mer P1 promoter sequence G-quadruplex complexes with **P(5), P(5,10), P(5, 15)** and **P(5,10,15)**.

2.3 Materials and Methods

2.3.1 Binding studies

The WT 27-mer *BCL*-2 oligonucleotide used in this study was obtained from Midland Oligos (Midland, TX). The oligonucleotide has the following sequence 5'-

CGG GCG CGG GAG GAA GGG GGC GGG AGC -3'. DNA stock solution was prepared by reconstituting the lyophilized oligonucleotide into KBPES buffer with a salt concentration of 130 mM [KCl] and a pH of 7.0. Approximately 2 mL of the oligonucleotide was dialyzed (1000 MW cutoff membrane) against three changes of buffer solution (1 L, 24 h each) at 4 °C. The concentrations of stock DNA solution were verified using UV-Vis. DNA was annealed by quickly heating the sample to 100 °C, holding at 100 °C for ten minutes then slowly cooling to 5 °C over a three hour period. The molar extinction coefficient of the DNA was determined using a nearest-neighbor method for single stranded DNA (27). The extinction coefficient at 260 nm for the WT 27-mer Bcl-2 sequence was: 2.26×10^5 M^{-1} cm^{-1}.

CD experiments were performed with an Olis DSM-20 spectropolarimeter (Bogart, GA). All measurements were done at 25 °C using a 1 cm quartz cuvette and covering a spectral range of 225-325 nm. All CD samples were prepared such that they had a nominal absorbance of less than 1.0 at 260 nm.

ITC experiments were performed using a VP-ITC calorimeter (GE-Healthcare). A typical ITC experiment involved the addition of 28 (10 μL) injections of a dilute (115 μM) WT 27-mer Bcl-2 DNA solution into ~ 1.5 mL of a dilute porphyrin solution (5 μM). Reverse titrations were employed because of the low solubility of the substituted porphyrins. Three replicate experiments were done for each of the four porphyrins. Blank titrations were done by injecting the titrant (115 μM G-quadruplex) into buffer solution. Corrected titration curves were achieved by subtracting the blank titration data from the ITC data for the porphyrin-DNA titrations. Corrected ITC titrations were fit with a

nonlinear regression algorithm again using the CHASM© ITC data analysis program developed in the Lewis laboratory (28).

ESI-MS experiments on *BCL*-2 and the *BCL*-2 porphyrin complexes were carried out on a Bruker MicrOTOFQ mass spectrometer. Data acquisition was set to operate in negative ion mode. All experiments were performed in 50 mM ammonium acetate buffer (pH = 7.0) containing 20% HPLC grade methanol. The WT Bcl-2 27-mer G-quadruplex sample was prepared at a concentration of approximately 25 μM in the ammonium acetate buffer and was dialyzed against three changes of buffer 12 hours each at 4 °C. Stock solutions of the porphyrin ligands were prepared in the final dialysate buffer at concentration as high as 50 μM. The ESI-MS samples were prepared by mixing the DNA and ligand stock solutions to yield a mixture containing 4 equivalents of each porphyrin ligand per equivalent of DNA. The MS capillary voltage was set to +3500 V, dry N_2 gas flow was adjusted to 0.5 L/min at 110°C, and the G-quadruplex/porphyrin samples were directly infused into the MS by using a kD Scientific syringe pump set to a flow rate of 200 μL/hour. Data processing was performed by using Bruker Daltonics Data Analysis program.

2.3.2 Porphyrin ligand synthesis

The overall synthesis for the four porphyrin ligands studied here is shown in Scheme 2.1. The synthesis of the substituted porphyrins began by synthesizing the key dipyrromethane building blocks **1** and **4** by condensation of the respective aldehydes with pyrrole (29, 30). Formylation of **1** utilizing a Vilsmeier reaction gave compound **2** in 45% yield (26). Functionalized dipyrromethane **5** was synthesized by the

diformylation of pyridyl dipyrromethane **4** also utilizing a Vilsmeier reaction in 28% yield (26). The reduction of formylated dipyrromethane **5** with sodium borohydride provided compound **6,** which was used in subsequent steps without purification (26).

With the key building blocks in hand, the synthesis was directed to the desired porphyrin analogues. The synthesis of **P(5)** was accomplished by the condensation of dipyrromethanes **1** and **6** in the presence of trifluoroacetic acid. The resulting mixture was allowed to stir for one hour, oxidized with DDQ, and treated with triethylamine to provide porphyrin **7** in 8% yield. Methylation of **7** with iodomethane followed by washing with ether provided **P(5)** in 16% yield (26).

The synthesis of **P(5,10)** was accomplished by deprotonation of compound **6** with ethyl magnesium bromide followed by the addition of Mukiyama reagent **8** resulted in the formation of compound **9** in 41% yield (31). The condensation of compounds **2** and **9** resulted in the formation of porphyrin **10** in 35% yield (32). Methylation of **14** provided the **P(5,10)** in 6% yield (26).

Porphyrin **P(5,15)** was synthesized by the condensation of compound **4** with trimethyl orthoformate **11** followed by methylation provided **P(5,15)** in 2% overall yield. Condensation of compounds **3**, **4**, and **11** followed by methylation resulted in the formation of porphyrin **P(5,10,15)** (26).

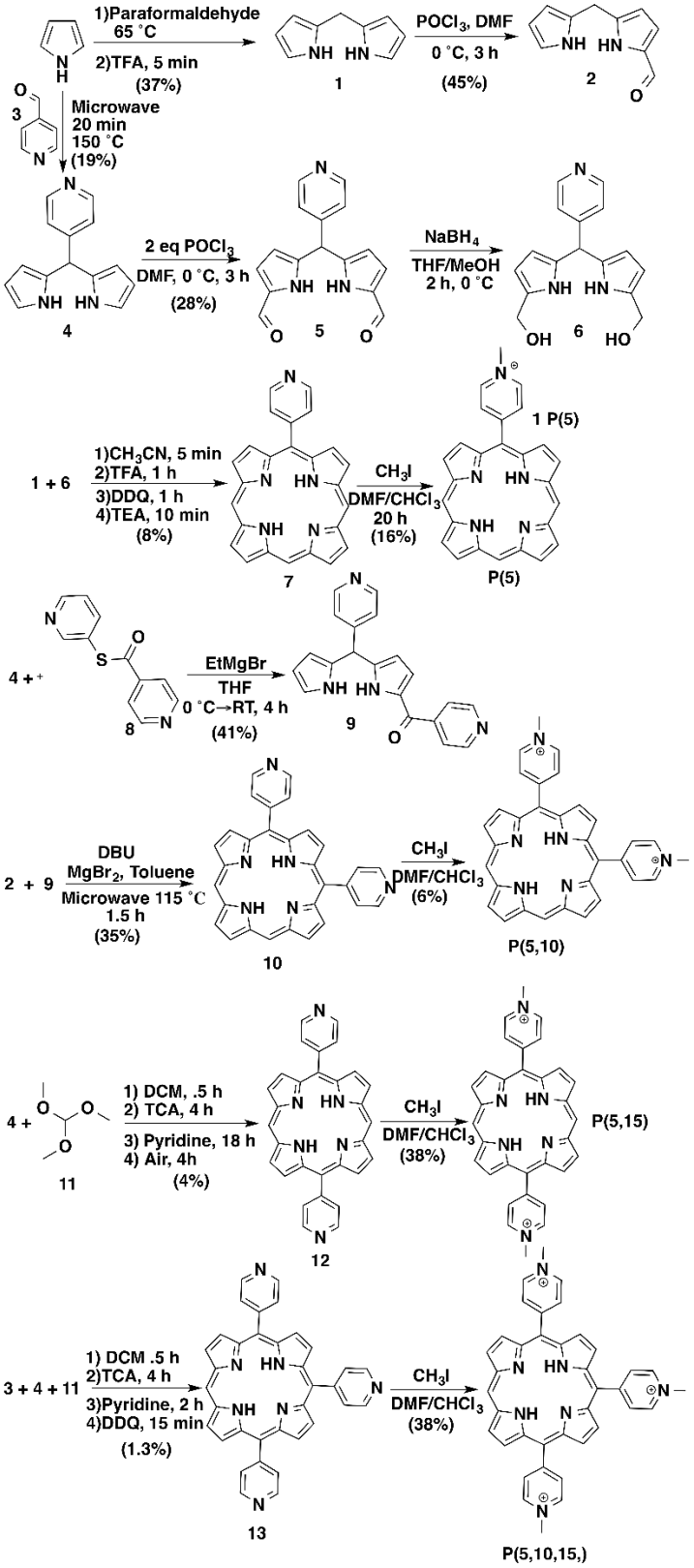

Scheme 2.1 Synthetic routes for the four cationic porphyrin ligands used in this study

2.3.2.1 Dipyrromethane 1 (30):

Paraformaldehyde (1.73g, 57.7mmol) and pyrrole (100mL, 1.44 mol) were added to a 250mL two-necked round-bottom flask equipped with a condenser and an internal thermometer. The mixture was brought to an internal temperature of 65 °C. The flask was removed from the heat and TFA (444 μL, 5.77 mmol) was added. The mixture was purified via flash chromatography eluting at 8-10% EtOAc in hexanes affording 3.17g of **1** as a white solid in 37% yield. ^{1}H NMR (300MHz, DMSO-d6): δ = 3.807 (s, 2H), 5.744 (s, 2H), 5.884-5.893 (d, 2H), 6.583 (s, 2H), 10.502 (br s, 2H).

2.3.2.2 1-formyl dipyrromethane 2 (26):

DMF (24.2 mmol, 1.9 mL) was added to a dry RBF and cooled to 0 °C. $POCl_3$ (0.3 mL, 3.01 mmol) was added drop wise and stirred for 10 min to yield the Vilsmeier reagent. In another dry RBF, dipyrromethane **1** (0.500 g, 3.42 mmol) was dissolved in DMF (7.5 mL) under argon and cooled to 0 °C. To the reaction mixture, the freshly prepared Vilsmeier reagent (1.9 mL, 3.36 mmol,) was added drop wise and stirred at 0 °C for 2 h. After 2 h, a biphasic solution of ethyl acetate (50 mL) and saturated aqueous sodium acetate (50 mL) was added and stirred at room temperature for 4 h. Ethyl acetate was separated and the aqueous layer was extracted three times with ethyl acetate and the combined organic layer was washed with brine and water, dried over anhydrous Na_2SO_4 and evaporated *in vacuo* to get crude product. The desired compound was isolated using automated flash chromatography, eluting at 20% EtOAc in DCM and evaporate *in vacuo* to yield **2** as a pale yellow solid (270 mg, 45.2%). ^{1}HNMR (300 MHz, DMSO-d_6): δ = 11.93 (br s, 1H), 10.606 (br s, 1H), 9.328 (s, 1H), 6.867-6.887 (m, 1H), 6.602-6.607 (m, 1H), 5.98-5.999 (m, 1H), 5.866-5.892 (m, 1H), 5.765 (br s, 1H), 3.868 (s, 2H) ppm.

2.3.2.3 5-(4-pyridyl) dipyrromethane 4 (29):

4-pyridylcarboxaldehyde **3** (1.5mL, 16.4 mmol) and pyrrole (16mL, 230 mmol) were added to a microwave vial. The vial was sealed under argon and stirred for 20 min at 150 °C. The reaction mixture was cooled and concentrated under reduced pressure to yield a dark red liquid which was left on high vacuum overnight to yield a dark oil. The oil was dissolved in minimal DCM and wet-loaded onto a Biotage 50G column, packed with alumina oxide and purified via flash chromatography with DCM: EtOAc. Fractions containing product were collected and concentrated under vacuum. Minimal DCM was added to the resulting solid to create a slurry. Excess hexanes were added and the mixture was filtered, collecting **4** as a pale grey solid (645.1mg, 18.9% yield). ^{1}H NMR (300MHz, $CDCl_3$): δ = 5.541 (s, 1H), 5.874 (s, 2H), 6.168-6.197 (q, 2H), 6.738-6.761 (q, 2H), 7.313-7.340 (d, 2H), 7.599-7.627 (d, 2H), 7.973 (br s, 2H).

2.3.2.4 1,9-Diformyl-5-(4-pyridyl)dipyrromethane 5 (26):

The procedure of 1-formyldipyrromethane **2** was followed with DMF (6 mL, 58 mmol), $POCl_3$ (0.9 mL, 9.66 mmol) and replacing the dipyrromethane with 5-(4-pyridyl) dipyrromethane **4** (0.300 g, 1.34 mmol). The desired compound was isolated using automated flash chromatography, eluting at 9% MeOH in DCM and concentrated in vacuo to yield **5** as a brown oil (0.103 g, 28%). ^{1}HNMR (300 MHz, $CDCl_3$), δ = 10.96 (br s, 2H), 9.24 (s, 2H), 8.58 (d, J = 5.1 Hz, 2H), 7.28 (d, J = 5.1 Hz, 2H), 6.91 (s, 2H), 6.09 (s, 2H) and 5.60 (s, 1H) ppm.

2.3.2.5 (5,5'-(pyridine-4-ylmethylene)bis(1H-Pyrrole-5,2-diyl)dimethanol 6 (26):

In a dry RBF under argon, 1,9-Diformyl-5-(4-pyridyl)dipyrromethane **5** (0.103 g, 0.365 mmol) was dissolved in THF-Methanol (10:1, 20 mL) and cooled to 0 °C. $NaBH_4$ (0.29 g, 7.66 mmol) was added in roughly 50 mg portions every 2 min under a stream of argon. The reaction mixture was stirred at room temperature for 1 h and poured into a biphasic mixture of saturated aqueous ammonium chloride and DCM (1:1, 50 mL). The organic layer was washed with water twice and dried over anhydrous Na_2SO_4 and evaporated *in vacuo* to get crude **6** (100 mg) which was used directly in the next step.

2.3.2.6 4-Pyridylporphyrin 7 (26):

1 was added to the above **6** and stirred at room temperature for 5 min. TFA (0.33 mL, 4.39 mmol) was added and the mixture was stirred for 1 h. DDQ (0.247 g, 1.09 mmol) in toluene (6 mL) was added and stirred for1 h. Triethylamine (0.6 mL, 4.39 mmol) was added and stirred for 10 min. The reaction mixture was evaporated *in vacuo*. Crude **7** was isolated at 2-10% MeOH in DCM as a purple solid (150 mg) using flash chromatography and purified by preparative TLC (eluted by 5% MeOH in DCM). The purple band was collected and extracted from the silica with MeOH. Evaporation of the solvent *in vacuo* gave **7** as a purple-red solid (6 mg, 8%). ^{1}HNMR (600 MHz, DMSO-d_6): δ = 10.70 (s, 2H), 10.64 (s, 1H), 9.74-9.72 (m, J = 4.4 Hz, 6H), 9.33 (d, J = 5.9 Hz, 2H), 9.27 (d, J = 4.4 Hz, 2H), 8.92 (d, J = 5.9 Hz, 2H) and -3.57 (br s, 2H, NH) ppm.

2.3.2.7 S-2-Pyridyl isonicotinothioate 8 (31,32):

An oven dried flask was charged with 2-mercaptopyridine (1.000 g, 8.99 mmol) and purged with argon. The solid was dissolved in anhydrous THF (20 mL) with stirring.

The solution was treated with isonicotinoyl chloride hydrochloride (1.600 g, 8.99 mmol). The resulting slurry was stirred overnight. The reaction mixture was filtered. The filtrate was washed with hexanes. The resulting orange solid was added to a biphasic solution of diethyl ether and saturated sodium bicarbonate and stirred until it no longer bubbled. The organic layer was collected and the aqueous layer was washed with diethyl ether (3 x 50 mL). The organic layers were combined and dried with Na_2SO_4 and concentrated *in vacuo* to yield a yellow solid. Minimal THF was added to the solid to form a slurry which was filtered and washed with hexanes to yield **8** (0.8 g, 45%). ^{1}HNMR (300 MHz, DMSO-d_6): δ = 8.65 (m, 2H), 8.719 (m, 1H), 7.820-7.854 (m, 3H), 7.749 (d, J = 7.8 Hz, 1H), 7.40 (m, 1H).

2.3.2.8 1-Isonicotinoyl-5-(4-pyridyl) dipyrromethane 9 (31,32):

To a solution of **6** (0.844 g, 3.8 mmol) in THF (15 mL) under argon was added dropwise 1.0 M EtMgBr (9.6 mL, 9.6 mmol) at room temperature. The flask was stirred for 10 min and cooled to -78 °C. S-2-pyridyl isonicotinothioate (0.795 g, 3.7 mmol) in THF (15 mL) was added dropwise over 10 min and stirred for an additional 10 min before warming to RT and stirring for 4 h. The reaction was quenched at RT with 25 mL saturated aqueous NH_4Cl. The slurry was extracted with EtOAc (3 x 25 mL). The organic layer was washed with DI water (3 x 20 mL), brine (3 x 20mL), dried with Na_2SO_4 and evaporated *in vacuo* to yield a yellow-brown solid. Flash chromatography gave **9** (0.506, 1.54 mmol) as a light brown solid in 41% yield eluting at 12% MeOH in DCM. ^{1}HNMR (300 MHz, DMSO-d_6): δ = 12.290 (br s, 1H), 10.809 (br s, 1H), 8.738 (d, J = 4.8, 2H), 8.493 (d, J = 4.8), 7.650 (d, J = 4.8), 7.159 (d, J = 4.8, 2H), 6.774 (m, 1H), 6.693 (m, 1H), 6.067 (m, 1H), 5.942 (m, 1H), 5.761 (m, 1H), 5.601 (s, 1H).

2.3.2.9 5,10-Di(4-pyridyl)porphyrin 10 (32):

To a stirred solution of 1-formyldiprromethane **2** (0.018 g, 0.103 mmol) and 1-isonicotinoyl-5-(4-pyridyl) dipyrromethane **9** (0.035 g, 0.106 mmol) in 2.4 mL toluene in a microwave reactor vial was added DBU (0.35 ml, 2.3 mmol) and stirred for 10 min. $MgBr_2$ (0.125 g, 0.67mmol) was added to the vial, which was then capped in atmosphere and heated to 115 °C for 90 min in the microwave reactor with magnetic stirring. The vial was emptied and rinsed with THF into a pear-shaped flask and evaporated. The crude solid was dissolved in DCM (15 mL) and washed with DI water (2 x 30 mL) and brine (2 x 30mL) dried with Na_2SO_4 and evaporated. The solid was dissolved in 4 mL DCM and demetallated with trifluoroacetic acid (0.050 mL) and neutralized with triethylamine (0.040 mL). After 5 min the mixture was washed with DI water (1 x 10 mL) and brine (2 x 10 mL), dried with Na_2SO_4 and evaporated to dryness. The crude product was then purified by column chromatography eluting at 45-50% MeOH in EtOAc. Evaporation of the solvent gave **10** (0.017g) in 35% yield. ^{1}HNMR (300 MHz, $CDCl_3$): δ = 10.341 (s, 2H), 9.519 (s, 2H), 9.439 (m, 2H), 9.079 (m, 4H), 9.012 (m, 2H), 8.936 (s, 2H), 8.206 (m, 4H), -3.422 (s, 2H).

2.3.2.10 5,15-Di-(4-pyridyl)porphyrin 12 (26):

5-(4-pyridyl) dipyrromethane **4** (1.000 g, 4.51 mmol), trimethyl orthoformate **11** (36 mL, 329 mmol) and DCM (700 mL) were added to a flask covered with aluminum foil, stirred and degassed by bubbling with argon for 30 min. A solution of TCA (17.6 g, 108 mmol) in DCM (300 mL) was added drop wise to the flask over 15 min. The reaction was stirred under argon for 4 h. The mixture was quenched with pyridine (31.2 mL) and stirred for 18 h. The reaction mixture was bubbled with air for 10 min. The

aluminum foil was removed and the reaction was stirred under ambient light for 4 h. The solvent was removed *in vacuo* to yield a black solid. The solid was filtered through a silica pad, and washed with DCM and 0.5% MeOH in DCM. The fraction collected was concentrated *in vacuo* and dissolved in DCM and filtered through a Buchner funnel to eliminate some black solid. The filtrate was concentrated to 3 mL and wet loaded onto a flash chromatography column. Automated flash chromatography gave pure fractions at 1% MeOH in DCM. Fractions were collected and concentrated *in vacuo* to afford **12** as a purple solid (80 mg, 4%). ^{1}H NMR (300 MHz, $CDCl_3$): δ = 10.416 (s, 2H), 9.485 (d, J = 4.65, 4H), 9.11 (m, 4H), 9.075 (d, J = 4.67, 4H), 8.260 (m, 4H).

2.3.2.11 5, 10, 15-Tri-4-pyridylporphyrin 13 (26):

5-(4-pyridyl)dipyrromethane **4** (500 mg, 2.3 mmol), trimethyl orthoformate **11** (9 mL, 82.5 mmol), 4-pyridylcarboxaldehyde **3** (0.4 mL, 4.1 mmol) and anhydrous DCM (400 mL) were added to a flask and degassed by bubbling with argon for 30 min. In a separate flask, TCA (8.83 g, 54 mmol) was dissolved in anhydrous DCM (100 mL). The solution was added to the reaction mixture slowly over 15 min and stirred for 4 h. The reaction mixture was quenched with pyridine (15.6 mL) and stirred for 2 h. DDQ (0.3 g, 1.3 mmol) was added and stirred for 15 min. The aluminum foil was removed and the solvent was evaporated *in vacuo* to yield a black solid, which was left on high vacuum overnight. The black solid was preadsorbed onto silica and purified twice via automated flash chromatography using 5% MeOH in DCM. Preparative TLC, run in 8% MeOH in DCM gave **13** as a purple band, isolated as a purple solid (15 mg, 1.3%). ^{1}H NMR (300 MHz, $CDCl_3$) : δ = 10.355 (s, 1H), 9.436 (d, J = 4.7 Hz, 2H), 9.081 (m, 6H),

9.032 (d, J = 4.7 Hz, 2H), 8.923 (m, 4H), 8.218 (m, 6H), -3.118 (s, 2H). Exact mass: calculated: 542.21; found: 542.2071 ($M+H^+$)

2.3.2.12 General procedure for the quaternization of porphyrin pyridyl groups with iodomethane (26):

To an oven dried flask cooled under vacuum porphyrin (0.044 mmol) was added and purged with 3x with argon. 32 mL dry $CHCl_3$ followed by 8 mL dry DMF was added via syringe. 3.5 mL (excess) CH_3I was added and the solution was stirred for 12 hours at RT. The solution was concentrated under vacuum to 1/4 the original volume. To the solution was then added 60 mL Et_2O several times with subsequent decanting. The solid was then triturated with CH_3CN, decanted and dried *in vacuo* to yield product.

2.3.2.12.1 5-(N-methylpyridynium-4-yl) porphyrin P(5):

Trituration yielded 0.002 g **P(5)**. Exact mass: calculated: 402.1713; found: 402.1771.

2.3.2.12.2 5,10-Di(N-methylpyridinium-4-yl) porphyrin P(5,10):

Note that **P(5,10)** was soluble in CH3CN, so the last wash was filtered and evaporated to dryness to yield 0.001 g **P(5,10)**. Exact mass: calculated: 494.2200; found: 494.2140.

2.3.2.12.3 5,15-Di(N-methylpyridinium-4-yl)porphyrin P(5,15):

Trituration yielded 0.012 g **P(5,15)**. ^{1}HNMR (300 MHz, DMSO-d_6): δ = 10.849 (s, 2H), 9.859 (d, J = 4.7, 4H), 9.516 (d, J = 5.91, 4H), 9.245 (d, J = 4.7, 4H), 9.083 (d, J = 5.92, 4H), 4.745 (s, 6H), -3.333 (br s, 2H). Exact mass: calculated 494.2200; found: 494.2228.

2.3.2.12.4 5,10,15-tri(N-methyl pyridinium-4-yl)porphyrin P(5,10,15):

Trituration yielded 0.008 g **P(5,10,15).** ^{1}H NMR (300 MHz, $CDCl_3$): δ = 10.866 (s, 1H), 9.860 (br s, 2H), 9.518 (m, 6H), 9.210 (m, 4H), 9.183 (m, 2H), 9.030 (m, 4H), 8.970 (m, 2H), 4.981 (s, 9H), -3.660 (s, 2H). Exact mass: calculated: 195.4200; found: 195.4242.

2.4 Results

The CD spectra shown in Figure 2.1 indicate that the WT Bcl-2 27-mer P1 promoter sequence exists as a mixed parallel/anti-parallel G-quadruplex in the K^+ BPES buffer in the absence of any added porphyrin ligand. The naked Bcl-2 27-mer CD spectrum shown in the Figure 2.1, (P/DNA = 0), exhibits typical G-quadruplex characteristic peaks and troughs at 245 nm, 265 nm and a shoulder at 290 nm (8). The dashed line shown along the x-axis in Figure 2.1 is the measured ellipticity of the porphyrin in a DNA free solution. The CD spectra for the **P(5,10,15)/Bcl-2** complexes having porphyrin to DNA ratios of 1, 2, 3, or 4 show that the CD signal for the G-quadruplex is largely the same for the complexes and the naked DNA although there is some attenuation of the characteristic peaks and troughs in the complex spectra. It is obvious that binding **P(5,10,15)** to the WT Bcl-2 27-mer P1 promoter sequence G-quadruplex does not perturb the folding of the DNA in the G-quadruplex. The CD spectra shown in Figure 2.2 are for the 2:1 complexes of the Bcl-2 G-quadruplex with P(5,15), P(5,10,15) and TMPyP4 (P(5,10,15,20)). The CD spectra shown in Figure 2.2 indicate that there is no change in the G-quadruplex structure upon complex formation with these ligands.

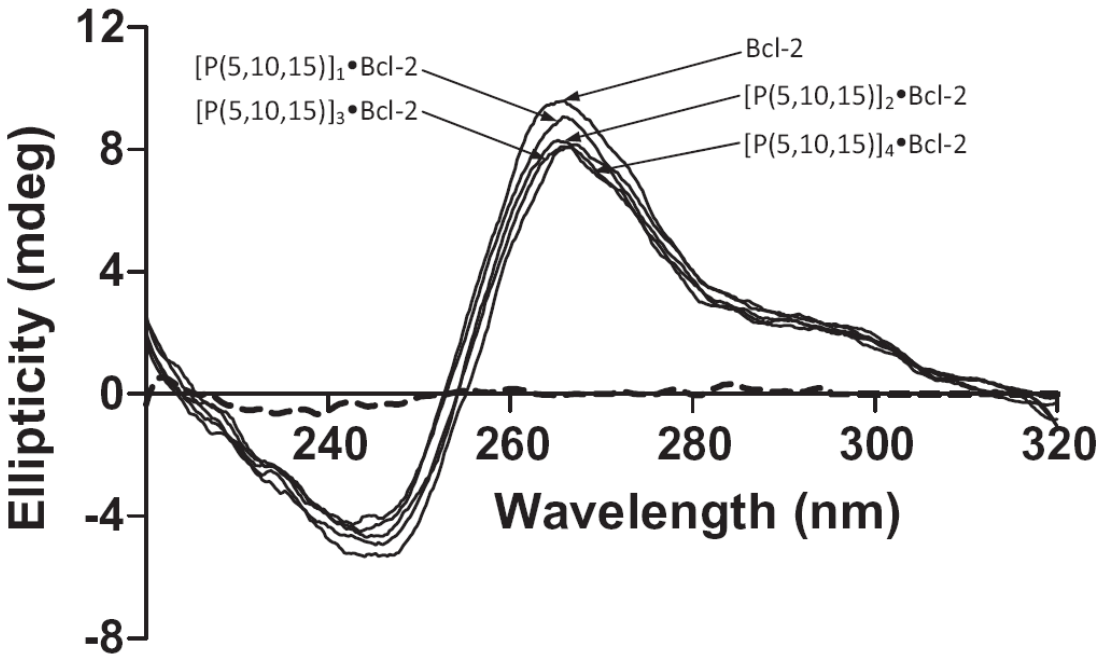

Figure 2.1 CD spectra of WT 27-mer Bcl-2 G-quadruplex in the absence and presence of the **P(5,10,15)** ligand.

The ellipticity at 265 nm is attenuated progressively as the porphyrin to DNA ration is increased from 0 to 4. The dashed line near y=0 is the ellipticity for the **P(5,10,15)** in a DNA free solution

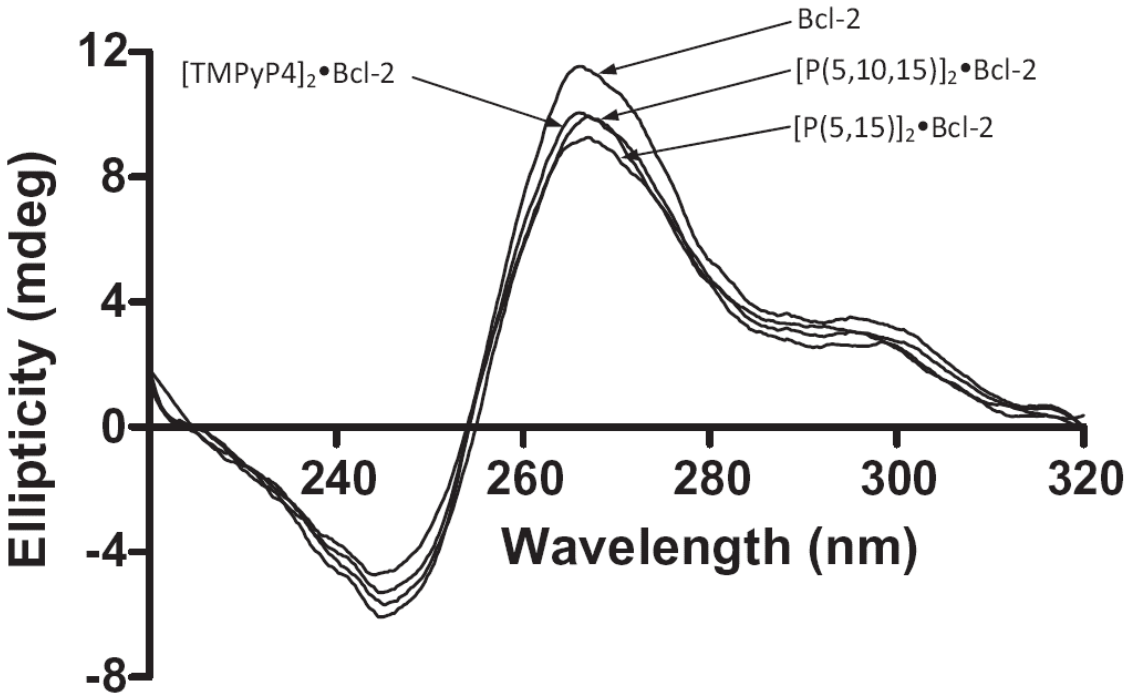

Figure 2.2 CD spectra are shown for the Bcl-2 G-quadruplex and its 2:1 complexes with **P(5,15)**, **P(5,10,15)** and **TMPyP4**.

The ellipticities at 265 nm and 295 nm are essentially the same for all three ligands and the free Bcl-2 G- quadruplex.

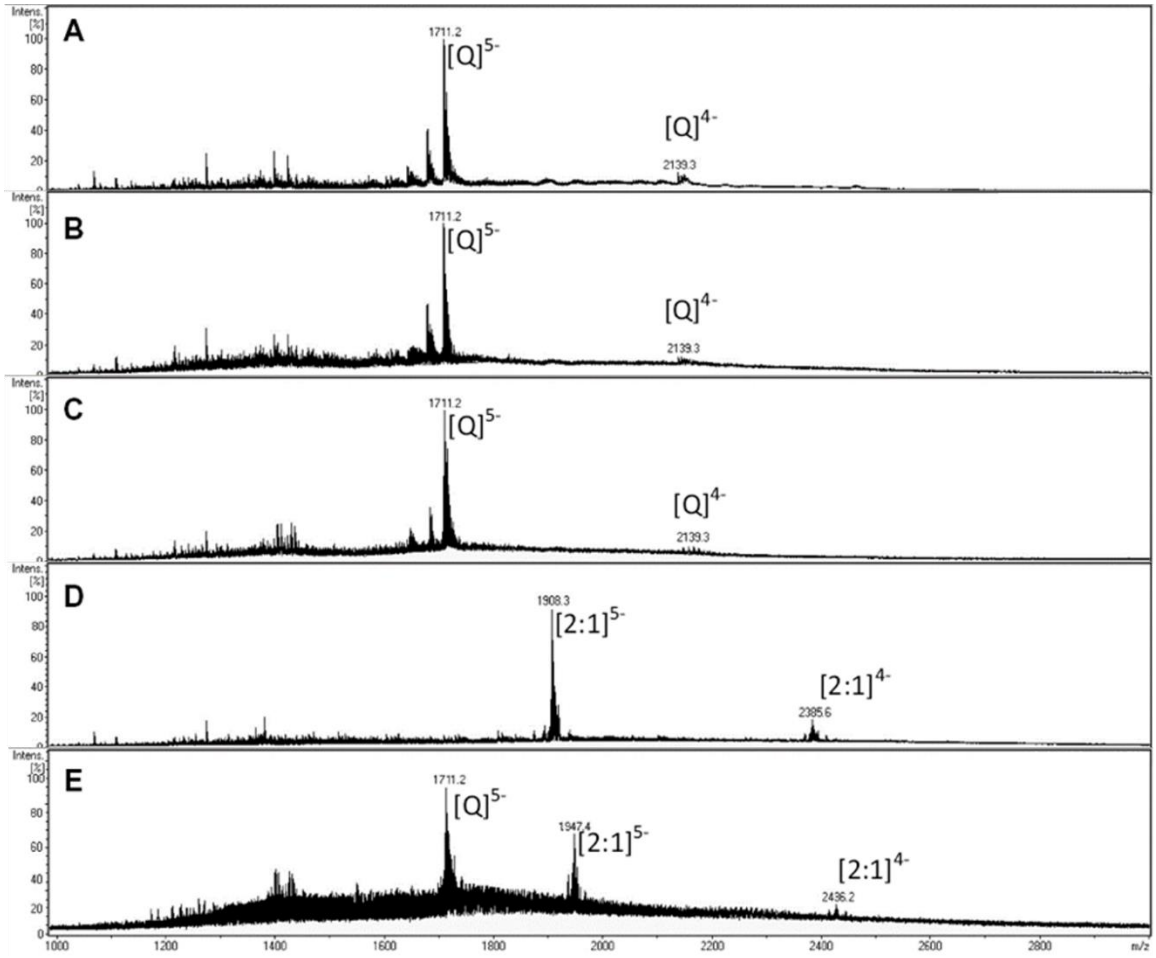

Figure 2.3 Electrospray ionization mass spectra for WT 27-mer Bcl-2 G-quadruplex and its complexes with **P(5)**, **P(5,10)**, **P(5,15)**, and **P(5,15,20)**.

Panel A shows the mass spectrum obtained for a solution containing only the Bcl-2 oligonucleotide at a concentration of 10 μM. Panels B–E show the mass spectra for the Bcl-2 oligonucleotide and its porphyrin complexes obtained in solutions containing 40 μM **P(5)**, 40 μM **P(5,10)**, 40 μM **P(5,15)** and 40 μM **P(5,15,20)**, respectively.

The ESI mass spectrum for the WT Bcl-2 27-mer P1 promoter sequence G-quadruplex, and the spectra for the saturated complexes of the WT Bcl-2 27-mer P1 promoter sequence G-quadruplex with **P(5)**, **P(5,10)**, **P(5, 15)** and **P(5,10,15)** are shown in Figure 2.3. The ESI mass spectra for the solutions containing **P(5)** or **P(5,10)** along with the Bcl-2 G-quadruplex, shown in Figure 2.3 B and C respectively, provide no

evidence for Bcl-2 complex formation with these ligands. The only peaks in the mass spectra shown in Panel B and Panel C of Figure 2.3 are for the parent DNA with a charge of -5 or -4, exactly the same as the spectrum shown in Panel A for the naked DNA. The ESI mass spectrum for the solution containing **P(5,15)** along with the Bcl-2 G-quadruplex is shown in Panel D of Figure 2.3. The spectrum for this solution which contains four moles of **P(5,15)** per mole of Bcl-2 G-quadruplex is consistent with significant complex formation. The new peaks with m/z values of 1908.3 and 2385.6 are attributed to a **P(5,15)/Bcl-2** complex having a molar ratio of 2:1 and a charge of -5 or -4 respectively. It should also be noted that no free or uncomplexed Bcl-2 is present in this solution. This result is consistent with a very large K_a for formation of the 2:1 **P(5,15)/Bcl-2** complex. The ESI mass spectrum for the solution containing **P(5,10,15)** and the Bcl-2 G-quadruplex is shown in Panel E of Figure 2.3. The spectrum for this solution, which contains four moles of **P(5,10,15)** per mole of Bcl-2 G-quadruplex, is consistent with weaker complex formation. The new peaks with m/z values of 1947.4 and 2436.2 are attributed to a **P(5,10,15)/Bcl-2** complex having a molar ratio of 2:1 and a charge of -5 or -4. In this spectrum a peak with an m/z value of 1711.2 which corresponds to uncomplexed G-quadruplex with a charge of -5 is also seen. The same peak (m/z = 1711.2) is also seen as the predominant peak in the spectrum obtained for DNA in the ligand free solutions (Figure 2.3 Panel A). The ESI-MS spectra were obtained using ammonium acetate as the buffer and supporting electrolyte (in place of either Na^+ or K^+). The greater lability of the ammonium ion in comparison to either sodium or potassium ions reduces DNA counter ion adduction yields a cleaner mass spectrum. Under these

conditions, the observation of the loss of the two NH_4^+ from between the stacked G-tetrads in the quadruplex is problematic.

Due to the limited solubility of the **P(5)**, **P(5,10)**, **P(5,15)** and **P(5,10,15)** porphyrin ligands, the ITC experiments were all done as reverse titrations in which a dilute solution of the DNA was added to a dilute solution of the porphyrin in the calorimeter cell (see Figure 2.4). Reverse titration is a common practice for systems with low solubility and yields thermograms that are easily fit to an independent site model with the CHASM© program (28) (see ITC data in Figure 2.4 panel C). Typical ITC data for the titration of the **P(5,15)** porphyrin ligand with the Bcl-2 G-quadruplex are shown in Figure 2.4 panel A. The data shown in Figure 2.4 panel B are for the dilution of **P(5,15)**, i.e. the curve shown is for the addition of buffer to the **P(5,15)** porphyrin titrate. The heats of dilution for these porphyrins were significant, a sign that the porphyrins in solution are undergoing some self-association. The data shown in Figure 2.4 panel C are the integrated heat data corrected for the heat of dilution. The best fit parameters and associated uncertainties for the non-linear regression fit of the ITC heat data are shown in the box in Figure 2.4 C. The expected value of n would be 0.5 for a complex having two ligands per mole of DNA since these data are for the reverse titration. The ITC data for the **P(5,15)** and **P(5,10,15)** titrations were similar in that these two ligands bind with similar stoichiometry (2:1) and similar affinity ($K_a \approx 1\times10^7$). The ITC data for the **P(5)** and **P(5,10)** titrations were similar in that these two ligands were not observed to bind and the titrations were almost identical to the blank titrations. The corrected data for the **P(5,15)** and **P(5,10,15)** titrations were fit with CHASM© to yield best fit values for K, ΔH, and n. Values of ΔG and $-T\Delta S$ were calculated from the best fit parameters and are

reported in Table 2.1. The relative affinities for binding the four new porphyrin ligands and TMPyP4 to the WT Bcl-2 promoter sequence G-quadruplex are: $K_{TMPyP4} \approx K_{P(5,15)} > K_{P(5,10,15)} >>> K_{P(5,10)}, K_{P(5)}$. The ITC and ESI-MS data are in agreement with respect to the relative affinities

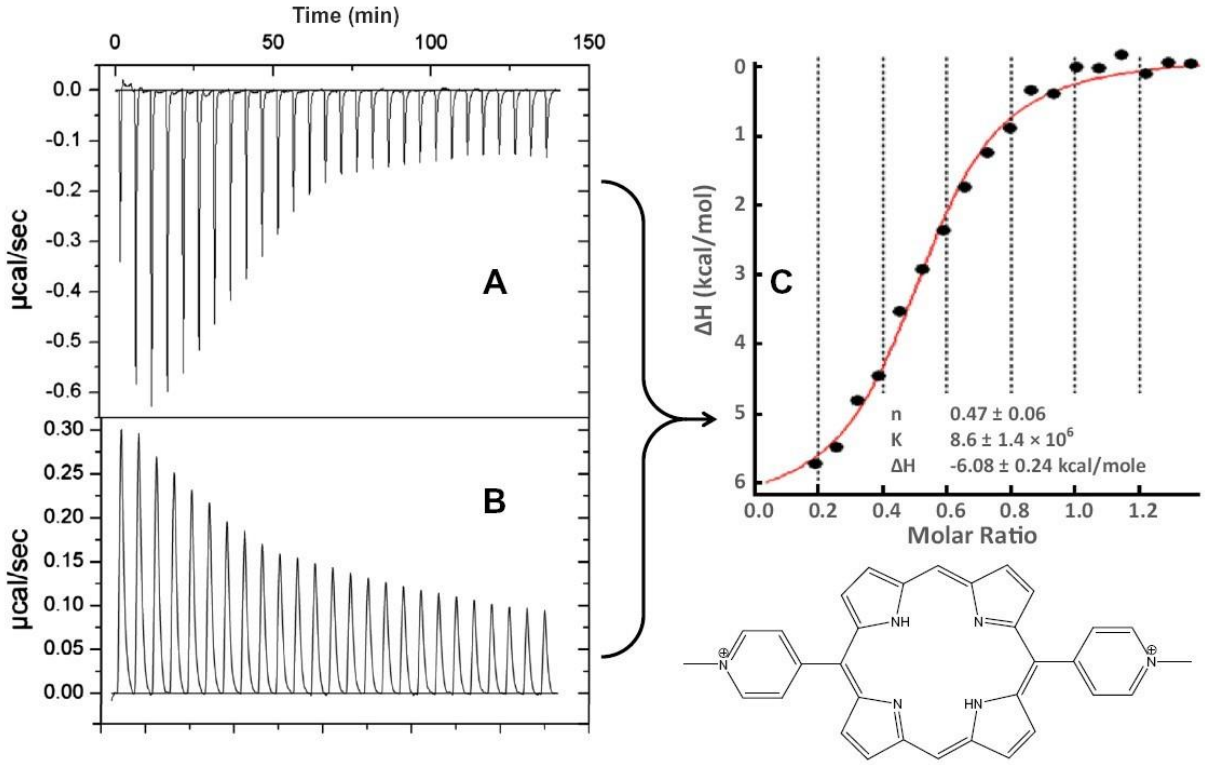

Figure 2.4 Panel A shows the thermogram for the addition of the 115 µM WT-27mer Bcl-2 titrant into 5 µM **P(5,15)**, Panel B shows the thermogram for heat of dilution of the porphyrin solution, that is, the addition of buffer into 5 µM **P(5,15)**, and Panel C shows the corrected enthalpogram for titration DNA into porphyrin ligand along with the model fit (—) and best fit parameters for formation of the 2:1 complex.

Table 2.1 A Comparison of the thermodynamic parameters for binding the porphyrin ligands **P(5)**, **P(5,10)**, **P(5,15)**, **P(5,10,15)** and **TMPyP4** to G-quadruplex DNA.

	SPR[a]	ITC[b]						
		End Stacking				Intercalation		
Ligand	*ΔG* (kcal/mol)	*ΔG* (kcal/mol)	*ΔH* (kcal/mol)	*-TΔS* (kcal/mol)		*ΔG* (kcal/mol)	*ΔH* (kcal/mol)	*-TΔS* (kcal/mol)
P(5)	n/a	No interaction				No interaction		
P(5,10)	-6.1 ± 0.1	No interaction				No interaction		
P(5,15)	-8.3 ± 0.1	-				-9.4 ± 0.1	-6.1 ± 0.2	-3.3
P(5,10,15)	-7.1 ± 0.1	-6.7 ± 0.1	-2.5 ± 0.4	-4.2		-		
TMPyP4	-8.4 ± 0.1	-10.4 ± 0.1	-1.8 ± 0.2	-8.6		-7.6 ± 0.1	-6.1 ± 0.1	-1.5

[a] The SPR data are for the interaction of the porphyrin ligands with a 26-mer human telomere G-quadruplex having the sequence: 5'-GGA TTG GGA TTG GGA TTG GGA TTG GG-3' (26)

[b] The ITC data reported here are for the interaction of the porphyrin ligands with a 27-mer *BCL*-2 G-Quadruplex having the sequence: 5'-CGG GCG CGG GAG GAA GGG GGC GGG AGC-30. The data for the binding of TMPyP4 to the same G-quadruplex are from Nagesh *et al*. (9)

2.5 Discussion

The synthetic routes for all four model porphyrin ligands are shown in Scheme 2.1 and all previous synthesis and synthetic methods are referenced. The synthesis of porphyrins **P(5)**, **P(5,15)**, and **P(5,10,15)** was accomplished utilizing the route reported by Goncalves *et al.* (26). This route provided these porphyrins in good yield. The synthesis of **P(5,10)** was accomplished by the modification of a synthetic route reported by Dogutan *et al.* (32). This new synthetic route provided for a more efficient means for the synthesis of the **P(5,10)** analogue as compared to the Goncalves *et al.* route.

The binding of the new porphyrin ligands was compared to TMPyP4 for the purpose of determining the effects of the ligand's solvent accessible surface area (SASA), charge, symmetry, and geometry on the thermodynamics of their interactions with G-

quadruplex DNA. The thermodynamic data given in Table 2.1 yield a couple of surprises. The binding of the **P(5,15)** and to a lesser degree the **P(5,10,15)** compounds seems to be tighter than expected, while the binding of the **P(5,10)** compound appears to be weaker than expected. The Lewis group and others have previously suggested that the two binding modes observed for the interaction of TMPyP4 with G-quadruplexes in general, and more specifically with c- MYC, Bcl-2, and K-ras promoter sequence G-quadruplexes, are 1) an "end binding" mode, and 2) an "intercalation mode" (7, 8, 10). The end-binding mode is generally accepted in the literature and is not controversial in that stacking of the planar porphyrin ligand, TMPyP4, on a terminal G-tetrad is consistent with simple π-π stacking and similar to guanine self-association. On the other hand, the proposed intercalation mode is neither proven nor does it resemble simple self-association or the π-π stacking of the end binding interaction. However, the Lewis group as well as others have published numerous studies that suggest that intercalation is plausible, not only from the saturation stoichiometry which varies as the number of stacked tetrads plus one (12), but also from the reduction in bound ligands from 4 to 2 as the ligand becomes non-planar (15). Modeling studies show that TMPyP4 can intercalate between the G-tetrads and that the structure of the G- quadruplex is not affected (33). All of these results are also supported by CD data that indicate no change in the G-quadruplex CD spectrum on formation of the 4:1 TMPyP4/DNA complex. There is also no induced CD signal for bound TMPyP4 until excess ligand is present, with excess ligand more weakly bound to the exterior of the G- quadruplex, possibly in the grooves (15). The thermodynamic signatures for these two modes are characteristic in that the "end binding" mode is accompanied by a small favorable ΔH and a large favorable $-T\Delta S$

term which drives the complex formation, while the "intercalation" mode is driven by a large favorable *ΔH* and a negligible change in entropy (7). Using these same arguments, the binding of the **P(5,15)** ligand is described as "intercalation" and the binding of the **P(5,10,15)** ligand as "end binding". In comparison to TMPyP4 which forms G-quadruplex complexes having a saturation stoichiometry of 4:1, the **P(5,15)** and **P(5,10,15)** only form 2:1 complexes with the *BCL*-2 promoter sequence G-quadruplex.

The affinities reported in Table 3.1 for binding **P(5,15)** and **P(5,10,15)** to the *BCL*-2 G-quadruplex are in general agreement with the affinities reported by Goncalves *et al.* (26) for binding these same ligands to a human telomere G-quadruplex. In comparison to this study's ITC results for G-quadruplex complex formation with these ligands, the SPR experiments of Goncalves *et al.* (26) yield a smaller ΔG° value for the interaction of **P(5,15)** (-8.3 kcal/mol vs. -9.4 kcal/mol by ITC), a similar ΔG value for the interaction of **P(5,10,15)** (-7.1 kcal/mol vs. -6.7 kcal/mol by ITC), and a smaller ΔG° value for the interaction of TMPyP4 (-8.4 kcal/mol vs. -9.0 kcal/mol, the average ΔG° for the mode 1 and mode 2 reactions as determined by ITC). All of these values are in good agreement particularly since the Goncalves results are for binding to a human telomere G-quadruplex instead of the Bcl-2 G-quadruplex used in this study which exists as an ensemble of at least three folded isomers. The biggest differences are that Goncalves *et al.* (26) reports a significant affinity for binding the **P(5,10)** ligand to a human telomere G-quadruplex, while complex formation between the **P(5,10)** ligand and the Bcl-2 promoter sequence G-quadruplex in either ITC or ESI-MS experiments was not observed in this work. Additionally Goncalves *et al.* (26) failed to find the expected 4:1 stoichiometry for the TMPyP4 complex with the human telomere (34). The SPR study of

Federici *et al.* reports two binding modes and a saturation stoichiometry of 4:1 for the binding of TMPyP4 to the c-MYC promoter sequence G-quadruplex (35). Their two reported affinities are: $K_1 \approx 1.3\times10^8$ (ΔG = -11.0 kcal/mol) and $K_2 \approx 7.7\times10^5$ ($\Delta G°$ = -8.0 kcal/mol). These are in excellent agreement with the previously reported values for the interaction of TMPyP4 with the c-MYC, Bcl-2, and K-ras promoter sequence G-quadruplexes (7, 8, 10).

Whether the binding of **P(5,15)** is through end-binding, intercalation, or binding in a G-quadruplex groove, its apparent high affinity points us in a new direction with respect to designing G-quadruplex interactive ligands. In comparison to TMPyP4, the **P(5,15)** ligand has a smaller SASA, and has a charge of only +2. However, **P(5,15)** binds to the Bcl-2 G-quadruplex with almost the same affinity as TMPyP4, $\Delta G°$ = -9.4 kcal/mol vs. -10.4 kcal/mol for TMPyP4 (for binding the first two moles of TMPyP4). It also appears to bind by the "intercalation mode" vs. the mode 1 interaction for TMPyP4 which has been assigned to "end binding". Perhaps even better G-quadruplex ligands could be synthesized to take advantage of the *trans* (5,15) substitution pattern on the core porphyrin, but with changes in the substituent charge or shape to produce stronger interactions with either the G-tetrad(s), loops, or grooves of the G-quadruplex (36-38). The weaker affinity of the **P(5,10,15)** ligand in comparison to TMPyP4 and its apparent end binding are more difficult to explain. For example, why does the removal of a single pyridinium substituent from TMPyP4 result in the loss of almost 3.5 kcal in the binding energy? Perhaps the explanation is that the substituent pyridinium groups in TMPyP4 are interacting with the loops, grooves and/or tail residues in the G-quadruplex and the loss of one interaction is destabilizing. The Arya group has begun to exploit dual recognition

with conjugated ligands incorporating both a planar moiety to base stack with an aminoglycoside to bind in the quadruplex groove (36, 37). A better understanding of the G-quadruplex interactions with model porphyrin ligands used in this study as well as other new ligands will most certainly lead to better G-quadruplex stabilizing drugs.

2.6 References

1. Baretton, G.B.; Diebold, J.; Christoforis, G.; Vogt, M.; Müller, C.; Dopfer, K.; Schneiderbanger, K.; Schmidt, M.; Löhrs, U. Apoptosis and immunohistochemical bcl-2 expression in colorectal adenomas and carcinomas: Aspects of carcinogenesis and prognostic significance. *Cancer* **1996 77**, 255-264.

2. Heckman, C.; Mochon, E.; Arcinas, M.; Boxer, L.M. The WT1 protein is a negative regulator of the normal bcl-2 allele in t(14;18) lymphomas. *Journal of Biological Chemistry* **1997**, 272, 19609-19614.

3. Gavathiotis, E., Heald, R.A., Stevens, M.F.G., Searle, M.S. (2003) Drug Recognition and Stabilisation of the Parallel-stranded DNA Quadruplex $d(TTAGGGT)_4$ Containing the Human Telomeric Repeat. *Journal of Molecular Biology*, **334**, 25-36.

4. Haider, S.M., Parkinson, G.N. and Neidle, S. (2003) Structure of a G-quadruplex–Ligand Complex. *Journal of Molecular Biology*, **326**, 117-125.

5. Han, H., Langley, D.R., Rangan, A. and Hurley, L.H. (2001) Selective interactions of cationic porphyrins with G-quadruplex structures. *Journal of the American Chemical Society*, **123**, 8902-8913.

6. Dixon, I.M., Lopez, F., Estève, J.P., Tejera, A.M., Blasco, M.A., Pratviel, G. and Meunier, B. (2005) Porphyrin derivatives for telomere binding and telomerase inhibition. *ChemBioChem*, **6**, 123-132.

7. Freyer, M.W., Buscaglia, R., Kaplan, K., Cashman, D., Hurley, L.H. and Lewis, E.A. (2007) Biophysical Studies of the c-MYC NHE III1 Promoter: Model Quadruplex Interactions with a Cationic Porphyrin. *Biophysical Journal*, **92**, 2007.

8. Nagesh, N., Sharma, V.K., Ganesh Kumar, A. and Lewis, E.A. (2010) Effect of Ionic Strength on Porphyrin Drug Interactions with Quadruplex DNA Formed by the Promoter Region of c-MYC and Bcl-2 Oncogenes. *Journal of Nucleic Acids*, 2009.

9. Nagesh, N., Buscaglia, R., Dettler, J.M. and Lewis, E.A. (2010) Studies on the Site and Mode of TMPyP4 Interactions with Bcl-2 Promoter Sequence G-Quadruplexes. *Biophysical Journal*, **98**, 2628-2633.

10. Dettler, J.M., Buscaglia, R., Le, V.H. and Lewis, E.A. (2011) DSC Deconvolution of the Structural Complexity of c-MYC P1 Promoter G- Quadruplexes. *Biophysical Journal*, **100**, 1517-1525.

11. Dettler, J.M. and Lewis, E.A. (2011) Biophysical Studies of the Structure, Stability and Ligand Properties of G-Quadruplex DNA: Thoughts and Comparisons of the K-ras, c-MYC, and Bcl-2 Oncogene promoter Sequence Quadruplexes. *Frontiers in Nucleic Acids*, **1082 VOL.**, 33-50.

12. Haq, I., Trent, J.O., Chowdhry, B.Z. and Jenkins, T.C. (1999) Intercalative G-tetraplex stabilization of telomeric DNA by a cationic porphyrin. *Journal of the American Chemical Society*, **121**, 1768-1779.

13. Arora, A. and Maiti, S. (2008) Effect of loop orientation on quadruplex - TMPyP4 interaction. *Journal of Physical Chemistry B*, **112**, 8151-8159.

14. Kimura, T., Kawai, K., Fujitsuka, M. and Majima, T. (2006) Detection of the G-quadruplex-TMPyP4 complex by 2-aminopurine modified human telomeric DNA. *Chemical Communications*, 401-402.

15. Le, V.H., Nagesh, N. and Lewis, E.A. (2013) Bcl-2 promoter sequence G-quadruplex interactions with three planar and non-planar cationic porphyrins: TMPyP4, TMPyP3, and TMPyP2. *PloS one*, **8**, e72462.

16. Han, H., Bennett, R.J. and Hurley, L.H. (2000) Inhibition of unwinding of G-quadruplex structures by Sgs1 helicase in the presence of N,N'-Bis[2-(1-piperidino)ethyl]-3,4,9,10-perylenetetracarboxylic diimide, a G-quadruplex-interactive ligand. *Biochemistry*, **39**, 9311-9316.

17. Neidle, S. (2010) Human telomeric G-quadruplex: The current status of telomeric G-quadruplexes as therapeutic targets in human cancer. *FEBS Journal*, **277**, 1118-1125.

18. Collie, G.W., Promontorio, R., Hampel, S.M., Micco, M., Neidle, S. and Parkinson, G.N. (2012) Structural basis for telomeric G-quadruplex targeting by naphthalene diimide ligands. *Journal of the American Chemical Society*, **134**, 2723-2731.

19. Monchaud, D., Granzhan, A., Saettel, N., Guedin, A., Mergny, J.L. and Teulade-Fichou, M.P. (2010) "One ring to bind them all"-part I: the efficiency of the macrocyclic scaffold for g-quadruplex DNA recognition. *Journal of Nucleic Acids*, **2010**. 2010, 5258-5262

20. Li, Q., Xiang, J.F., Yang, Q.F., Sun, H.X., Guan, A.J. and Tang, Y.L. (2013) G4LDB: a database for discovering and studying G-quadruplex ligands. *Nucleic Acids Research*, **41**, D1115-1123.

21. Yaku, H., Murashima, T., Tateishi-Karimata, H., Nakano, S. I., Miyoshi, D. and Sugimoto, N. (2013) Study on effects of molecular crowding on G-quadruplex-ligand binding and ligand-mediated telomerase inhibition. *Methods*, **64**, 19-27

22. Iida, K., Majima, S., Nakamura, T., Seimiya, H. and Nagasawa, K. (2013) Evaluation of the interaction between long telomeric DNA and macrocyclic hexaoxazole (6OTD) dimer of a G-quadruplex ligand. *Molecules*, **18**, 4328-4341.

23. Tan, W. and Yuan, G. (2013) Electrospray ionization mass spectrometric exploration of the high-affinity binding of three natural alkaloids with the mRNA G-quadruplex in the BCL2 5′-untranslated region. *Rapid Communications in Mass Spectrometry*, **27**, 560-564.

24. Zhu, L.N., Wu, B. and Kong, D.M. (2013) Specific recognition and stabilization of monomeric and multimeric G-quadruplexes by cationic porphyrin TMPipEOPP under molecular crowding conditions. *Nucleic Acids Research*, **41**, 4324-4335.

25. Blankson, G.A., Pilch, D.S., Liu, A.A., Liu, L.F., Rice, J.E. and Lavoie, E.J. (2013) Macrocyclic biphenyl tetraoxazoles: Synthesis, evaluation as G-quadruplex stabilizers and cytotoxic activity. *Bioorganic and Medicinal Chemistry*, **21**, 4511-4520.

26. Gonçalves, D.P.N., Ladame, S., Balasubramanian, S. and Sanders, J.K.M. (2006) Synthesis and G-quadruplex binding studies of new 4-N-methylpyridinium porphyrins. *Organic and Biomolecular Chemistry*, **4**, 3337-3342.

27. Plum, G.E. (2000) Determination of oligonucleotide molar extinction coefficients. *Current Protocols in Nucleic Acid Chemistry*, **73**, 1-17.

28. Le, V.H., Buscaglia, R., Chaires, J.B. and Lewis, E.A. (2013) Modeling complex equilibria in isothermal titration calorimetry experiments: thermodynamic parameters estimation for a three-binding-site model. *Analytical Biochemistry*, **434**, 233-241.

29. Gryko, D. and Lindsey, J.S. (2000) Rational synthesis of meso-substituted porphyrins bearing one nitrogen heterocyclic group. *Journal of Organic Chemistry*, **65**, 2249-2252.

30. Littler, B.J., Miller, M.A., Hung, C.H., Wagner, R.W., O'Shea, D.F., Boyle, P.D. and Lindsey, J.S. (1999) Refined synthesis of 5-substituted dipyrromethanes. *Journal of Organic Chemistry*, **64**, 1391-1396.

31. Lindsey, J.S., Callinan, J.B., Dharma Rao, P. and Geier, G.R. (2001) A survey of acid catalysts in dipyrromethanecarbinol condensations leading to meso-substituted porphyrins. *Journal of Porphyrins and Phthalocyanines*, **05**, 810-823.

32. Dogutan, D.K., Ptaszek, M. and Lindsey, J.S. (2008) Rational or statistical routes from 1-acyldipyrromethanes to meso-substituted porphyrins. Distinct patterns, multiple pyridyl substituents, and amphipathic architectures. *Journal of Organic Chemistry*, **73**, 6187-6201.

33. Cashman, D.J., Buscaglia, R., Freyer, M.W., Dettler, J., Hurley, L.H. and Lewis, E.A. (2008) Molecular modeling and biophysical analysis of the c-MYC NHE-III1 silencer element. *Journal of Molecular Modeling*, **14**, 93-101.

34. Martino, L., Pagano, B., Fotticchia, I., Neidle, S. and Giancola, C. (2009) Shedding light on the interaction between TMPyP4 and human telomeric quadruplexes. *Journal of Physical Chemistry B*, **113**, 14779-14786.

35. Federici, L., Arcovito, A., Scaglione, G.L., Scaloni, F., Lo Sterzo, C., Di Matteo, A., Falini, B., Giardina, B. and Brunori, M. (2010) Nucleophosmin C-terminal leukemia-associated domain interacts with G-rich quadruplex forming DNA. *Journal of Biological Chemistry*, **285**, 37138-37149.

36. Xue, L., Ranjan, N. and Arya, D.P. (2011) Synthesis and spectroscopic studies of the aminoglycoside (Neomycin)-perylene conjugate binding to human telomeric DNA. *Biochemistry*, **50**, 2838-2849.

37. Ranjan, N., Davis, E., Xue, L. and Arya, D.P. (2013) Dual recognition of the human telomeric G-quadruplex by a neomycin-anthraquinone conjugate. *Chemical Communications*, **49**, 5796-5798.

38. Neidle, S. (2012). Therapeutic Applications of Quadruplex Nucleic Acids; Academic Press, Boston, pp. 151.

CHAPTER III

CALORIMETRIC AND SPECTROSCOPIC INVESTIGATIONS OF THE BINDING OF METALLATED PORPHYRINS TO G-QUADRUPLEX DNA

Previously published in *Biochimica et Biophysica Acta - General Subjects* **2015**, 1860, 902-909 and reproduced with permission

3.1 Abstract

The human telomere contains tandem repeat of (TTAGGG) capable of forming a higher order DNA structure known as G-quadruplex. Porphyrin molecules such as TMPyP4 bind and stabilize G-quadruplex structure. Isothermal titration calorimetry (ITC), circular dichroism (CD), and mass spectrometry (ESI-MS) were used to investigate the interactions between TMPyP4 and the cobalt(III), nickel(II), copper(II), and zinc(II) complexes of TMPyP4 (e.g. Co-TMPyP4) and a model human telomere G-quadruplex (hTel22) at or near physiologic ionic strength ($[Na^+]$ or $[K^+] \approx 0.15$ M). The apo-TMPyP4, Ni-TMPyP4, and Cu-TMPyP4 all formed complexes having a saturation stoichiometry of 4:1, moles of ligand per mole of DNA. Binding of apo-TMPyP4, Ni-TMPyP4, and Cu-TMPyP4 is described by a "four-independent-sites model". The two highest-affinity sites exhibit a K_a in the range of 10^8 to 10^{10} M^{-1} with the two lower-affinity sites exhibiting a K_a in the range of 10^4 to 10^5 M^{-1}. Binding of Co-TMPyP4, and Zn-TMPyP4, is best described by a "two-independent-sites model" in which only the end-stacking binding mode is observed with a K_a in the range of 10^4 to 10^5 M^{-1}. In the

case of apo-TMPyP4, Ni-TMPyP4, and Cu-TMPyP4, the thermodynamic signatures for the two binding modes are consistent with an "end stacking" mechanism for the higher affinity binding mode and an "intercalation" mechanism for the lower affinity binding mode. In the case of Co-TMPyP4 and Zn-TMPyP4, both the lower affinity for the "end-stacking" mode and the loss of the intercalative mode for forming the 2:1 complexes with hTel22 are attributed to the preferred metal coordination geometry and the presence of axial ligands. The preferred coordination geometry around the metal center strongly influences the energetics of the interactions between the metallated-TMPyP4 and the model human telomeric G-quadruplex.

3.2 Introduction

Human telomeric DNA offers an attractive therapeutic target in cancer research (1). Telomerase, an enzyme that catalyzes telomeric extension in the 3′ overhang of eukaryotic DNA, is expressed in a majority of cancer cells (2). Telomeric extension inhibits the degradation of chromosomal DNA and thereby allows for replicative immortality, whereas normal cells incur telomeric truncation of 50–200 bp with each replicative cycle (3). Allosteric inhibition of telomerase activity would allow for truncation without extension and therefore allow induction of senescence in malignant cells (4).

The human telomere contains 5–15 kb pairs consisting of the repeat unit $(TTAGGG)_n$ (3). These guanine-rich sequences are able to undergo conformational changes to form a higher order DNA structure, consisting of a series of planar G-tetrads, which are then stacked through π–π interactions to form a G-quadruplex (5). G-quadruplexes formed in the 3′-single strand overhang of the human telomere have been

studied in cells (6, 7). Stabilization of this structure allows for the inhibition of telomerase (4). Small molecules with selectivity and high affinity for G-quadruplex DNA have been studied as potential therapeutic agents (8–13). Porphyrins are known to inhibit telomerase with low cytotoxicity (8, 9). The interactions of the planar cationic porphyrin TMPyP4 (meso-tetra (N-methyl-4-pyridyl)porphyrin tetrachloride, which exhibits selectivity and high affinity for G-quadruplex DNA, have been studied extensively as a model for drug stabilization of quadruplex DNA (8, 9, 14, 15).

The Lewis group has previously published several studies of TMPyP4 interactions with G-quadruplex DNAs (13–17). It has been demonstrated that TMPyP4 binds in an n + 1 fashion, where n is the number of stacked tetrads in the quadruplex core. For example, a G-quadruplex having three stacked G-tetrads, typically binds four moles of TMPyP4 per mole of quadruplex DNA, with two moles of the TMPyP4 ligand binding by a higher affinity mode, attributed to an end binding mechanism driven largely by a favorable entropy contribution, and two moles binding by a lower affinity, intercalative mode driven by favorable changes in enthalpy. Le *et al.* has also shown that planarity of the ligand is needed for a complete saturation of the G-quadruplex, as TMPyP4 binds with a 4:1 ratio while TMPyP3 and TMPyP2 only bind with 2:1 ratio (14). By modulating the number of pyridyl substituents on the porphyrin, it was demonstrated that charge, geometry, and symmetry also play important roles in the thermodynamics and selectivity of binding porphyrins to G-quadruplex DNA (13). In this study, the incorporation of four third row transition metals into the center of the porphyrin ring to form metallated cationic porphyrins and its effects on binding were examined: Co-TMPyP4, Ni-TMPyP4, Cu-TMPyP4, and Zn-TMPyP4. The goal was to understand how

the presence of the metal, the additional positive charge, and the geometry of the metal ion environment would affect the interactions of these metallated porphyrins with G-quadruplex DNA. Obviously the metallated porphyrins are not being developed as potential drug compounds since the presence of the transition metals would be expected to render these compounds to be either toxic or even carcinogenic. In effect, this study was performed in an attempt to probe the effects of the metal ions on the binding thermodynamics for the metallated porphyrin compounds in comparison to the parent porphyrin, TMPyP4, and on the possible structures for their complexes with G-quadruplex DNA, again in comparison to the parent porphyrin, TMPyP4.

Isothermal titration calorimetry, in combination with ESI-MS and CD spectroscopy, was used to characterize the interactions of the metal containing porphyrins with a model human telomeric DNA sequence, hTel22. Although previous reports have studied some aspects of these interactions, no one has examined these specific metallated porphyrins using G-quadruplex DNA and isothermal titration calorimetry (18–20).

3.3 Materials and methods

The 22-mer oligonucleotide, hTel22, having the sequence 5′-A GGG TTA GGG TTA GGG TTA GGG-3′, was obtained from Midland Oligos (Midland, TX). DNA stock solutions were prepared by reconstituting the lyophilized oligonucleotide into its respective phosphate buffer. The buffer concentrations consisted of 20 mM phosphate and 150 mM total Na^+ or K^+ as the supporting electrolyte (the chloride form of the salt was used), as well as 1 mM EDTA, at a pH of 7.0. Oligonucleotide was exhaustively dialyzed (1000 MW cutoff membrane) against two changes of buffer solution (1 L, 24 h each) at 4 °C. The DNA stock concentrations were verified using UV–Vis spectroscopy.

DNA was annealed by quickly heating to 98 °C, holding for 10 min and then cooling to 5 °C over a 3 h period. The molar absorption coefficient was determined using a nearest-neighbor method for single-stranded DNA (21).

Co-TMPyP4 (Co^{3+}), Ni-TMPyP4, Cu-TMPyP4, Zn-TMPyP4, and apo-TMPyP4 were purchased as the chloride salts from Frontier Scientific (Logan, UT). The purity of the commercial porphyrins was confirmed by thin layer chromatography (TLC), UV–Vis and NMR spectroscopy as provided by the company. Porphyrin samples were prepared by careful weighing and dissolving in the final dialysate buffer for respective experiments. Concentrations of the metallated porphyrin ligand solutions were determined by weight as the published extinctions coefficients were unreliable for the metallated porphyrins in the phosphate buffers used in this study.

ESI-MS experiments of hTel22 porphyrin complexes were carried out on a Bruker MicrOTOFQ mass spectrometer. Data acquisition was set to operate in negative ion mode. All experiments were performed in 50 mM ammonium acetate buffer (pH 7.0) containing 20% HPLC grade methanol. The hTel 22-mer G-quadruplex sample was dialyzed against three changes of buffer, 24 h each, at 4 °C. Stock solutions of the porphyrin were prepared in the final dialysate buffer. The ESI-MS samples were prepared by stepwise, slow addition of porphyrin into hTel22 solution. The MS capillary voltage was set to +3500 V, dry N_2 gas flow was adjusted to 0.5 L/min at 110 °C, and the G-quadruplex/porphyrin samples were directly infused into the MS by using a kD Scientific syringe pump set to a flow rate of 200 μL/h. Data processing was performed using Bruker Daltonics Data Analysis program.

CD experiments were performed with an Olis DSM-20 spectropolarimeter (Bogart, GA). All measurements were performed at 25 °C using a 1 cm quartz cuvette and covering a spectral range of 220–320 nm.

ITC experiments were performed using a VP-ITC calorimeter (GE Healthcare). A typical ITC experiment consisted of either 28 (10 μL) or 56 (5 μL) injections of a dilute porphyrin solution into a dilute hTel22 DNA solution. Blank titrations were determined by injecting porphyrin into buffer solution. These dilution heats were subtracted from the ITC data for the DNA-porphyrin titrations, yielding dilution corrected heats. Corrected ITC titrations were then fit with a nonlinear regression algorithm using CHASM, a data analysis program developed in the Lewis laboratory (22).

3.4 Results

The ESI mass spectra for solutions containing mixtures of metallated-TMPyP4 complexed to hTel22 are shown in Figure 3.1. In comparison to the ESI mass spectra for the solution containing only hTel22 (11), ESI mass spectra for mixture solutions of metallated-TMPyP4/hTel22 did not contain any m/z peaks of 1740.5 or 2321.0, which correspond to the −4 and −3 unbound hTel22 species. In all four cases, the ESI mass spectra shown in Figure 3.1 provide evidence of complex formation between hTel22 and metallated-TMPyP4. In contrast to the ESI mass spectrum for a solution containing apo-TMPyP4/hTel22 in which several m/z peaks corresponding to the highest 4:1 saturation stoichiometry could be observed, the ESI mass spectra for solutions containing metallated-TMPyP4/hTel22 only provide evidence for the formation of 2:1 complexes for the Co- and Zn-TMPyP4 ligands and only provide evidence for the formation of the 3:1 complexes of the Ni- and Cu-TMPyP4 ligands. Furthermore, the natural isotopes of the

metal (Co, Ni, Cu, and Zn) result in the ESI mass spectra being more complex than observed for apo-TMPyP4. However, the isotopic distribution patterns observed in the ESI mass spectra matched with those simulated by using the Bruker Daltonics Data Analysis program.

Circular dichroism spectropolarimetry was used to investigate the effect of titrating apo-TMPyP4 and metallated-TMPyP4 into hTel22 G-quadruplex DNA. The CD spectra for the titrations of the apo-TMPyP4 and metallated-TMPyP4 into hTel22 G-quadruplex in 150 mM Na^+ are illustrated in Figure 3.2. The CD spectra of the hTel22 G-quadruplex, in the absence of any ligand, exhibited characteristic peaks at 245 nm and 295 nm as well as a trough at 265 nm (23). Additions of apo-TMPyP4 into hTel22 resulted in significant attenuation in the CD signal at 265 nm and to a lesser extent in the CD signal at 295 nm. The titrations of metallated-TMPyP4 exhibited differential effects on the CD signals of the hTel22 G-quadruplex depending on the metal center in the metallated-TMPyP4. Titrations of Co- and Zn-TMPyP4 exhibited negligible effects on the CD signal of hTel22 up to 6 equivalence of the ligands. Addition of Ni- and Cu-TMPyP4, however, resulted in significant attenuation in the CD signals at both 265 nm and 295 nm. These signal attenuations, caused by addition of Ni- and Cu-TMPyP4, are even more pronounced than the signal attenuations observed for the additions of the apo-TMPyP4 into hTel22 at the same molar ratio of ligand/DNA. Notably, the signal attenuations were also accompanied by shifts in the wavelength at both 265 nm and 295 nm.

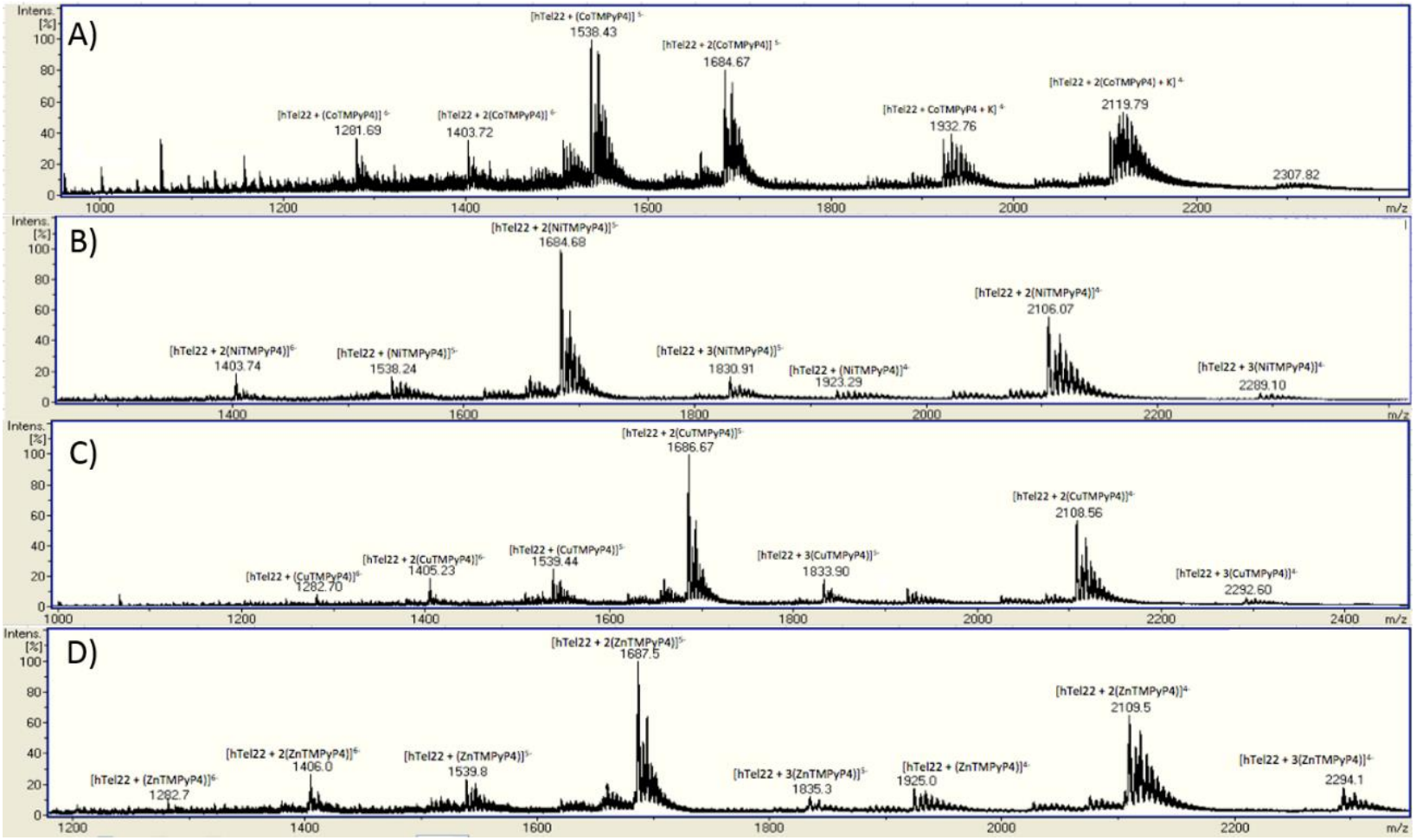

Figure 3.1 Electrospray ionization mass spectra for solutions containing hTel22 G-quadruplex DNA and excess amounts Co-TMPyP4 (panel A), Ni-TMPyP4 (panel B), Cu-TMPyP4 (panel C), and Zn-TMPyP4 (panel D).

Similar titration experiments were conducted for additions of apo- and metallated-TMPyP4 into hTel22 in potassium buffer. The CD titrations performed in 150 mM K^+ phosphate buffer are shown in Figure 3.3. In contrast to CD signals for the hTel22 observed under Na^+ conditions, the CD signals for the hTel22 observed under K^+ conditions are clearly distinctive with a characteristic shoulder at 265 nm and a peak at 295 nm (23). Additions of apo-TMPyP4, Ni-TMPyP4, and Cu-TMPyP4 into K^+ form hTel22 all resulted in significant attenuation in the CD signal at 295 nm. Similar to CD titrations performed under Na^+ conditions, the addition of Co- and Zn-TMPyP4 had minimal effect on the CD signals of K^+ form hTel22 up to 6 equivalence of the ligands. The signal attenuations near 295 nm were also accompanied by red shifts.

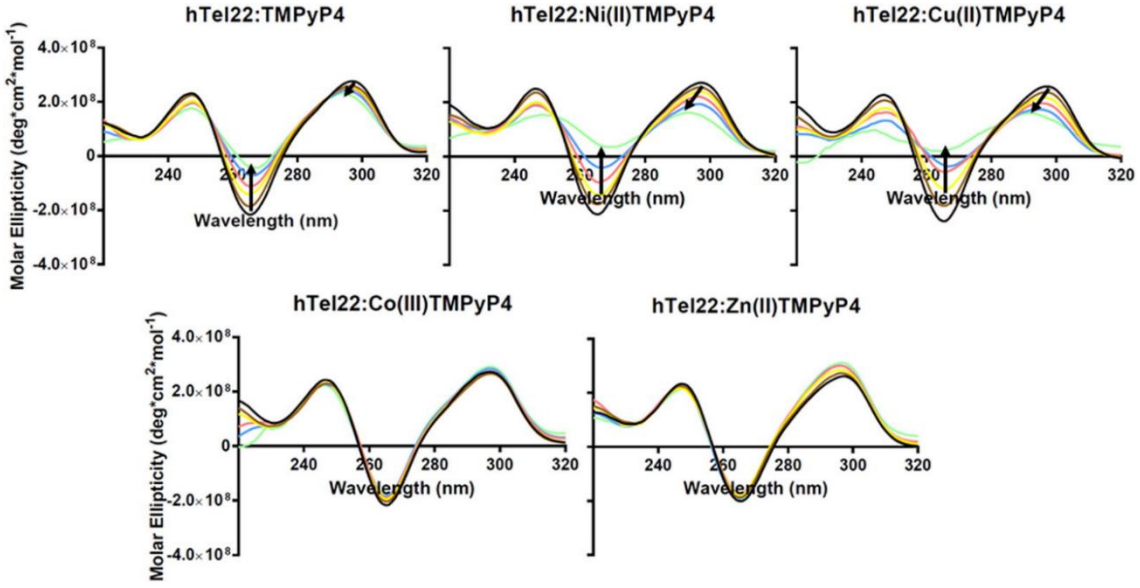

Figure 3.2 CD titration data for complexation of the hTel22 G-quadruplex with apo- and metallated-TMPyP4 in 150 mM Na^+ BPES buffer.

CD spectra of the Na^+ salt hTel22 G-quadruplex are represented as (—) while the spectra for the titrations of apo- and metallated-TMPyP4 into hTel22 are shown in colors. The CD titration data were collected at 1:1, 2:1, 3:1, 4:1, and 6:1 ratios of ligand per DNA and were corrected for the signal of ligands at the corresponding ratios. Arrows indicate the shifts at the characteristic wavelengths for Na+ hTel22.

CD spectra are difficult to interpret and the subtle changes in the 295 region are only noted here to indicate that the strongly binding compounds, TMPyP4, Ni-TMPyP4, and Cu-TMPyP4 are influencing the structure of the hTel22 G-quadruplex. The important point is that there are no significant changes in the G-quadruplex signature peaks in the CD titrations employing the more weakly interacting Co and Zn porphyrins. Explaining the small blue and red shifts observed in the 295 nm region for both the Na^+ and K^+ hTel22 G-quadruplexes when titrated with TMPyP4, Ni-TMPyP4, or Cu-TMPyP4 is beyond the scope of this manuscript.

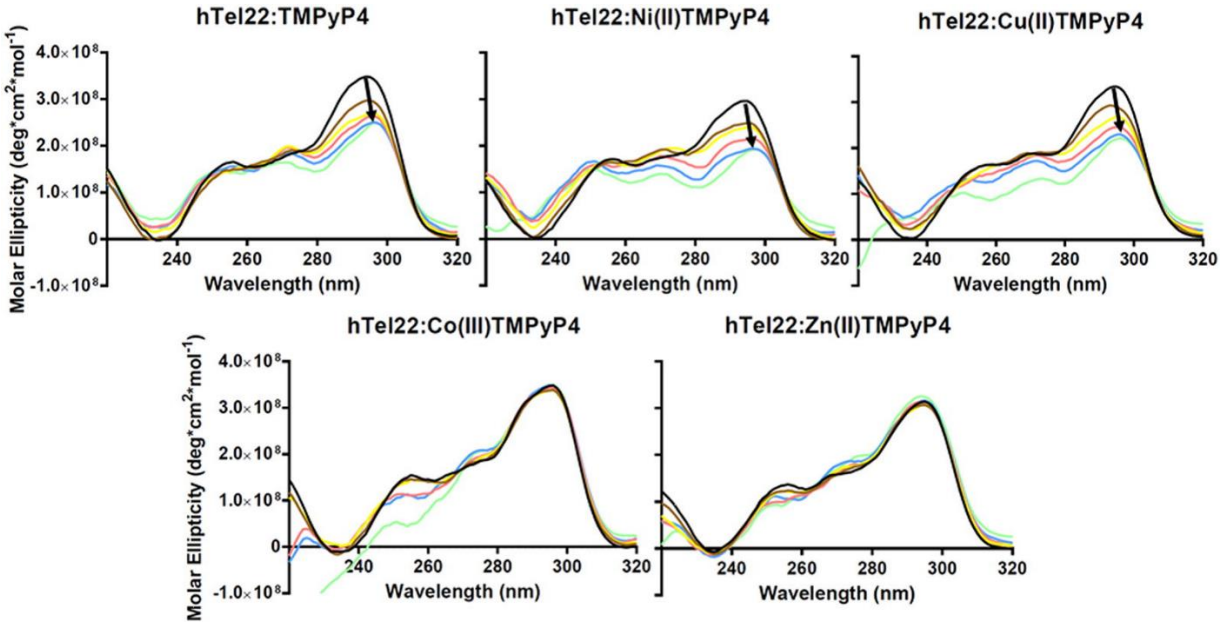

Figure 3.3 CD titration data for complexation of the hTel22 G-quadruplex with apo and metallated-TMPyP4 in 150 mM K^+ BPES buffer.

CD spectra of the Na^+ salt hTel22 G-quadruplex are represented as (—) while the spectra for the titrations of apo and metallated-TMPyP4 into hTel22 are shown in colors. The CD titration data were collected at 1:1, 2:1, 3:1, 4:1, and 6:1 ratios of ligand per DNA and were corrected for the signal of ligands at the corresponding ratios. Arrows indicate the shifts at the characteristic wavelength for K^+ hTel22

To further investigate the interactions between hTel22 G-quadruplex with both the apo-TMPyP4 and metallated-TMPyP4, a series of ITC experiments in two different buffer conditions was performed: 150 mM Na^+ and 150 mM K^+. As shown in Figures 4.4 and 4.5, the titration experiments of TMPyP4 (both apo- and metallated-) into hTel22 G-quadruplex are more complex than the TMPyP4 titrations previously reported for the addition of TMPyP4 to oncogene promoter sequence G-quadruplexes for c-MYC, BCl-2 and K-ras (14–17). Figure 3.4 shows the titration data of the apo- and metallated-TMPyP4 into hTel22 G-quadruplex in 150 mM Na^+ BPES buffer. The titrations shown in Figure 3.4 have been corrected for the heats of dilution of the ligand (apo- and metallated-TMPyP4) into buffer. The titration data for apo-TMPyP4, Ni-TMPyP4, and Cu-TMPyP4, shown in the left panel of Figure 3.4, could not be adequately analyzed using the two-binding site model provided by the ITC manufacturer; instead they were fit to a three-event model using CHASM ITC data analysis software (22). However, the titration data for Co-TMPyP4 and Zn-TMPyP4, shown on the right panel of Figure 3.4, were adequately fit to a simple single binding event either by using the commercial software (Origin) or software developed in the Lewis laboratory (CHASM).

The titration data of the apo- and metallated-TMPyP4 into hTel22 G-quadruplex in 150 mM K+ BPES buffer are shown in Figure 3.5. The titrations shown in Figure 3.5 have been corrected for the heats of dilution of the ligand (apo- or metallated-TMPyP4) into buffer. Similar to the titration experiments performed in Na+ buffer, titration data of the apo-TMPyP4, Ni-TMPyP4, and Cu-TMPyP4, shown in the left panel of Figure 3.5, were fit to a three-event model using CHASM while the titration data for Co-TMPyP4 and Zn-TMPyP4, shown on the right panel of Figure 3.5, were fit to a single binding

event, Co, or to a two binding event model, Zn. Notably, for ITC experiments performed in both potassium and sodium conditions, the titrations of apo- TMPyP4, Cu-TMPyP4, and Ni-TMPyP4 into hTel22 exhibit saturation stoichiometries occurring near a molar ratio of 4:1. On the other hand, titrations of Co-TMPyP4 and Zn-TMPyP4 into hTel 22-mer exhibit a 2:1 saturation stoichiometry.

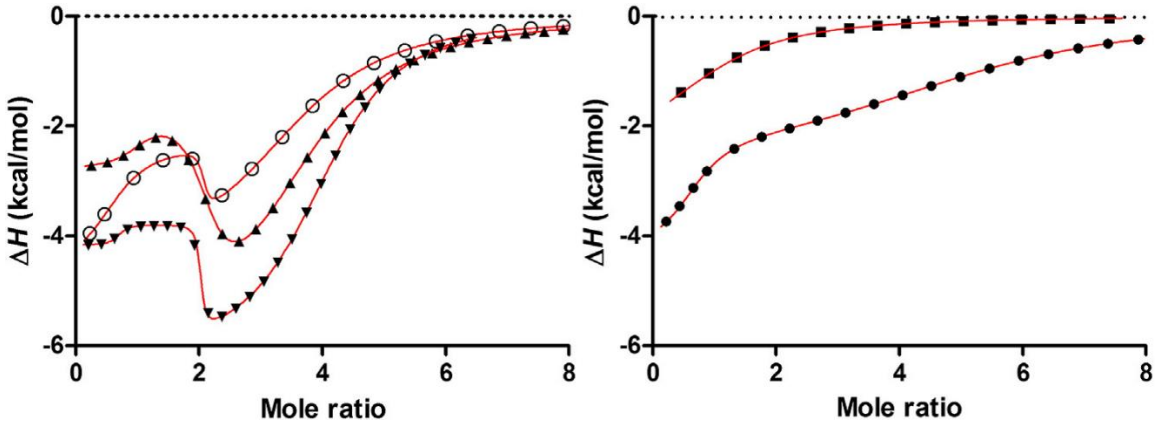

Figure 3.4 Typical nonlinear regression fits for the titration of apo (○) andmetallated-TMPyP4 into hTel22 G-quadruplex in 150 mM K+ BPES buffer.

Titration data ofmetallated-TMPyP4 are represented as following: Co-TMPyP4(■), Ni-TMPyP4 (▲), Cu-TMPyP4 (▼), and Zn-TMPyP4 (●). The titration data shown on the left panel were fit to a three-event model and the titration data shown on the right panel were fit to a single-event model. The non-linear best fits are shown in red.

Table 3.1 Thermodynamic parameters obtained from ITC experiments for the formation of the apo-TMPyP4 complexes with hTel22 in Na^+ and K^+ buffer conditions.

Cation	K_1 (M^{-1})	ΔH_1 (kcal/mol)	$-T\Delta S_1$ (kcal/mol)	K_2 (M^{-1})	ΔH_2 (kcal/mol)	$-T\Delta S_2$ (kcal/mol)	K_3 (M^{-1})	ΔH_3 (kcal/mol)	$-T\Delta S_3$ (kcal/mol)
Na^+	8.7 ± 7.8 x10^7	-8.5 ± 0.4	-2.4 ± 0.5	9.3 ± 5.4 x10^6	-2.5 ± 0.3	-7.0 ± 0.4	8.2 ± 0.7 x10^4	-4.9 ± 0.2	-1.8 ± 0.1
K^+	7.4 ± 5.2 x10^8	-4.5 ± 0.2	-7.6 ± 0.6	5.9 ± 3.5 x10^7	-2.1 ± 0.1	-7.9 ± 0.5	3.9 ± 0.2 x10^4	-5.0 ± 0.5	-1.3 ± 0.4

Table 3.2 Thermodynamic parameters obtained from ITC experiments for the formation of metallated-TMPyP4 complexes with hTel22 G-quadruplex in 150 mM Na^+ buffer conditions.

Metal center	K_1 (M^{-1})	ΔH_1 (kcal/mol)	$-T\Delta S_1$ (kcal/mol)	K_2 (M^{-1})	ΔH_2 (kcal/mol)	$-T\Delta S_2$ (kcal/mol)	K_3 (M^{-1})	ΔH_3 (kcal/mol)	$-T\Delta S_3$ (kcal/mol)
Co(III)	9.5 ± 0.7 x10^4	-2.4 ± 0.1	-3.1 ± 0.1						
Ni(II)	1.2 ± 0.9 x10^8	-6.5 ± 0.4	-4.6 ± 0.6	1.3 ± 0.9 x10^7	-0.6 ± 0.2	-9.1 ± 0.5	3.9 ± 0.2 x10^5	-5.3 ± 0.4	-2.3 ± 0.3
Cu(II)	1.7 ± 1.3 x10^8	-8.3 ± 0.3	-2.9 ± 0.4	1.1 ± 0.2 x10^7	-3.8 ± 0.1	-5.8 ± 0.4	2.6 ± 0.1 x10^5	-9.2 ± 0.3	1.8 ± 0.2
Zn(II)	3.4 ± 0.4 x10^5	-9.1 ± 0.1	2.9 ± 0.1						

3.5 Discussion

The Lewis group has recently reported on the use of ESI-MS to reveal the complex species formed and the saturation stoichiometry for ligand/DNA complexes (11, 13, 14, 24, 25). Similar to the mass spectrometry data obtained for TMPyP4 complexed with a 27-mer Bcl-2 promoter sequence G-quadruplex, ESI mass spectra indicated that the planar cationic porphyrin TMPyP4 exhibited a 4:1 saturation stoichiometry with human telomeric G-quadruplex hTel22. The absence of any m/z peaks corresponding to free DNA in the ESI mass spectrum for a solution containing apo-TMPyP4 and hTel22, is indicative of the high affinity exhibited by the TMPyP4 toward the hTel22 G-quadruplex. Similarly, there were no m/z peaks corresponding to the free DNA in the ESI mass spectra for solutions containing any of the four different metallated-TMPyP4 ligands and hTel22 G-quadruplex DNA. This suggests that all four metallated-TMPyP4 ligands bind to hTel22 with moderate to high affinity under the conditions of these experiments. However, in contrast to the ESI-MS experiments performed with the apo-TMPyP4, m/z peaks corresponding to ligand/DNA ratios greater than 3:1 for the Ni, Cu, and Zn compounds or greater than 2:1 for the Co-TMPyP4 compound, were not

observed. Furthermore, the m/z peaks observed in the mass spectrum for the apo-TMPyP4/hTel22 complex are much sharper than those observed for the metallated-TMPyP4/hTel22 complexes.

Even though Co-TMPyP4 only exhibits a maximum 2:1 stoichiometry with hTel22, while the remaining Cu-TMPyP4, Ni-TMPyP4, and Zn-TMPyP4 exhibited a maximum of 3:1 stoichiometry, these ratios are in poor agreement with the ITC endpoints that indicate saturation stoichiometries of 4:1 for the apo-TMPyP4 (confirmed by ESI-MS), and 4:1 for the Ni and Cu TMPyP4 compounds (where the ESI-MS data show maximum mole ratios of 3:1). An explanation for these differences is that the 4:1 metallated porphyrin complexes have lower solubility and precipitate in the solutions prepared for the ESI-MS experiments. The very small amounts of the 3:1 Zn-TMPyP4/hTel22 complex observed in the ESI-MS spectrum may be the result of some nonspecific ligand binding whereas the 2:1 mol ratio species observed in both the Co-TMPyP4/hTel22 and Zn-TMPyP4/hTel22 solutions are in agreement with the ITC endpoints. We have elected to use the ITC stoichiometries with some caution since they are not universally confirmed by the ESI-MS experiments.

The CD titration experiments revealed useful insights into the type of interactions that a particular ligand may impose on the structure of the DNA. The change in signal of the G-quadruplex was observed to determine how binding of a given metallated-TMPyP4 may alter the structure of the hTel22 G-quadruplex. Several conclusions can be drawn from the CD titration experiments performed under both Na^+ and K^+ conditions. First, the interactions of the apo-TMPyP4 with the hTel22 G-quadruplex proceed with only slight modification of the telomeric G-quadruplex solution structure. Secondly, the interactions

of both Co-TMPyP4 and Zn-TMPyP4 with the hTel22 G-quadruplex proceed through a mechanism that results in essentially no change in the structure of the hTel22 G-quadruplex. Thirdly, the CD titration experiments suggest that the interactions of both Ni-TMPyP4 and Cu-TMPyP4 with the hTel22 G-quadruplex are most similar to the interactions of apo-TMPyP4 with the hTel22 G-quadruplex, albeit exhibiting a greater change in the hTel22 G-quadruplex solution structure.

The Lewis laboratory's previous work has documented that the interactions between the planar cationic porphyrin, TMPyP4, and any G-quadruplex DNA, having three stacks of G-tetrads (e.g. 27-mer Bcl-2, 27-mer c-myc, and 30-mer K-ras), can typically be described by a model which includes two different binding modes, with each binding mode having two identical binding sites. The higher affinity binding mode is predominantly driven by the change in entropy while the lower affinity binding mode is driven by the change in enthalpy (14–17). The high affinity binding site has been attributed to "end-stacking" of the planar porphyrin to the top or bottom of the G-quadruplex core while the lower affinity site has been attributed to intercalation of the porphyrin between adjacent G-tetrads in the G-quadruplex core (14).

This study was initially designed to determine/understand how the preferred coordination geometry around the metal center, in a series of metallated-TMPyP4 ligands, might influence the energetics of the interactions between the metallated-TMPyP4 ligands and model 22-mer human telomeric G-quadruplex constructs. Specifically, the interactions between the metallated-TMPyP4 and hTel22 would be compared to the interactions between apo-TMPyP4 and hTel22. However, the thermograms for the titration of apo-TMPyP4 into hTel22, in either Na^+ or K^+ solutions,

are more complicated than expected. The presence of an additional event in the early part of the titrations, specifically between 0 and 1 mol ratio of TMPyP4 to DNA, indicates that the previously proposed model (4 sites and two modes) for the interactions of TMPyP4 with for example the c-MYC promoter sequence G-quadruplex is not adequate to describe the interactions between apo-TMPyP4 and hTel22. The additional reaction in the early part of the hTel22 titrations required us to use ITC analysis software developed in the Lewis laboratory to fit these titration data to a three-event model. The thermodynamic parameters for the interactions between apo-TMPyP4 and hTel22 in either Na^+ or K^+ solutions are given in Table 3.1.

Given the drastic difference in structural complexity between the K^+ form and the Na^+ form of telomeric G-quadruplex, as indicated by the CD experiments, the interactions between apo- TMPyP4 and hTel22 would be expected to be accordingly different. These differences are most apparent in the first reaction occurring in the early part of the titrations, i.e. the binding affinity exhibited by apo-TMPyP4 toward hTel22 in K^+ form is almost an order of magnitude higher than for the Na^+ form. This difference in binding affinity and the corresponding binding free energy ($\Delta\Delta G_1 = -1.3$ kcal/mol) of the first reaction is the result of the compensating effect between the enthalpy and entropy change terms. For the Na^+ hTel22 G-quadruplex, the first reaction is predominantly driven by the enthalpy change, while the first reaction for the K^+ hTel22 G-quadruplex is mainly driven by a change in entropy. Beyond the differences in the energetic profiles for the first reaction, the second and third reactions exhibit some similarities in their binding energetics: e.g. the second reaction is approximately two to three orders of magnitude greater in terms of binding affinity in comparison to the third reaction (or $\Delta\Delta G_{2-3} = \Delta G_2 -$

ΔG_3 of approximately −3 to −4 kcal/mol). Entropy changes provide the driving force for the second reaction while enthalpy changes drive the third reaction.

Even though we can only speculate what the first reaction may be in these hTel22 titrations, the second and third reactions are consistent (at least in terms of their thermodynamic profiles) with the previous model for binding TMPyP4 to G-quadruplex DNA. In other words, the second reaction is likely an "end-stacking" interaction to bind the second mole of TMPyP4 to form the $(TMPyP4)_2$(hTel22) complex species and the third reaction is attributed to the "intercalation" of two additional moles of TMPyP4 to form the $(TMPyP4)_4$(hTel22) complex species. The additional heat in the early part of the apo-TMPyP4 (or the metallated-TMPyP4) titration of hTel22 is unique to titrations of the human telomeric G-quadruplex.

There are two plausible explanations for the extra heat and apparent increased affinity for binding the first mole of TMPyP4 to hTel22. One explanation would be that the hTel22 G-quadruplex has a solution structure wherein one end of the G-quadruplex core binds TMPyP4 much more tightly than the other end of the G-quadruplex core. A second and more likely explanation is that there is a ligand induced structural reorganization of the hTel22 G-quadruplex that accompanies binding of the first mole of TMPyP4. The second explanation finds support in the fact that hTel22 G-quadruplex is known to exhibit structural complexity in the form of multiple foldamers in dynamic equilibrium. For example, Phan and Patel have published NMR studies which suggested that the two-repeat human telomeric sequence d(TAGGGTTAGGGT) can form both parallel form and anti-parallel folded structures in 100 mM K^+ and the two foldamers are in dynamic equilibrium at room temperature (26). The first reaction in the titration of

apo-TMPyP4 to hTel22 G-quadruplex can be described as the apo-TMPyP4 binding simultaneously to multiple hTel22 foldamers; this binding is coupled with some ligand-induced refolding of hTel22. It is conceivable that apo-TMPyP4 exhibits a higher affinity toward a specific hTel22 G-quadruplex topology and that this conformational selection shifts the dynamic equilibrium between the foldamers to a new equilibrium populated by the most thermodynamically favored apo-TMPyP4/hTel22 complex.

The titration data for the interactions between hTel22 and metallated-TMPyP4 have also been analyzed using the appropriate models. The thermodynamic parameters for the interactions between the metallated-TMPyP4 and hTel22, in solutions containing either Na^+ or K^+, are shown in Tables 3.2 and 3.3.

As previously noted in the Results section, the thermograms for titration of either Co-TMPyP4 or Zn-TMPyP4 to hTel22 are very different from the titration experiments of apo-TMPyP4 to hTel22. Not only do these thermograms mostly lack the initial early reaction between 0 and 1 M ratio, but these thermograms also do not exhibit the classical "check mark" pattern as previously observed for c-MYC, Bcl-2 or K-ras G-quadruplex. Instead, the titrations of either Co-TMPyP4 or Zn-TMPyP4 to hTel22 exhibit a simple sigmoidal curve. The ITC experiments provide strong evidence that the presence of a metal in the center of the metallated-TMPyP4 plays a significant role in the interactions between these porphyrins and hTel22 G-quadruplex.

Interactions between Co-TMPyP4 and hTel22 exhibit the lowest binding affinity among the series of metallated-TMPyP4 under both Na^+ and K^+ conditions. These binding affinities of Co-TMPyP4 to hTel22 are most comparable to the binding affinities determined for the third reaction in the titration of apo-TMPyP4 to hTel22. The enthalpic

and entropic contributions for binding of Co-TMPyP4 to hTel22, however, are more consistent with the second reaction in the titration of apo-TMPyP4 to hTel22. Based on the observation from the CD titration experiments in which subsequent addition of the Co-TMPyP4 resulted in almost no change in the CD signal of the hTel22 and the binding energetics obtained from ITC experiments, the binding of Co-TMPyP4 to hTel22 likely occurs via an exterior or "end-stacking" like mechanism. Except for a coordinating cobalt at the center of the porphyrin ring, Co-TMPyP4 is structurally similar to the apo-TMPyP4. The geometry and ligand environment around the cobalt center in Co-TMPyP4 must therefore account for the significant reduction in binding affinity and a complete loss of the "intercalative" mode as observed for binding of apo-TMPyP4 to hTel22.

Zn-TMPyP4 exhibits some similarity to Co-TMPyP4 in terms of its binding to hTel22, although its binding affinities toward hTel22 are slightly higher than Co-TMPyP4 under both Na^+ and K^+ conditions. The interactions of Zn-TMPyP4 to hTel22 in Na^+ conditions can be modeled via a single binding event which is predominantly driven by enthalpy change. The interactions of Zn-TMPyP4 to hTel22 in K^+ conditions, however, had to be modeled by two overlapping binding processes with the higher affinity binding driven by enthalpy change while the lower affinity binding is driven by entropy change. Although the interaction between Zn-TMPyP4 and hTel22 in K^+ conditions can be described via a two binding-process, the enthalpic and entropic contributions are not consistent with a ligand binding proceeding through "end-stacking" followed by "intercalation" mechanism. Furthermore, the CD titration experiment of Zn-TMPyP4 to hTel22 also ruled out the possibility of the "intercalation" mechanism during which some attenuation of the CD signal are often observed at characteristic wavelengths

for hTel22 G-quadruplex. A plausible explanation for two binding events, as observed for the interactions of Zn-TMPyP4 to hTel22 in K^+ salt, may be the preferential binding of Zn-TMPyP4 toward one hTel22 foldamer over the others.

Ni-TMPyP4 and Cu-TMPyP4 exhibit many similarities in comparison to apo-TMPyP4 with respect to their binding to hTel22 under both Na^+ and K^+ conditions. First, their titration experiments all contain the first reaction in the early part of the titrations (between 0 and 1 mol ratio) followed by the "checkmark" pattern. Secondly, the entropic contribution dominates the second reaction while the enthalpic contribution is the main driving force for the third reaction. These thermodynamic signatures, in combination with CD titration experiments, are in very good agreement with a process in which formation of the "end-stacking" complex is followed by the "intercalative" complex. The difference arises from comparing the thermodynamics of the first reaction in Na^+ buffer versus the K^+ buffer. The enthalpic change is the main driving force for the first reaction of binding either Ni- TMPyP4 or Cu-TMPyP4 to hTel22 G-quadruplex in Na^+ buffer. The complete opposite is observed for the first reaction of binding either Ni-TMPyP4 or Cu-TMPyP4 to hTel22 G-quadruplex in K^+ buffer in which the entropy change is the main driving force. This trend is very similar to thermodynamics of the first reaction during the binding of apo-TMPyP4 to hTel22 (see Table 3.1). With the original speculation that the first reaction is initially ligand binding coupled with a conformational reorganization of the hTel22, the difference in the thermodynamics of the first reaction, as observed in the Na^+ salt versus the K^+ salt, must arise from the difference in the hTel22 pool of foldamers in Na^+ vs. K^+ containing solutions.

The question to be asked is why Ni-TMPyP4 or Cu-TMPyP4 behave similarly to apo-TMPyP4 with respect to their interactions with hTel22 while Co-TMPyP4 or Zn-TMPyP4 behave very differently. These differences must be due to the metal ion and the coordination geometry and ligand environment around the metal center in metallated-TMPyP4, in comparison to apo-TMPyP4. Zn-TMPyP4 has been reported to have two axial ligands coordinating in an octahedral environment, (27) thereby hindering its ability to effectively form a π–π stacking with the G-tetrads, resulting a lower binding affinity toward hTel22, as well as completely inhibiting the formation of the intercalative complex. Ni-TMPyP4 is in a very fast equilibrium between the unbound (4 coordinate, square planar) and diaqua ($2 \times H_2O$, 6 coordinate, octahedral) complexes (28, 29). This very fast equilibrium can be re-established to favor the unbound square planar geometry of Ni-TMPyP4, which is capable of forming "end-stack" as well as "intercalative" complexes with hTel22 G-quadruplex. Cu-TMPyP4 has no obstacle for binding from axial ligands as its preferred coordination geometry is square planar (28). The higher affinity for Cu-TMPyP4 toward hTel22 in comparison to the apo-TMPyP4 may also come from additional orbital interactions between the metal ion and the oxygen atoms from the guanines of the G-tetrads. Lastly, Zn-TMPyP4 has strongly bound axial water in a square pyramidal environment, causing a decrease in affinity for end-stacking and inhibiting the intercalative mode (30).

This study employed isothermal titration calorimetry, in combination with ESI-MS and CD spectroscopy, to investigate the interactions between a apo-TMPyP4 and a series of metallated-TMPyP4 compounds (Co^{3+}, Ni^{2+}, Cu^{2+}, and Zn^{2+}) and the human telomeric G-quadruplex. The interactions between apo-TMPyP4 and the hTel22 alone,

measured by ITC, are more complex than originally expected. The additional complexity seems to be explained on the basis of the topological diversity presented by the hTel22 G-quadruplex. The differences in the binding of the M-TMPyP4 ligands seem to lend additional support for the two binding mode model previously proposed. The two mode model incorporating both "end-stacking" and "intercalative" binding mechanisms seems to explain the differences in the interactions of the apo-TMPyP4, Ni-TMPyP4, and Cu-TMPyP4 ligands with hTel22 G-quadruplex DNA and the interactions of the Co-TMPyP4 or Zn-TMPyP4 ligands with the hTel22 G-quadruplex construct. In addition, the higher affinity exhibited by Cu-TMPyP4 (over apo-TMPyP4) may provide a basis for the development of better G-quadruplex interactive ligands.

This study provide lessons regarding both the utility and the limitations of the ITC technique for the measurement of the thermodynamic parameters, K (or ΔG), ΔH, $-T\Delta S$, and n, for a weak (non-covalent) interaction of interest. The power of the microcalorimetry technique lies in the fact that most reactions proceed with either the evolution or the absorption of heat (i.e. the microcalorimeter is a universal detector). The limitation of the microcalorimetry technique is that other techniques must often be used in combination with the microcalorimetry technique in order to identify the origin of the measured heat effects. Another point to be made from the present study is that the results of an ITC study will almost always be model dependent in that a thermodynamic model must be used to deconvolute the observed thermograms into a set of best fit thermodynamic parameters for the model reactions.

3.6 References

1. Bears, D.J., Hurley, L.H. and Von Hoff, D.D. Telomere maintenance mechanisms as a target for drug development. *Oncogene,* **2000** 19, 6632–6641.

2. White, L.K., Wright, W.E. and Shay, J.W. (2001) Telomerase inhibitors. *Trends in Biotechnology*, **2001** 19, 114–120.

3. Doria, F., Nadai, M., Folini, M., Di Antonio, M., Germani, L. Percivalle, C., Sissi, C., Zaffaroni, N., Alcaro, S., Artese, A., Richter, S.N. and Freccero, M. F. Hybrid ligand-alkylating agents targeting telomeric G-quadruplex structures. *Organic and Biomolecular Chemistry,* **2012** 10 2798–2806.

4. Tauchi, T., Shin-ya, K., Sashida, G., Sumi, M., Okabe, S., Ohyashiki, J.H. and Ohyashiki, K. (2006) Telomerase inhibition with a novel G-quadruplex-interactive agent, telomestatin: in vitro and in vivo studies in acute leukemia. *Oncogene*, **2006** 25, 5719–5725.

5. Phan, A.T., Kuryavyi, V., Luu, K.N. and Patel, D.J. Structure of two intramolecular Gquadruplexes formed by natural human telomere sequences in K^+ solution. *Nucleic Acids Research*, **2007** 35, 6517–6525.

6. Verma, A., Yadav, V.K., Basundra, R., Kumar, A. and Chowdhury, S. Evidence of genomewide G4 DNA-mediated gene expression in human cancer cells. *Nucleic Acids Research*, **2009** 37, 4194–4204.

7. Yuan, L., Tian, T., Chen, Y., Yan, S., Xing, X., Zhang, Z., Zhai, Q., Xu, L., Wang, S., Weng, X., Yuan, B., Feng, Y. and Zhou, X. Existence of G-quadruplex structures in promoter region of oncogenes confirmed by G-quadruplex DNA cross-linking strategy. *Scientific Reports*, **2013** 3, 1811.

8. Dixon, I.M., Lopez, F., Estève, J.P., Tejera, A.M., Blasco, M.A., Pratviel, G. and Meunier, B. Porphyrin derivatives for telomere binding and telomerase inhibition. *ChemBioChem*, **2005** 6, 123–132.

9. Han, H. Langley, D.R., Rangan, A. and Hurley, L.H. Selective interactions of cationic porphyrins with G-quadruplex structures. *The Journal of the American Chemical Society*, **2001** 123, 8902–8913.

10. Gavathiotis, E., Heald, R.A., Stevens, M.F.G. and Searle, M.S. (2003) Drug recognition and stabilisation of the parallel-stranded DNA quadruplex $d(TTAGGGT)_4$ containing the human telomeric repeat. *Journal of Molecular Biology*, **2003** 334, 25–36.

11. Zhou, J., Le, V.H., Kalia, D., Nakayam, S., Mikek, C., Lewis, E.A. and Sintim, H.O. Diminazene or berenil, a classic duplex minor groove binder, binds to G-quadruplexes with low nanomolar dissociation constants and the amidine groups are also critical for G-quadruplex binding. *Molecular BioSystems*, **2014** 10, 2724–2734.

12. Haider, S.M., Parkinson, G.N. and Neidle, S. Structure of a G-quadruplex–ligand complex. *Journal of Molecular Biology*, **2003** 326, 117–125.

13. Rowland, G.B., Barnett, K., DuPont, J.I., Akurathi, G., Le, V.H., Lewis, E.A. The effect of pyridyl substituents on the thermodynamics of porphyrin binding to Gquadruplex DNA. *Bioorganic and Medicinal Chemistry*, **2013** 21, 7515–7522.

14. Le, V.H., Nagesh, N., Lewis, E.A. Bcl-2 promoter sequence G-quadruplex interactions with three planar and non-planar cationic porphyrins: TMPyP4, TMPyP3, and TMPyP2. *PLoS One*, **2013** 8, e72462.

15. Nagesh, N., Buscaglia, R., Dettler, J.M., Lewis, E.A. Studies on the site and mode of TMPyP4 interactions with Bcl-2 promoter sequence G-quadruplexes, Biophysical Journal. **2012** 98, 2628–2633.

16. Freyer, M.W., Buscaglia, R., Kaplan, K., Cashman, D., Hurley, L.H. and Lewis, E.A. (2007) Biophysical studies of the c-MYC NHE III1 promoter: model quadruplex interactions with a cationic porphyrin. *Biophysical Journal*, **2007** 92, 2007–2015.

17. Dettler, J.M. and Lewis, E.A. Biophysical studies of the structure, stability and ligand properties of G-quadruplex DNA: thoughts and comparisons of the K-ras, c-MYC, and Bcl-2 oncogene promoter sequence quadruplexes, in: R.W. Sheardy, S.A.Winkle (Eds.), **2011** *Frontiers in Nucleic Acids*, pp. 33–50.

18. Bhattacharjee, A.J., Ahluwalia, K., Taylor, S., Jin, O., Nicoludis, J.M., Buscaglia, R., Chaires J.B., Kornfilt, D.J.P., Marquardt, D.G.S., Yatsunyk L.A. Induction of G-quadruplex DNA structure by Zn 5,10,15,20-tetrakis(N-methyl-4-pyridyl)porphyrin. *Biochimie*, **2011** 93, 1297–1309.

19. Pasternack, R.F., Gibbs, E.J., Villafranca, J.J. Interactions of porphyrins with nucleic acids. *Biochemistry*, **1983** 22, 5409–5417.

20. Izbicka, E., Wheelhouse, R.T., Raymond, E., Davidson, K.K., Lawrence, R.A, Sun, D., Windle, B.E., Hurley, L.H., Von Hoff, D.D. Effects of cationic porphyrins as G-quadruplex interactive agents in human tumor cells. *Cancer Research*, **1999** 59, 639–644.

21. Plum, G.E. Determination of oligonucleotide molar extinction coefficients. *Current Protocols in Nucleic Acid Chemistry*, **2000** 73, 1–17.

22. Le, V.H., Buscaglia, R., Chaires, J.B., Lewis, E.A. Modeling complex equilibria in isothermal titration calorimetry experiments: thermodynamic parameters estimation for a three-binding-site model, *Analytical Biochemistry*, **2013** 434, 233–241.

23. Hudson, J.S., Ding, L., Le, V.H., Lewis, E.A., Graves, D. Recognition and binding of human telomeric G-quadruplex DNA by unfolding protein 1, *Biochemistry,* **2014** 53, 3347–3356.

24. Lewis, E.A., Munde, M., Wang, S., Rettig, M., Le, V.H., Machha, V., Wilson, W.D. Complexity in the binding of minor groove agents: netropsin has two thermodynamically different DNA binding modes at a single site. *Nucleic Acids Research*, **2011** 39, 9649–9658.

25. Le, V.H., McGuire, M.R., Ahuja, P., MacDonnell, F.M., Lewis, E.A. Thermodynamic investigations of $((phen)_2Ru(tatpp)Ru(phen)_2)^{4+}$ interactions with B-DNA. *The Journal of Physical Chemistry B*, **2015** 119, 65–71.

26. Phan, A.T., Patel, D.J. Two-repeat human telomeric d(TAGGGTTAGGGT) sequence forms interconverting parallel and antiparallel G-quadruplexes in solution: distinct topologies, thermodynamic properties, and folding/unfolding kinetics. *The Journal of the American Chemical Society*, **2003** 125, 15021–15027.

27. Lin, M., Marzilli, L.G. Solution chemistry of cobalt(III) porphyrins in water and nonaqueous solvents. Axial ligation by solvent and counterion. *Inorganic Chemistry*, **1994** 33, 5309–5315.

28. Pasternack, R.F., Francesconi, L., Raff, D., Spiro, E. Aggregation of nickel(II), copper(II), and zinc(II) derivatives of water-soluble porphyrins. *Inorganic Chemistry*, **1973** 12, 2606–2611.

29. Pasternack, R.F., Sutin, N., Turner, D.H. Some very rapid reactions of porphyrins in aqueous solution. *The Journal of the American Chemical Society*, **1976** 98, 1908–1913.

30. Manono, J., Marzilli, P.A., Marzilli, L.G. New porphyrins bearing positively charged peripheral groups linked by a sulfonamide group to meso-tetraphenylporphyrin: interactions with calf thymus DNA. *Inorganic Chemistry*, **2009** 48, 5636–5647.

CHAPTER IV

THE THERMODYNAMIC EFFECTS OF LIGAND STRUCTURE ON THE MOLECULAR RECOGNITION OF RUTHENIUM COMPLEXES WITH B-DNA

4.1 Abstract

Ruthenium(II) complexes have garnered increasing interest over the last 20 years including investigations into their properties as chemosensors and chemotherapeutic agents. Some polyheterocyclic ruthenium compounds have shown less toxicity and are able to overcome the resistance seen with platinum drugs. Due to the hypoxic environment present in a broad range of tumors versus normoxic cells, $[Ru(phen)_2(tatpp)]^{2+}$ (**MP**) is able to abstract a hydrogen atom from a DNA backbone deoxyribose, resulting in DNA cleavage. The binding mode of mononuclear $[Ru(phen)_3]^{2+}$ (**Rp3**) has been thoroughly examined and is reported to bind via minor groove association while $[Ru(phen)_2(dppz)]^{2+}$ (**Rp2d**) is able to intercalate. Le *et al.* recently reported on the binding of binuclear $[(phen)_2Ru(tatpp)Ru(phen)_2]^{4+}$ ($\mathbf{P^{4+}}$) which had a greater binding affinity for duplex DNA than **Rp3** and bound through an intercalative mode. To further understand the role of the intercalative ligand substituent, Ru^{2+} compounds were examined, starting at **Rp3** and building to $\mathbf{P^{4+}}$, and the primary binding events for all ligands were entropically driven with either low or unfavorable enthalpic contributions. The binding affinities to duplex DNA followed as **Rp3** < $\mathbf{P^{4+}}$ <

Rp2d < MP. A second binding mode, two orders of magnitude weaker than the first, was seen for **Rp2d.**

4.2 Introduction

Ruthenium anticancer drugs have attracted an increasing interest in the last 20 years including examination in clinical trials and compared to platinum drugs, the complexes based on ruthenium are often identified as less toxic and capable of overcoming the resistance induced by platinum drugs in cancer cells (1-4). Ruthenium complexes have shown selective activation to more reactive species by the reducing environment of solid tumors as compared to healthy tissues (5-7). Numerous studies have noted the important aspects of the photophysical properties of these ruthenium complexes (8-12).

Ruthenium(II) containing drug $[Ru(phen)_2(tatpp)]^{2+}$ (**MP**) showed promising results in a 60 day tumor regression trial that examined the growth of solid tumors in H358 bearing mice treated with the Δ enantiomer of **MP**. Results of this study included a greater than doubled subject survival time and a marked decrease of 83% less tumor growth compared to the untreated control (7). Additional studies measuring the acute toxicity of **MP** in animals showed that low toxicity existed at the doses needed in therapeutic treatment.

Reports furthering the understanding of the mode of action of these drugs have indicated that its primary function arises through H-atom extraction in a deoxyribose by a carbon radical on the tatpp ligand, causing DNA cleavage (7, 13). Dioxygen, present in only low levels in hypoxic tumor cells compared to normoxic cells, is able to quench the

radical, leading to selective cleavage of DNA in malignant cells versus healthy, normally functioning cells, as seen with the non-reactivity in healthy tissues (7, 13).

Prior publications by the Lewis group and others have examined the thermodynamic parameters involved in the binding of ruthenium(II) containing structures (14). Reports by Chaires' group examined the binding relationship of mononuclear ruthenium(II) complexes and proposed that $[Ru(phen)_3]^{2+}$ (**Rp3**) bound through a non-intercalative mechanism, but that by building upon one of the phenanthroline groups, forming $[Ru(phen)_2(dppz)]^{2+}$ (**Rp2d**), intercalation was possible and favored. Le *et al.* previously reported that $[(phen)_2Ru(tatpp)Ru(phen)_2]^{4+}$ ($\mathbf{P^{4+}}$) bound to DNA through an intercalative binding mode that took advantage of the dynamic "breathing" exhibited by duplex DNA. This present work set out to examine how increasing the size of the modified phenanthroline would affect the binding of these ruthenium(II) containing complexes using ITC to extract the entirety of the binding thermodynamics and to supplement those with CD experiments to validate the changes in structure. To our knowledge, no other groups have published studies examining the structure function relationship of these increasingly substituted heterocycle-containing $[Ru(L)(phen)_2]^{2+}$ analogs.

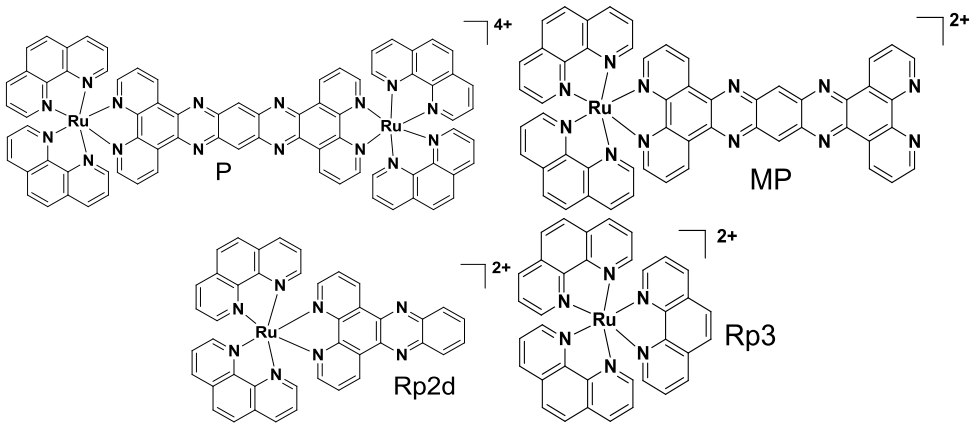

Figure 4.1 Structures of the Ru^{2+} compounds used in this study.

P=$[(phen)_2Ru(tatpp)Ru(phen)_2]^{4+}$, **MP**=$[Ru(phen)_2(tatpp)]^{2+}$, **Rp2d**=$[Ru(phen)_2(dppz)]^{2+}$, **Rp3**=$[Ru(phen)_3]^{2+}$

4.3 Material and methods

The target DNA was 25 base pair dsDNA (25bp duplex) (5′-ATC AAG CTA CGG TCT GTG AGC AAG T-3′/5′-ACT TGC TCA CAG ACC GTA GCT TGA T-3′) purchased from Midland Certified Reagent Co. as the RP grade and used without further purification. The 25bp duplex was exhaustively dialyzed against 80 mM Na^+ BPES buffer (50 mM NaCl; 10 mM Na_2HPO_4; 10 mM NaH_2PO_4; 1 mM EDTA) at pH = 7.0 and annealed by heating to 95 ^oC and holding for 10 minutes followed by cooling to 5 °C at a rate of 0.5 °C/min.

Ligands were dissolved in the final dialysate buffer and their concentrations calculated from mass of ligand used **MP** = 1018.9 g/mol; $[Ru(phen)_2dppz]^{2+}$ (**Rp2d**) = 814.69 g/mol; $[Ru(phen)_3]^{2+}$ (**Rp3**) = 712.59 g/mol). Working solutions were made fresh prior to experiments by dissolution of the weighed solid into the final dialysate and kept at RT in a drawer away from ambient light. $[Ru(phen)_2dppz]^{2+}$ required substantial heat

and sonication to dissolve completely into the buffer systems. MP required initial heat and sonication to dissolve. $[Ru(phen)_3]^{2+}$ readily dissolved in the chosen buffers.

ITC experiments were performed using a Microcal VP-ITC (Malvern) at 25 ºC. A typical experiment involved injection of 28 aliquots of dilute ligand (nominally 120 to 850 μM) into the calorimeter cell containing 1.45 ml of 10 μM DNA. Injection volumes were 10 μl and injections were made at 200 second intervals. The ITC thermograms were corrected for titrate and titrant dilution effects by performing the appropriate blank experiments and correcting the observed heats by subtracting the heats of dilution. Corrected ITC titrations were fit with a nonlinear regression algorithm using CHASM, an ITC data analysis program developed in the Lewis laboratory (15).

CD experiments were performed using an Olis DSM-20 spectropolarimeter (Bogart, GA). Typical experiments involved the titration of ligand into a DNA sample with a nominal $A_{260} = \sim 1$. Corrections were made by subtracting the signal of ligand titrated into buffer from its respective sample and converting to molar ellipticity.

ESI-MS experiments on 7 base pair hairpin (7bpHP) and the (Ligand·7bpHP) complex were carried out on a Bruker MicrOTOFQ mass spectrometer. Data acquisition was set to operate in negative ion mode. All experiments were performed in 50 mM ammonium acetate buffer (pH = 7.0) containing 20% HPLC grade methanol. The 7bpHP sample was prepared at a concentration of approximately 40 μM in the ammonium acetate buffer and was exhaustively dialyzed at 4 °C. Stock solutions of the ligands were prepared in the same final dialysate buffer. The ESI-MS samples were prepared by mixing the hairpin DNA and ligand stock solutions to yield a mixture containing 4 equivalents of ligand molecules per molecule of hairpin DNA. The MS capillary voltage

was set to +4000 V, dry N_2 gas flow was adjusted to 4 L/min at 190 °C, and the sample was directly infused into the MS by using a kD Scientific syringe pump set to a flow rate of 180 μL/h. Data processing was performed by using the Bruker Daltonics Data Analysis program.

Molecular modeling was performed by Clinton G. Mikek who used Discovery Studio 3.1. DNA-ligand molecules were drawn using the internal build functions, calculated with the CHARMm force field, and minimized with an implicit solvent model dielectric constant of 80.

4.4 Results

Le *et al.* previously reported on $\mathbf{P^{4+}}$ binding to B-DNA with an average affinity of $\sim 4 \times 10^5\ M^{-1}$ through an entropically driven intercalative mechanism (14). This work seeks to present data on structural derivatives of this parent compound. **MP**, **Rp2d**, and **Rp3** are structurally similar to the original $\mathbf{P^{4+}}$ with the exception of truncation of the structure to form a shorter tatpp, dppz, or phen protrusion from the $[Ru(Phen)_2]^{2+}$ base and exclusion of the second Ru^{2+} in the case of **MP**.

Table 4.1 summarizes the ITC data collected from the titration of concentrated ligand into a dilute sample of DNA in Na^+ BPES buffer, while Table B.1 repeats this in Tris buffer. ITC derived data for the binding of **MP** to DNA show an n value which is equal to the 12-13 sites available by observation of the nearest neighbor exclusion for 25 bp duplex. This was a racemic mixture of **MP** containing Δ and Λ molecules. Experiments with the enantiomerically pure **MP** would be worthwhile to ensure conformity across the enantiomers. **MP** binding is characterized in this study by a small enthalpic penalty against a larger entropic driving force resulting in a value for ΔG of -9.1

kcal/mol. The profile for **MP** binding to 25 bp duplex DNA is similar to that for binding of $\mathbf{P}^{4+}$ in which the previously reported formation of $\mathbf{P}^{4+}$·DNA complexes were entropically driven ($-T\Delta S = -9.7$ kcal/mol) with an unfavorable enthalpy change (ΔH = 2.0 kcal/mol) resulting in a value for ΔG of -7.1 kcal/mol.

Rp2d binding is an entropically driven intercalative process which was previously demonstrated (16). The K_a values of 1.4 x 10^6 M^{-1} and 8 x 10^4 M^{-1} for this racemic mixture in the studied buffers are in agreement with data previously collected on the enantiomers, which was K_a = 3.2 x 10^6 M^{-1} and 1.7 x 10^6 M^{-1} for Δ and Λ isomers respectively (16). The total stoichiometry is in line with the ~13 molecules that would be expected to bind through intercalation limited by neighbor exclusion (17-20).

Rp3 enantiomers were previously found to weakly bind DNA with binding affinities of 4.9 x 10^4 M^{-1} and 2.8 x 10^4 M^{-1} for the Δ and Λ isomers respectively (21). This racemic mixture was found to bind to DNA with a binding constant of approximately 1.3 x 10^4 M^{-1}. Binding was previously reported to be electrostatic in nature and not to proceed via a classical intercalative method (21). The enthalpy was previously found to be small in magnitude and positive in sign yielding an overall entropically driven binding process (22). Since hydrogen bond acceptors and donors are not included in the structure, observed enthalpy changes appear to result from van der Waals contacts, electrostatic interactions, and/or effects related to the solvation of DNA (22). These observations are consistent with the data reported in this work. Binding of an **Rp3** molecule was reported to remove 3-4 base pairs as potential binding sites from the DNA lattice which is also in agreement with the approximately five molecules that were found bound to 25bp duplex DNA in this study (21).

Table 4.1 Thermodynamic data obtained from ITC experiments performed at 298 K for the interaction between ligands and dsDNA in Na^+ BPES buffer

Ligand	K_{a1} ($x10^{-5}$ M^{-1})	ΔG_1 (kcal/mol)	ΔH_1 (kcal/mol)	$-T\Delta S_1$ (kcal/mol)	K_{a2} ($x10^{4}$ M^{-1})	ΔG_2 (kcal/mol)	ΔH_2 (kcal/mol)	$-T\Delta S_2$ (kcal/mol)
MP	47 ± 0.5	-9.1 ± 0.1	4.9 ± 0.1	-14.0 ± 0.1				
$Ru(phen)_2dppz$	14 ± 0.5	-8.4 ± 0.3	-1.1 ± 0.1	-7.3 ± 0.2	8 ± 2	-6.7 ± 0.1	-5.0 ± 2.0	-2.0 ± 2.0
$Ru(phen)_3$	0.13 ± 0.1	-5.6 ± 0.1	3.9 ± 0.1	-9.5 ± 0.1				
P^{4+} [14]	1.7 ± 0.8	-7.1 ± 0.3	2.6 ± 0.4	-9.7 ± 0.7				

Figure 4.2 shows CD results for the binding of ligand to the target 25 bp duplex DNA in Tris buffer. The signal for the titrations of **MP** into DNA demonstrates an attenuation in molar ellipticity at 274 nm and undergoes a bathochromic shift up to 2:1 binding. This bathochromic shift was previously seen in experiments with $\mathbf{P}^{4+}$ binding to a 7 base pair hairpin. Additional ligand shifts the peak to its original wavelength and by 8:1 the molar ellipticity retains only a fraction of its original intensity. The **MP** ligand is interacting with the DNA in such a way as to disrupt its structure. This disruption is likely in the form of unwinding as the intercalating moiety inserts itself between base stacked bases. Figure 4.3A shows **MP** bound to the minor grove of DNA and the displacement of the nucleotide bases to accommodate the intercalation taking place. Elongation of the duplex has occurred to accommodate the intercalation in these simulations.

Rp2d titrations demonstrate a hypsochromic shift from 275 to 260 nm for the CD signal. This 260 nm region is characteristic of A-DNA character, in which the minor groove has been elongated (23). This suggests the major groove is changing as a result of binding. This binding mode is illustrated in Figure 4.3B, modelled with ligand binding

directionally from the minor groove of DNA and one ligand molecule lying in the major groove.

Rp3 titration experiments do not demonstrate attenuation. This is consistent with a non-intercalative mode of binding. Chaires previously demonstrated that **Rp3** binds to the major/minor groove of DNA (21, 22). This binding mode is shown in Figure 4.3C. **Figure B.1** repeats the CD experiments in BPES buffer and appears very similar to the experiments in tris buffer.

As shown in Figure 4.4, the ESI mass spectra observed in the presence of the various ligands differs from that of the original DNA (shown in Figure 4.4A or 4.4C). Figure 4.4D shows notable m/z peaks at 1598.2, 1833.9, 2131.3, and 2446.3 which correspond to DNA***MP** complexes of 1 or 2 molecules of **MP** per molecule of 7 bpHP. Figure 4.4E shows notable m/z peaks at 1386.2, 1547.2, 1732.7, 1939.2, 2063.3, and 2310.3 which correspond to DNA***Rp2d** complexes of 1, 2, or 3 molecules of **Rp2d** per molecule of 7 bpHP. Notable m/z peaks in Figure 5.4F are 1521.7, 1681.7, 1841.7, 2029.2, 2242.6, and 2455.6 which correspond to DNA***Rp3** complexes of 1, 2 or 3 molecules of **Rp3** per molecule of 7 bpHP.

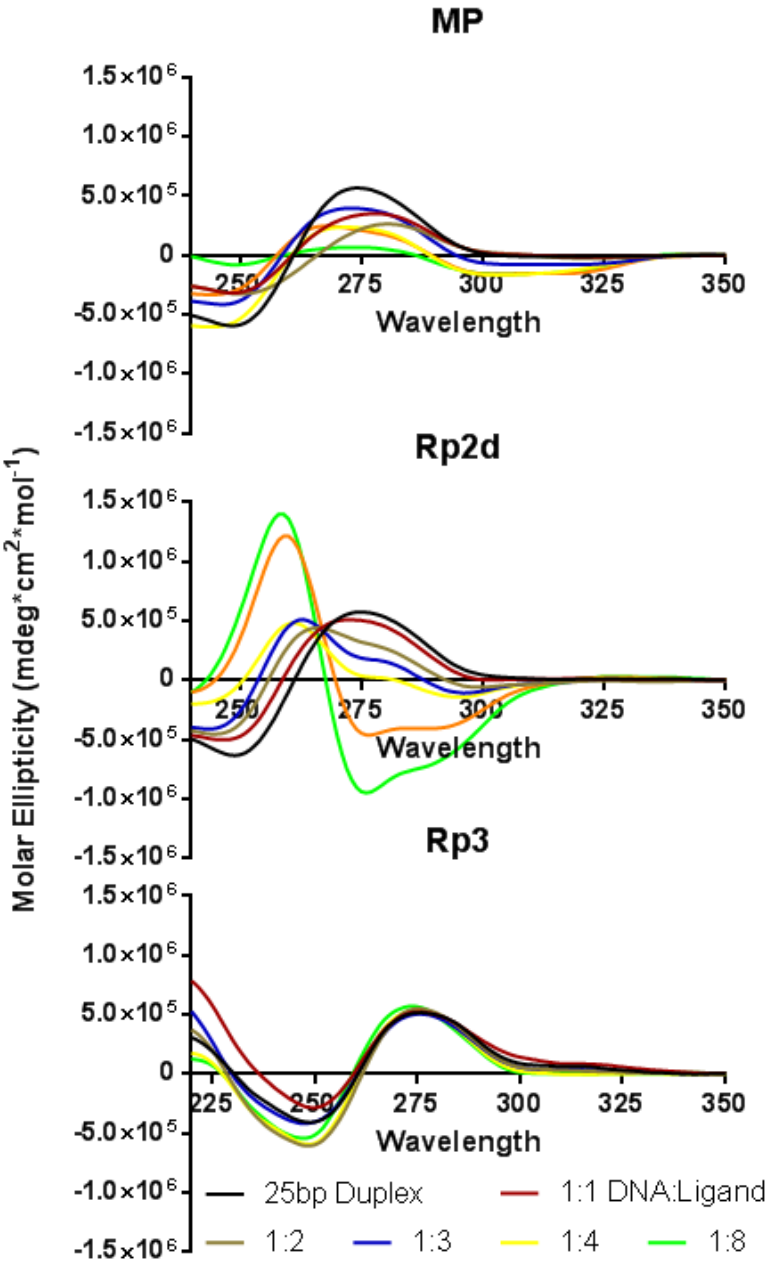

Figure 4.2 CD spectra for the subsequent titrations of Ru^{2+} complexes into DNA in tris buffer.

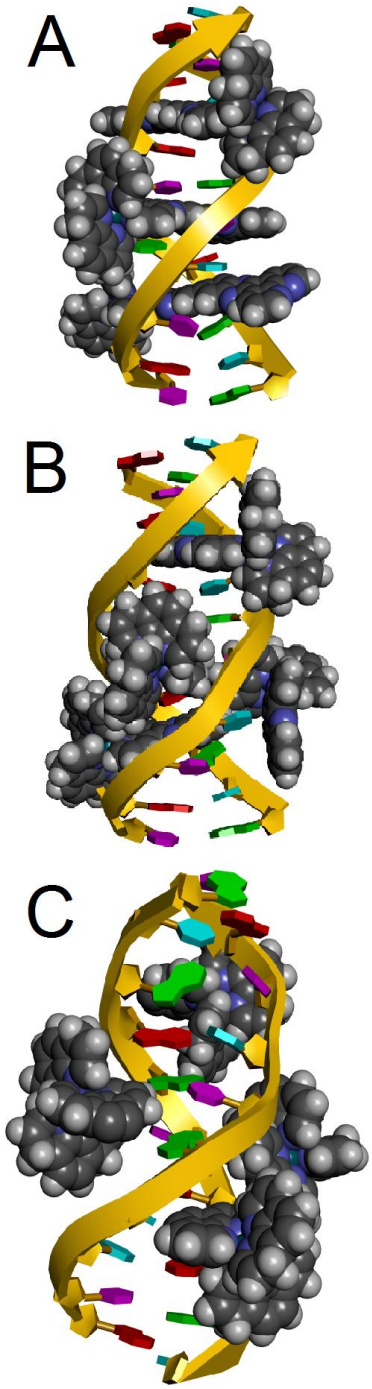

Figure 4.3 Minimized models of MP (A), Rp2d (B), and Rp3 (C) interacting with duplex DNA; calculated by Clinton G. Mikek of the Lewis lab.

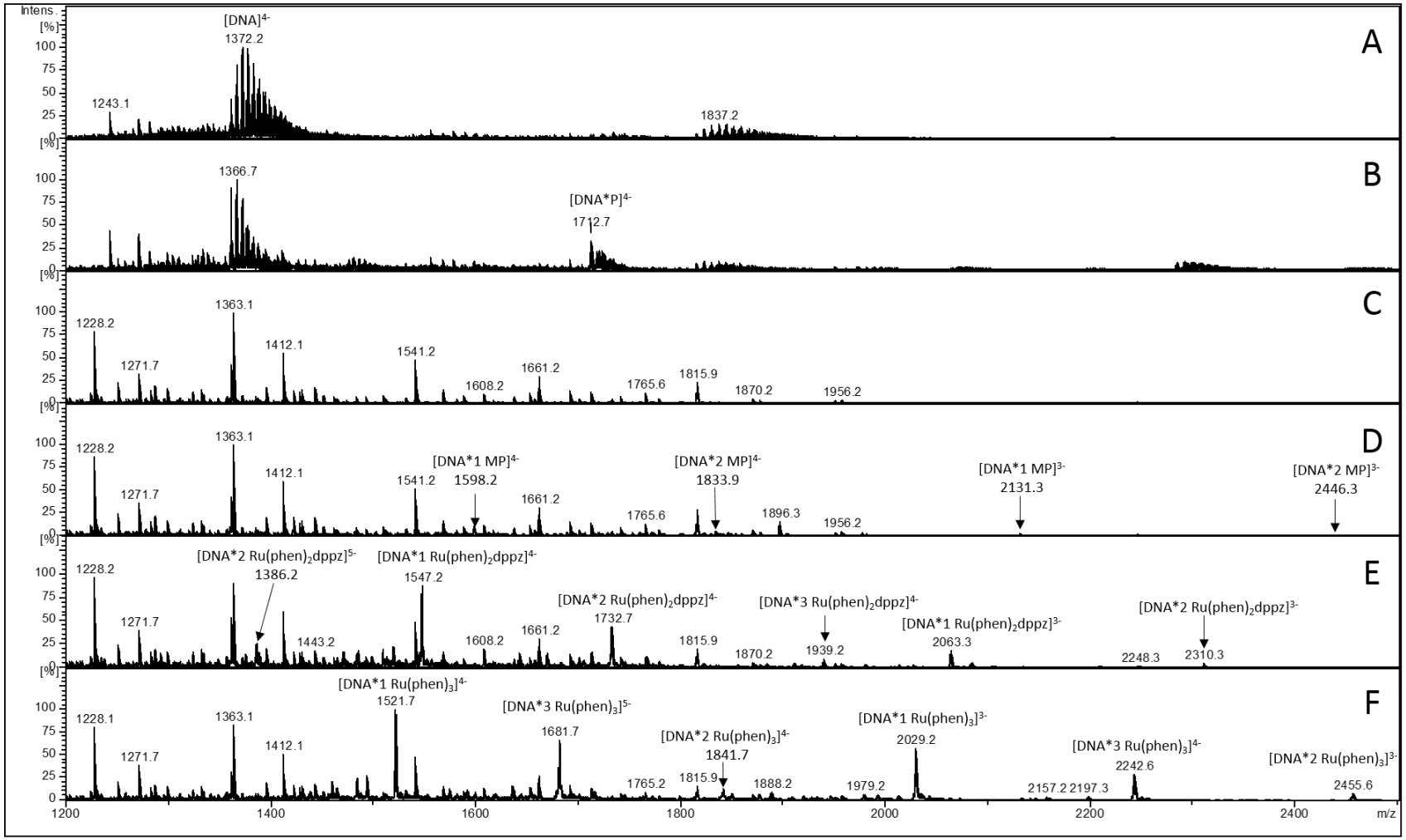

Figure 4.4 ESI-MS of free hairpin DNA and hairpin DNA incubated with a slight excess of the indicated ligand. DNA illustrated in 4B was prepared with DNA shown in 4A, while 4D, 4E, and 4F were prepared with DNA shown in 4C.

4.5 Discussion

Previous reports have indicated that 1,10-phenanthroline and related analogs are capable of interacting with DNA through an intercalative binding mode. Complexation of several phenanthroline molecules to a metal center was previously thought to have a partial intercalative mode as well (16). Chaires was able to demonstrate that $[Ru(phen)_3]^{2+}$ binding does not proceed through the classical intercalative mode, but rather through Van der Waals contacts, electrostatic interactions, and/or effects related to the solvation of DNA (16). Le *et al.* reported that $\mathbf{P^{4+}}$ was able to interact with DNA with an affinity one order of magnitude greater than the **Rp3** binding, but that the enthalpy was similar to that reported by Chaires group. Le *et al.* presented that $\mathbf{P^{4+}}$ was able to thread through the DNA base pairs by taking advantage of the "breathing" motion of DNA (14). Interestingly, the kinetics of the reaction appeared to be relatively fast for a threading mechanism, perhaps due to the dynamic flux of DNA. To further understand this intercalative binding mode, **MP**, **Rp2d,** and **Rp3** (ligand size starting at phen and building towards tatpp) were bound to 25bp duplex to examine the structure function relationship of the Ru^{2+} ligands with DNA.

As a starting point, the validity of 25 bp duplex DNA as a good model DNA was confirmed by comparing the experiments with **Rp3** in this work to the literature. For **Rp3** binding to 25 bp DNA, a similar binding affinity with respect to the previous reports for the forward titration experiment was obtained (21). Additionally the measured enthalpy agrees with the results for their **Rp3** binding (both were positive, difference was ~0.1 kcal/mol) and the entropic contribution were comparable (ΔS= 28.8 vs 26.8 cal/mol) especially considering the buffer concentrations differed from their system (16).

Further building upon the **Rp3** scaffold, the binding of **Rp2d** was examined. Two distinct binding events were noted. The first higher affinity binding of 1.2×10^6 was comparable to that reported by Chaires *et al*. (16). Interestingly this work yielded a negative enthalpy, whereas their reported enthalpy for the binding of **Rp2d** was 0.2 kcal/mol vs this work's -1.1 kcal/mol, but both obtained a favorable entropic contribution (16). The difference in enthalpy is small and possibly negligible, but could arise from a number of factors including the difference in buffer conditions or the differences arising from the use of different techniques (the entirety of the presented thermodynamic parameters were derived from ITC, whereas Chaires *et al.* only reported enthalpies from ITC and used fluorescence data for the binding constants) (16). Recent advances in microcalorimetry and the fitting models used to model the binding parameters could also explain this difference. Nevertheless, using these different models with different DNAs, similar binding affinities were obtained.

Interestingly, a secondary binding event which was not reported by Chaires *et al*. was observed. Similar results of a second binding event were seen in more recent ITC results of **Rp2d** with $(\text{poly[dAdT]})_2$ by Lincoln *et al*., where they saw two distinct binding events via ITC but did not present the values of the thermodynamic parameters of the second binding event (24). This work's ITC derived first binding site free energy change value is nearly identical to their reported value, and both determined the first binding mode to be entropically driven. The second binding mode was characterized by a more favorable enthalpic contribution, as was also stated by Lincoln *et al.*, with an almost equal entropic contribution. While we agree with the assignment of the nature of the primary ligand binding by Lincoln *et al*., we do not believe the additional mode to

simply be that of a canted geometrical binding, but rather a side-on interaction with the backbone of the DNA or a new intercalative association arising from the original intercalation which caused a widening of the minor groove (25, 26). Thermodynamically, a normal and canted intercalation should be relatively similar and instead two separate binding modes with distinctly different enthalpic and entropic contributions were observed (27). X-ray crystal structures of both Δ and Λ complexes with DNA are available and show two different binding modes for the racemic mixture (28). Additional crystal structures show the structural variance possible in bound DNA at differing relative humidities (25). It should be noted that this difference could arise from the different oligonucleotides used in the two studies. Future ITC titrations with full thermodynamic characterization of both binding events with $[poly(dAdT)]_2$ would be useful to compare these two systems. We do not believe the difference in the ITC profile to be the result of a competitive process between these two modes though, as the two are added simultaneously and the affinities for both processes are two orders of magnitude different (29).

In order to complete the link between **Rp3** and $\mathbf{P^{4+}}$ the interaction of **MP** with the model duplex DNA was examined. A slightly higher binding constant, suggesting a more favorable interaction for **MP** with duplex DNA than **Rp2d** with duplex DNA, was obtained for **MP** vs **Rp2d**. This higher association for the intercalated construct likely arises not only from the favorable **π-π** interactions of the extended conjugated system but also due to the release of unfavorable hydrophobic interactions between the ligand and solvent system (water) upon binding of the ligand to DNA. Molecular dynamics energy minimization studies show a closer relationship between the **MP** Ru^{2+} center and the

nucleotides than was observed with the modeling of $\mathbf{P}^{4+}$ complexed with the same DNA. Perhaps the majority of the additional binding energy comes from this ability to more closely associate with the backbone and have more favorable ionic interactions instead of two cationic metal centers competing for the interaction and having a less thermodynamically stable binding product.

CD titration results assisted in the confirmation of these conclusions. **Rp3** shows little to no effect on the structure of the duplex, as there is no large amount of absorbance shifts observed. Figure 4.3C shows the **Rp3** ligand associating with the grooves of DNA. Creating an extension from the phenanthroline ligand offers an intercalative ability with a higher affinity. This increased affinity for the bound mode causes structural changes through steric interactions between the bulky phenanthroline groups and the DNA backbone as well as deformation caused by the necessary increase in distance between base pairs to accommodate the intercalation. For the binding of **Rp2d** to DNA, the minor groove is likely widened to near A-form type as seen with the emergence of a positive peak near 260-270 nm, which is indicative of A-form DNA (23, 30). Figure 4.3B shows **Rp2d** intercalating into DNA from the minor groove and widening it to accommodate the phenanthroline groups lying in the grove. A minor groove binding non-intercalative mode is also demonstrated in the figure. Increasing the width of the minor groove and major grooves is necessary for relaxation of the torsional strain caused by intercalation (31).

With the case of **MP**, there is a drastic attenuation in molar ellipticity in the region of 275 nm in both buffers examined. Titrations of **MP** in phosphate buffer demonstrated emergence of a positive peak near 260-270 nm at mole ratios of ligand in

excess of the 8 expected for a 25 base pair duplex that would be able bind based on the **Rp3** exclusion observation discussed by Chaires *et al.* (21).

4.6 Conclusion

The reported ITC, ESI-MS, and CD results from the experiments serve to examine the structure function relationship of these Ru^{2+} ligands when binding with DNA. A marked increase in binding affinity for the mononuclear Ru^{2+} containing ligands that are able to intercalate versus the mononuclear **Rp3** which has been reported to not bind through classical intercalation was seen. The favorable entropic contributions likely arise from the displacement of solvent (water) upon ligand binding, as well as the unwinding of the duplex. ESI-MS data support the "neighbor exclusion principle" and exclusion based on the size of **Rp3** that has been previously reported (14, 21).

MP binds to dsDNA with an affinity 1.5 kcal/mol greater than that of $\mathbf{P^{4+}}$, while **Rp2d** binds with an affinity slightly lower than that of $\mathbf{P^{4+}}$, suggesting that a longer intercalating moiety but not additional groove binding moiety is able to enhance the binding of these Ru^{2+} containing DNA binding ligands. Future studies will examine more substituted ligands as well as the enantiomerically pure samples of **Rp2d** and **MP** in order to distinguish each enantiomers' contribution to the thermodynamic parameters.

4.7 References

1. Chien, J.; Kuang, R.; Landen, C.; Shridhar, V. Platinum-sensitive recurrence in ovarian cancer: The role of tumor microenvironment. *Frontiers in Oncology* **2013**, *3*.

2. Bergamo, A.; Sava, G. Ruthenium anticancer compounds: myths and realities of the emerging metal-based drugs. *Dalton Transactions* **2011**, *40*, 7817-7823.

3. Eckstein, N. Platinum resistance in breast and ovarian cancer cell lines. *Journal of Experimental & Clinical Cancer Research* **2011**, *30*, 1-11.

4. Dickerson, M.; Howerton, B.; Bae, Y.; C. Glazer, E. Light-sensitive ruthenium complex-loaded cross-linked polymeric nanoassemblies for the treatment of cancer. *Journal of Materials Chemistry B* **2016**, *4*, 394-408.

5. Antonarakis, E. S.; Emadi, A. Ruthenium-based chemotherapeutics: are they ready for prime time? *Cancer Chemotherapy and Pharmacology* **2010**, *66*, 1-9.

6. Hartinger, C. G.; Jakupec, M. A.; Zorbas-Seifried, S.; Groessl, M.; Egger, A.; Berger, W.; Zorbas, H.; Dyson, P. J.; Keppler, B. K. KP1019, A New Redox-Active Anticancer Agent – Preclinical Development and Results of a Clinical Phase I Study in Tumor Patients. *Chemistry & Biodiversity* **2008**, *5*, 2140-2155.

7. Yadav, A.; Janaratne, T.; Krishnan, A.; Singhal, S. S.; Yadav, S.; Dayoub, A. S.; Hawkins, D. L.; Awasthi, S.; MacDonnell, F. M. Regression of lung cancer by hypoxia-sensitizing ruthenium polypyridyl complexes. *Molecular Cancer Therapeutics* **2013**, *12*, 643-653.

8. Boynton, A. N.; Marcélis, L.; Barton, J. K. $[Ru(Me_4(phen))_2dppz]^{2+}$, a Light Switch for DNA Mismatches. *Journal of the American Chemical Society* **2016**, *138*, 5020-5023

9. Bouskila, A.; Amouyal, E.; Verchère-Béaur, C.; Sasaki, I.; Gaudemer, A. Mononuclear and binuclear ruthenium(II) heteroleptic complexes based on 1,10-phenanthroline ligands. Part II: Spectroscopic and photophysical study in the presence of DNA. *Journal of Photochemistry and Photobiology B: Biology* **2004**, *76*, 69-83.

10. Kelly, J. M.; McConnell, D. J.; OhUigin, C.; Tossi, A. B.; Mesmaeker, A. K.-D.; Masschelein, A.; Nasielski, J. Ruthenium polypyridyl complexes; their interaction with DNA and their role as sensitisers for its photocleavage. *Journal of the Chemical Society, Chemical Communications* **1987**, 1821-1823.

11. Gill, M. R.; Thomas, J. A. Ruthenium(II) polypyridyl complexes and DNA-from structural probes to cellular imaging and therapeutics. *Chemical Society Reviews* **2012**, *41*, 3179-3192.

12. Friedman, A. E.; Chambron, J. C.; Sauvage, J. P.; Turro, N. J.; Barton, J. K. A molecular light switch for DNA: $Ru(bpy)_2(dppz)^{2+}$. *Journal of the American Chemical Society* **1990**, *112*, 4960-4962.

13. Williams, K. J.; Cowen, R. L.; Stratford, I. J. Hypoxia and oxidative stress in breast cancer: Tumour hypoxia – therapeutic considerations. *Breast Cancer Research* **2001**, *3*, 1-4.

14. Le, V. H.; McGuire, M. R.; Ahuja, P.; MacDonnell, F. M.; Lewis, E. A. Thermodynamic investigations of $[(phen)_2Ru(tatpp)Ru(phen)_2]^{4+}$ interactions with B-DNA. *Journal of Physical Chemistry B* **2015**, *119*, 65-71.

15. Le, V. H.; Buscaglia, R.; Chaires, J. B.; Lewis, E. A. Modeling complex equilibria in isothermal titration calorimetry experiments: Thermodynamic parameters estimation for a three-binding-site model. *Analytical Biochemistry* **2013**, *434*, 233-241.

16. Haq, I.; Lincoln, P.; Suh, D.; Norden, B.; Chowdhry, B. Z.; Chaires, J. B. Interaction of .DELTA.- and .LAMBDA.-$[Ru(phen)_2(dppz)]^{2+}$ with DNA: A Calorimetric and Equilibrium Binding Study. *Journal of the American Chemical Society* **1995**, *117*, 4788-4796.

17. Chothers, D. M. Calculation of binding isotherms for heterogeneous polymers. *Biopolymers* **1968**, *6*, 575-584.

18. Bond, P. J.; Langridge, R.; Jennette, K. W.; Lippard, S. J. X-ray fiber diffraction evidence for neighbor exclusion binding of a platinum metallointercalation reagent to DNA. *Proceedings of the National Academy of Sciences of the United States of America* **1975**, *72*, 4825-4829.

19. Carvlin, M. J.; Fiel, R. J. Intercalative and nonintercalative binding of large cationic porphyrin ligands to calf thymus DNA. *Nucleic Acids Research* **1983**, *11*, 6121-6139.

20. Carvlin, M. J.; Mark, E.; Fiel, R.; Howard, J. C. Intercalative and nonintercalative binding of large cationic porphyrin ligands to polynucleotides. *Nucleic Acids Research* **1983**, *11*, 6141-6154.

21. Satyanarayana, S.; Dabrowiak, J. C.; Chaires, J. B. Neither delta- nor lambda-tris(phenanthroline)ruthenium(II) binds to DNA by classical intercalation. *Biochemistry* **1992**, *31*, 9319-9324.

22. Satyanarayana, S.; Dabrowiak, J. C.; Chaires, J. B. Tris(phenanthroline)ruthenium(II) enantiomer interactions with DNA: mode and specificity of binding. *Biochemistry* **1993**, *32*, 2573-2584.

23. Chang, Y. M.; Chen, C. K.; Hou, M. H. Conformational changes in DNA upon ligand binding monitored by circular dichroism. *Int J Mol Sci* **2012**, *13*, 3394-3413.

24. Andersson, J.; Fornander, L. H.; Abrahamsson, M.; Tuite, E.; Nordell, P.; Lincoln, P. Lifetime heterogeneity of DNA-bound dppz complexes originates from distinct intercalation geometries determined by complex-complex interactions. *Inorg Chem* **2013**, *52*, 1151-1159.

25. Hall, J. P.; Sanchez-Weatherby, J.; Alberti, C.; Quimper, C. H.; O'Sullivan, K.; Brazier, J. A.; Winter, G.; Sorensen, T.; Kelly, J. M.; Cardin, D. J.; Cardin, C. J. Controlled Dehydration of a Ruthenium Complex–DNA Crystal Induces Reversible DNA Kinking. *Journal of the American Chemical Society* **2014**, *136*, 17505-17512.

26. Biver, T.; Cavazza, C.; Secco, F.; Venturini, M. The two modes of binding of $(Ru(phen)_2dppz)^{2+}$ to DNA: Thermodynamic evidence and kinetic studies. *Journal of Inorganic Biochemistry* **2007**, *101*, 461-469.

27. Pérez-Arnaiz, C.; Busto, N.; Leal, J. M.; García, B. New Insights into the Mechanism of the DNA/Doxorubicin Interaction. *The Journal of Physical Chemistry B* **2014**, *118*, 1288-1295.

28. Hall, J. P.; Cook, D.; Morte, S. R.; McIntyre, P.; Buchner, K.; Beer, H.; Cardin, D. J.; Brazier, J. A.; Winter, G.; Kelly, J. M.; Cardin, C. J. X-ray Crystal Structure of rac-$[Ru(phen)_2dppz]^{2+}$ with $d(ATGCAT)^{2+}$ Shows Enantiomer Orientations and Water Ordering. *Journal of the American Chemical Society* **2013**, *135*, 12652-12659.

29. Bazzicalupi, C.; Biagini, S.; Bianchi, A.; Biver, T.; Boggioni, A.; Giorgi, C.; Gratteri, P.; Malavolti, M.; Secco, F.; Valtancoli, B.; Venturini, M. DNA interaction with Ru(II) and Ru(II)/Cu complexes containing azamacrocycle and dppz residues. A thermodynamic, kinetic and theoretical study. *Dalton Transactions* **2010**, *39*, 9838-9850.

30. Kypr, J.; Kejnovská, I.; Renčiuk, D.; Vorlíčková, M. Circular dichroism and conformational polymorphism of DNA. *Nucleic Acids Research* **2009**, *37*, 1713-1725.

31. Monnot, M.; Mauffret, O.; Lescot, E.; Fermandjian, S. Probing intercalation and conformational effects of the anticancer drug 2-methyl-9-hydroxyellipticinium acetate in DNA fragments with circular dichroism. *European Journal of Biochemistry* **1992**, *204*, 1035-1039.

APPENDIX A

SUPPLEMENTARY INFORMATION FOR CHAPTER III

A.1 Complete ITC titration profiles

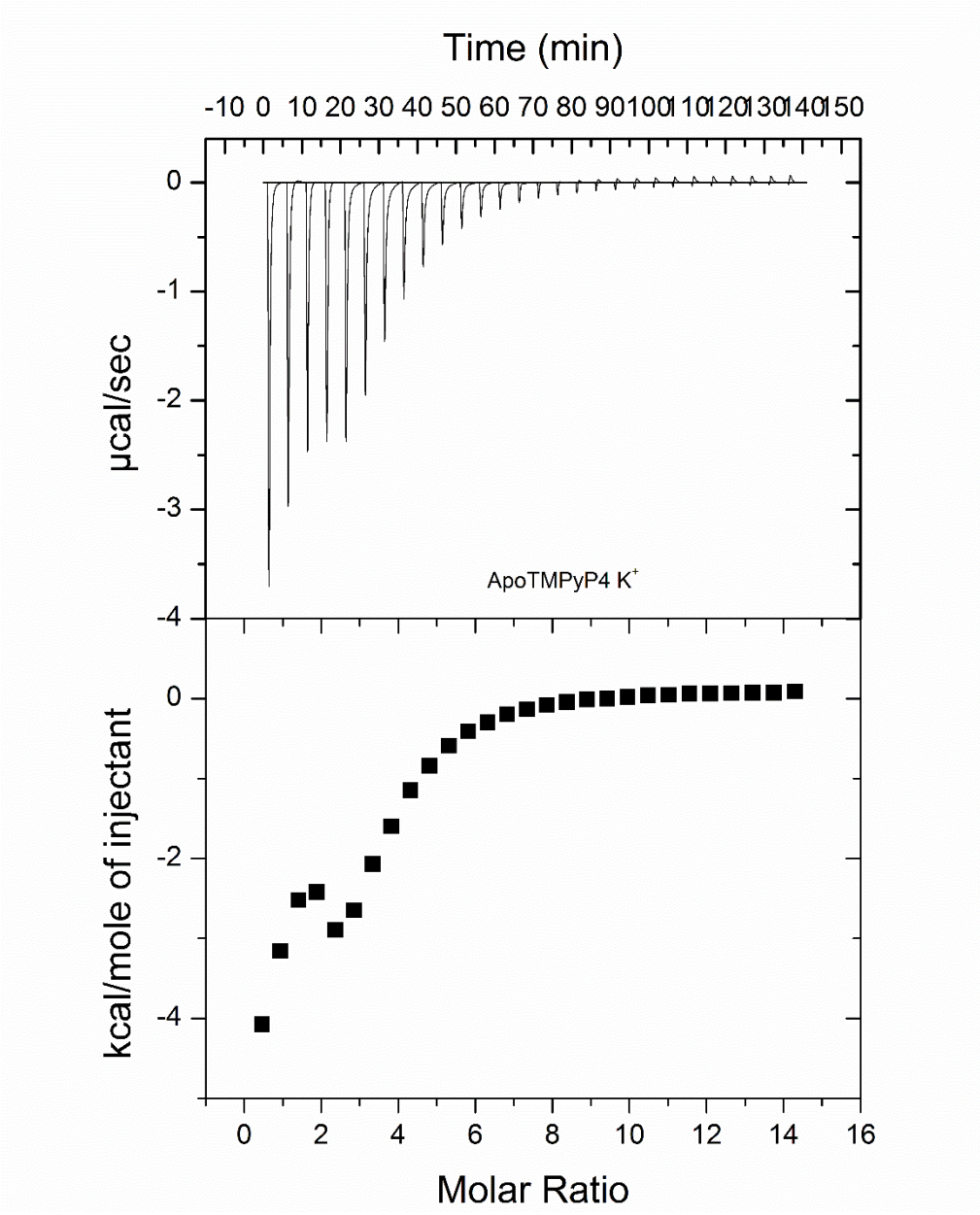

Figure A.1 Representative ITC titration profile for the titration of apo-TMPyP4 into hTel22 in 150 mM K^+ BPES buffer.

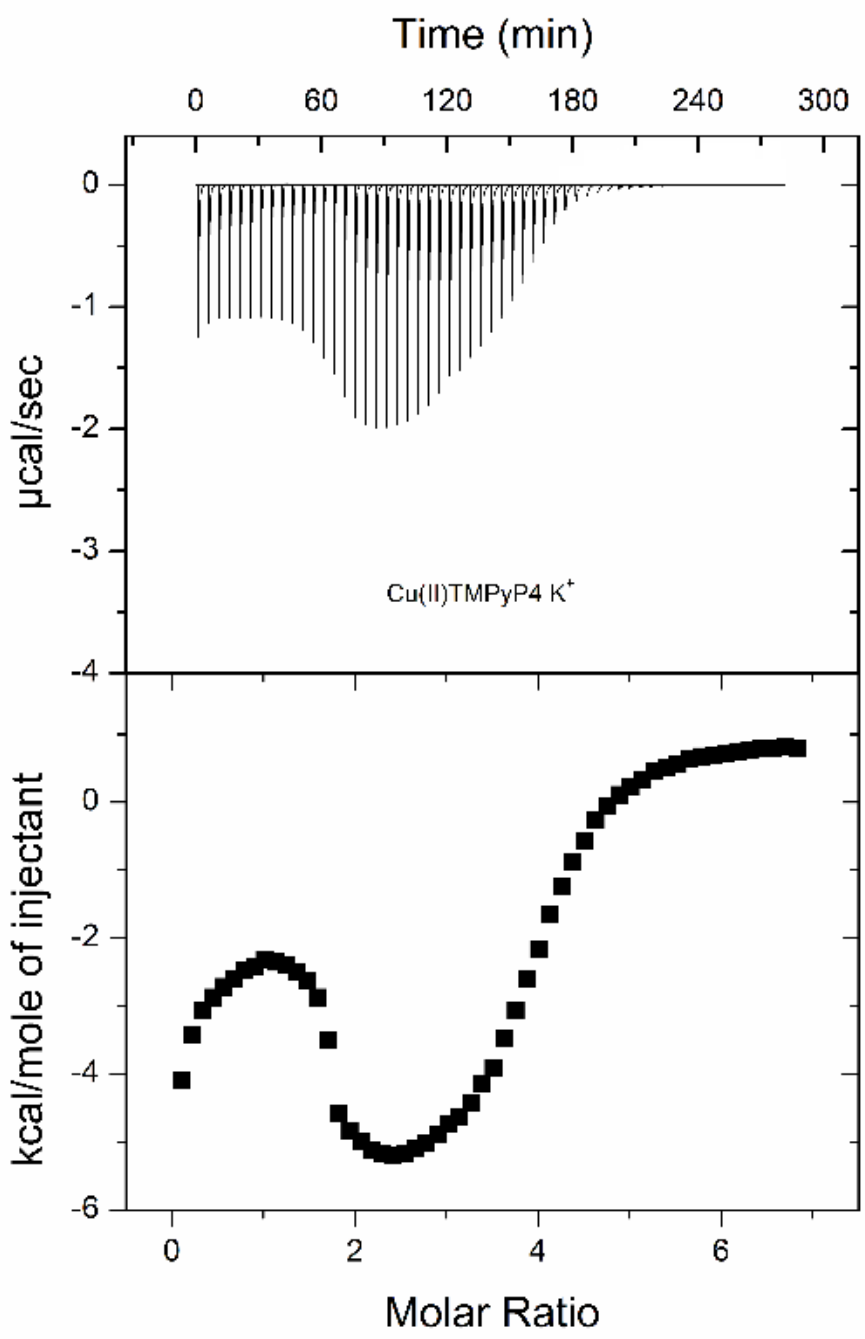

Figure A.2 Representative ITC titration profile for the titration of Cu-TMPyP4 into hTel22 in 150 mM K^+ BPES buffer.

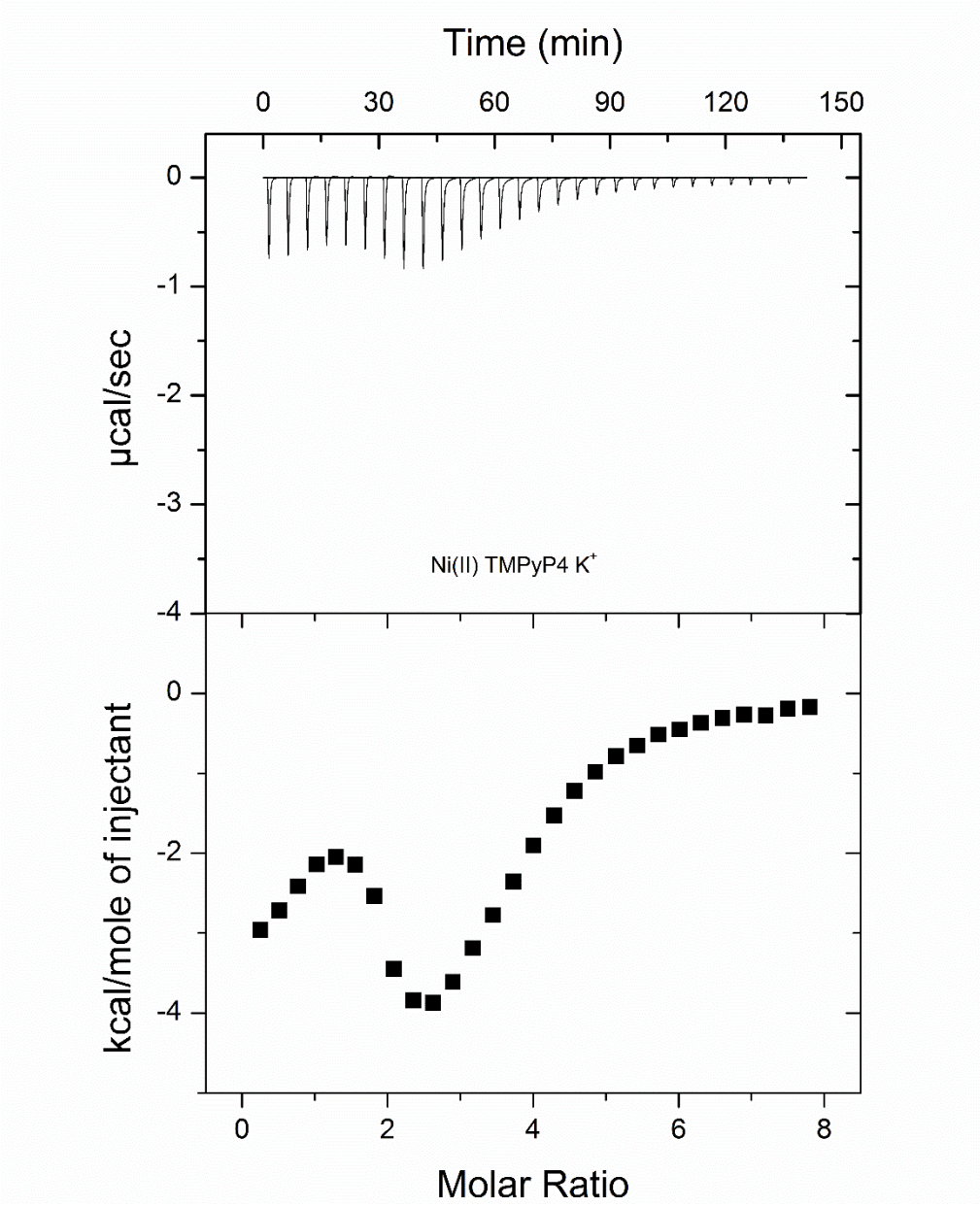

Figure A.3 Representative ITC titration profile for the titration of Ni-TMPyP4 into hTel22 in 150 mM K^+ BPES buffer.

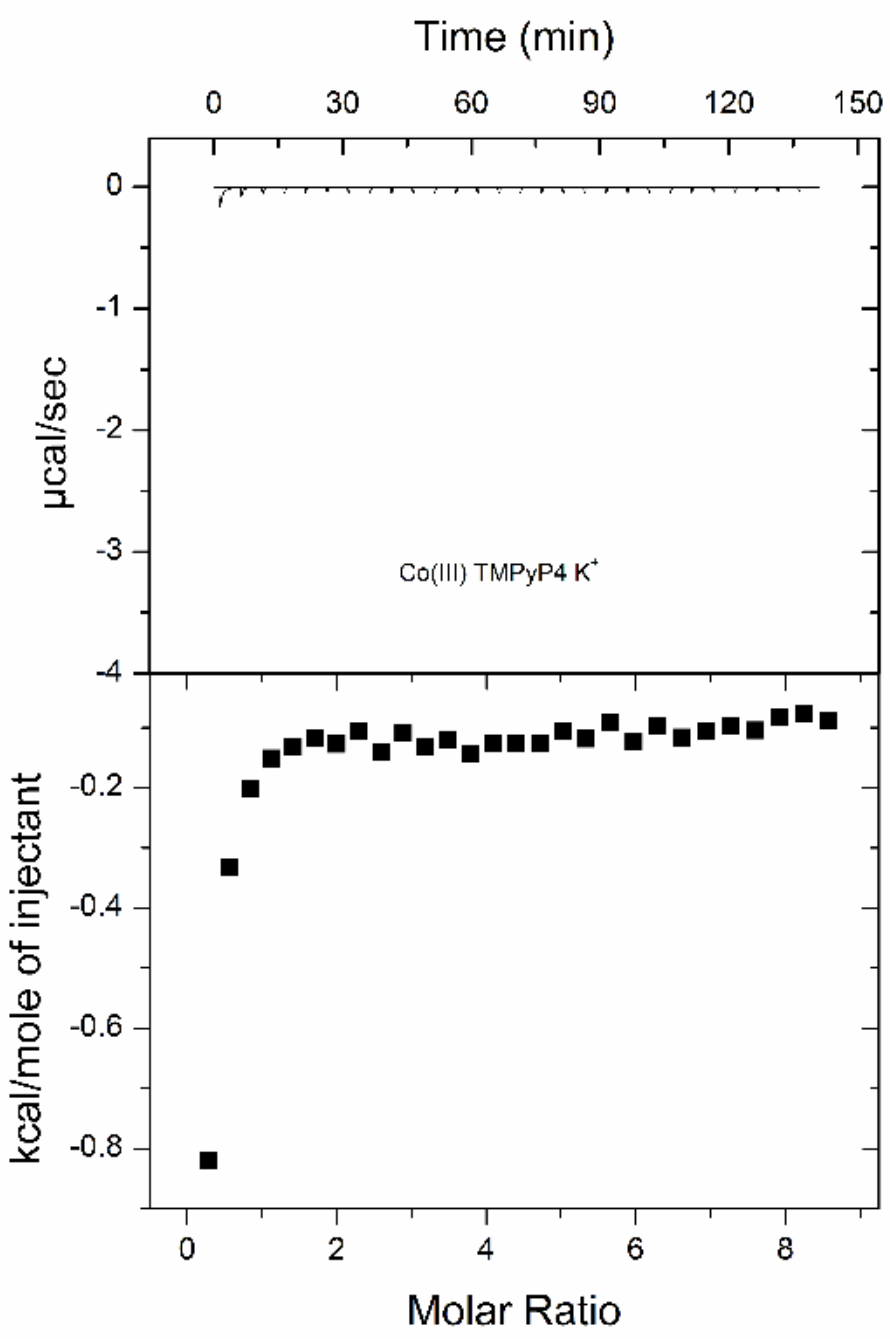

Figure A.4 Representative ITC titration profile for the titration of Co-TMPyP4 into hTel22 in 150 mM K^+ BPES buffer.

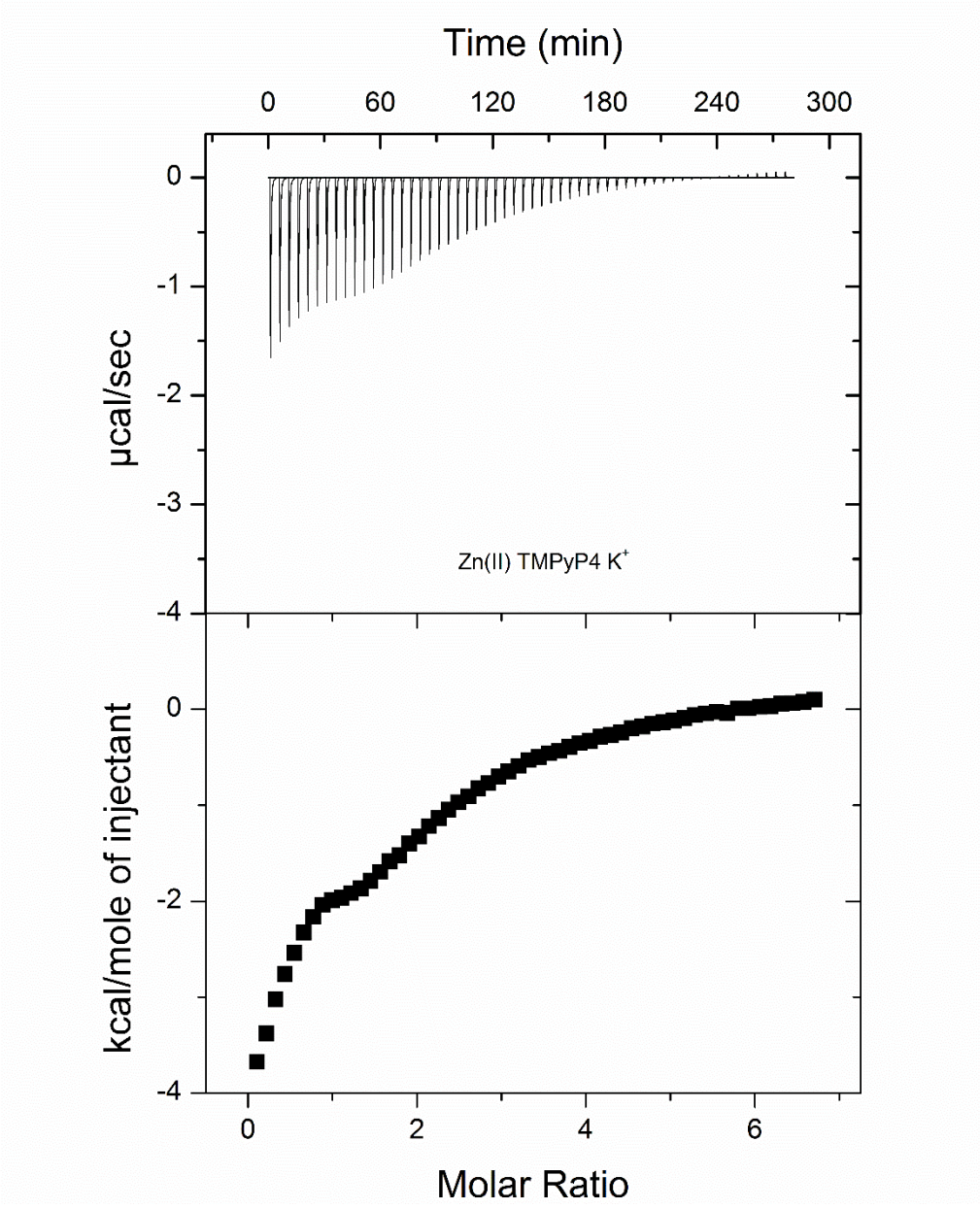

Figure A.5 Representative ITC titration profile for the titration of Zn-TMPyP4 into hTel22 in 150 mM K^+ BPES buffer.

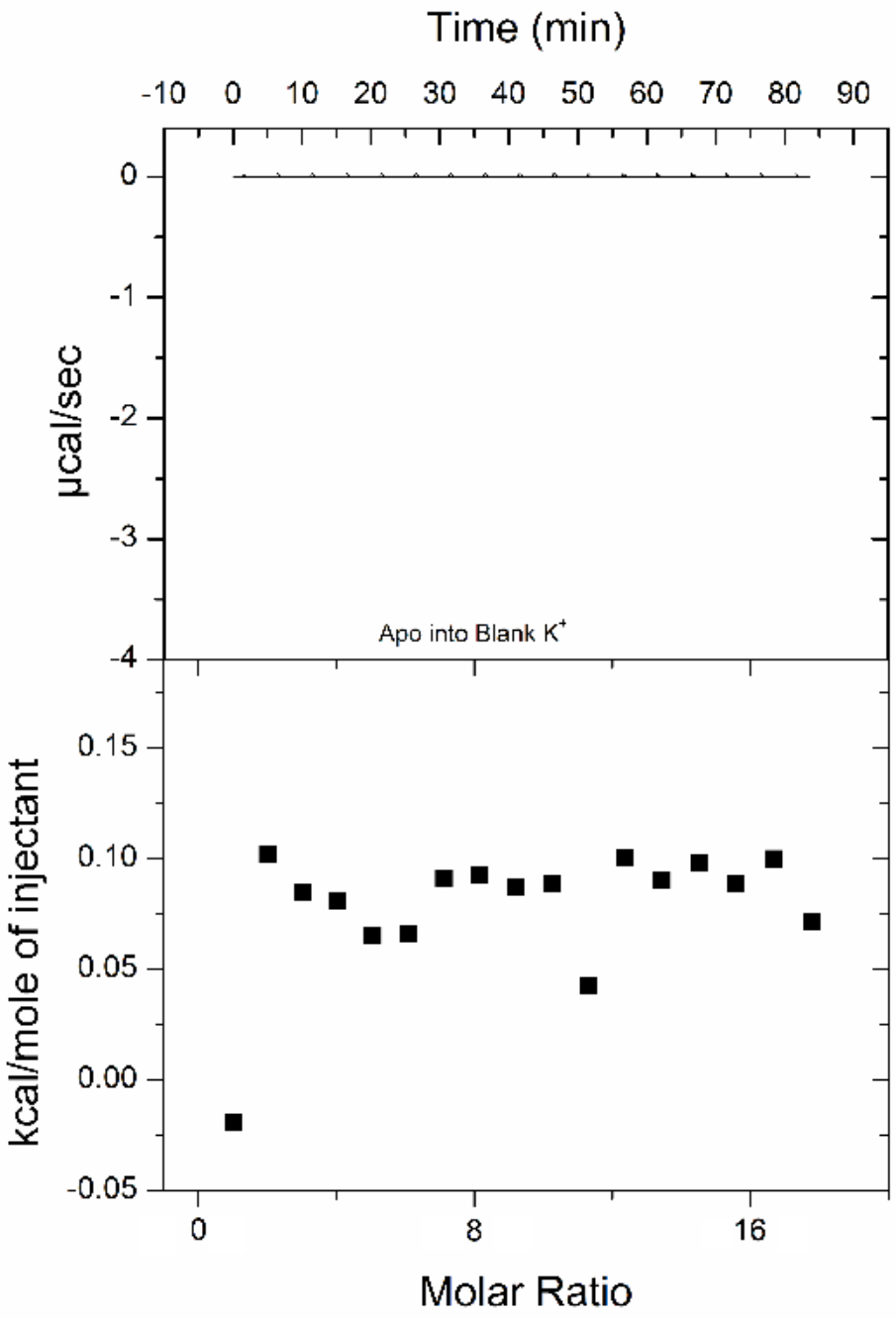

Figure A.6 Representative titration profile for the dilution of apo-TMPyP4 in 150 mM K^+ BPES buffer. Note the low endothermic heats of dilution seen.

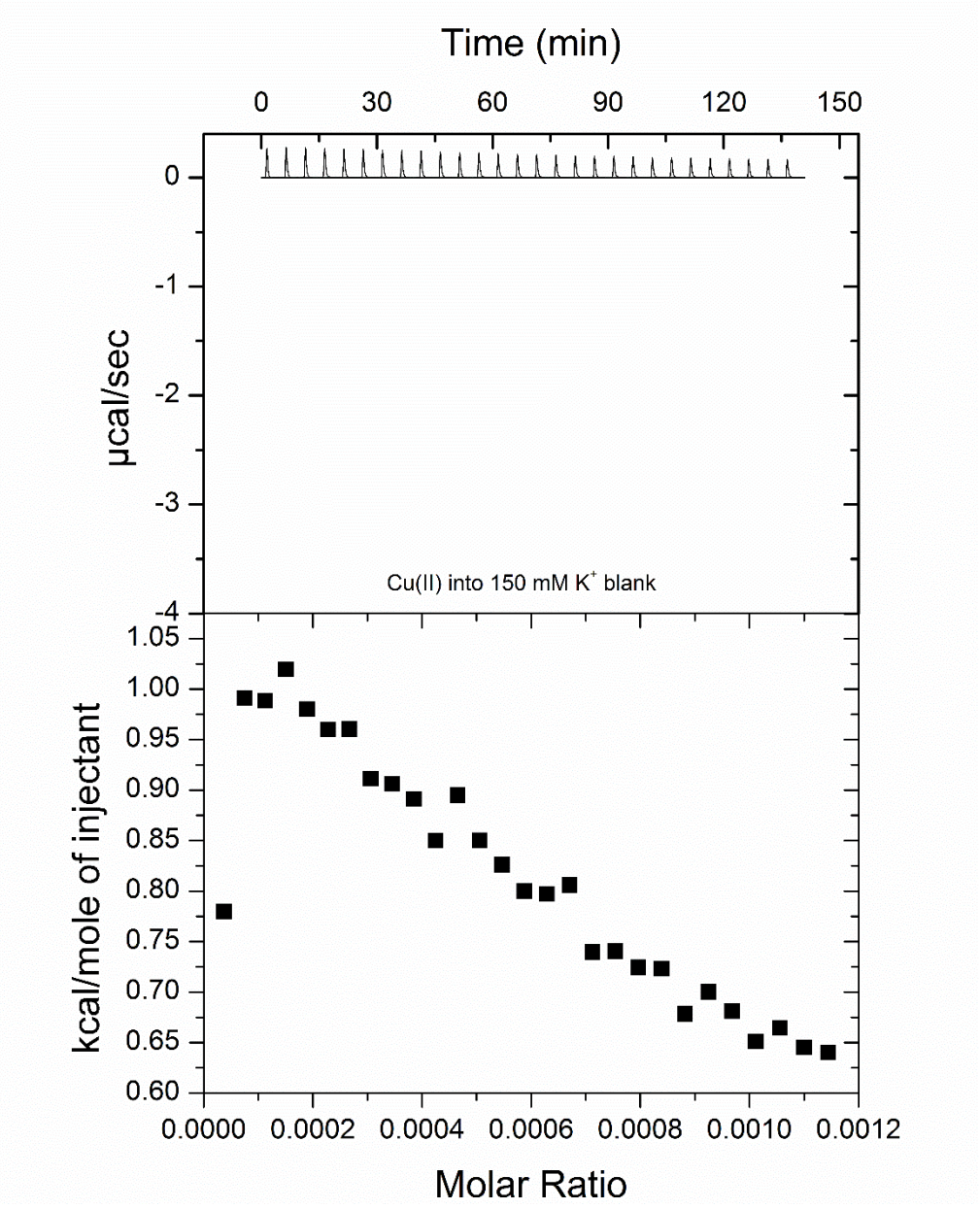

Figure A.7 Representative titration profile for the dilution of Cu-TMPyP4 in 150 mM K^+ BPES buffer.

Note the linearly decreasing endothermic heats of dilution seen.

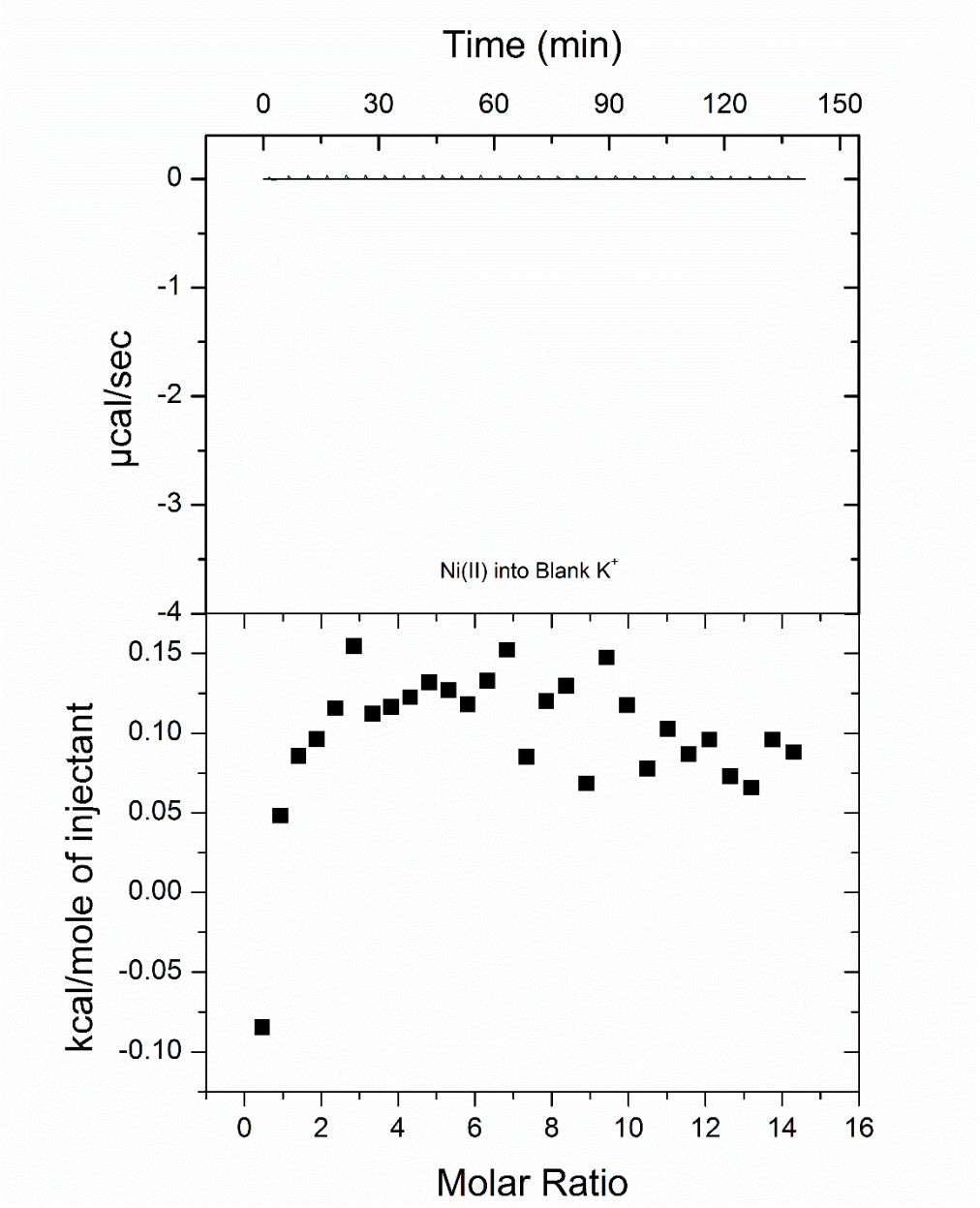

Figure A.8 Representative titration profile for the dilution of Ni-TMPyP4 in 150 mM K^+ BPES buffer. Note the low endothermic heats of dilution seen.

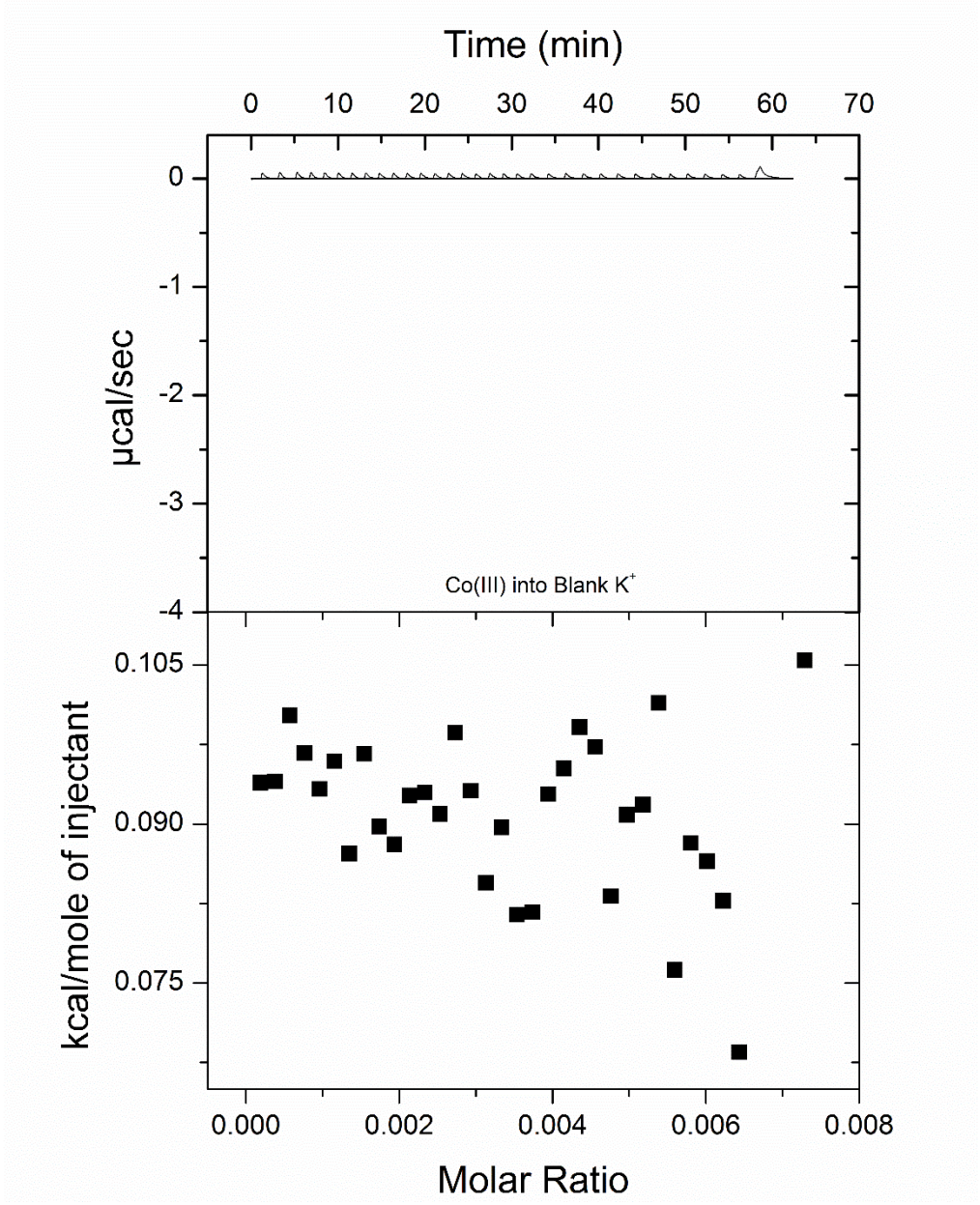

Figure A.9 Representative titration profile for the dilution of Co-TMPyP4 in 150 mM K^+ BPES buffer. Note the low endothermic heats of dilution seen.

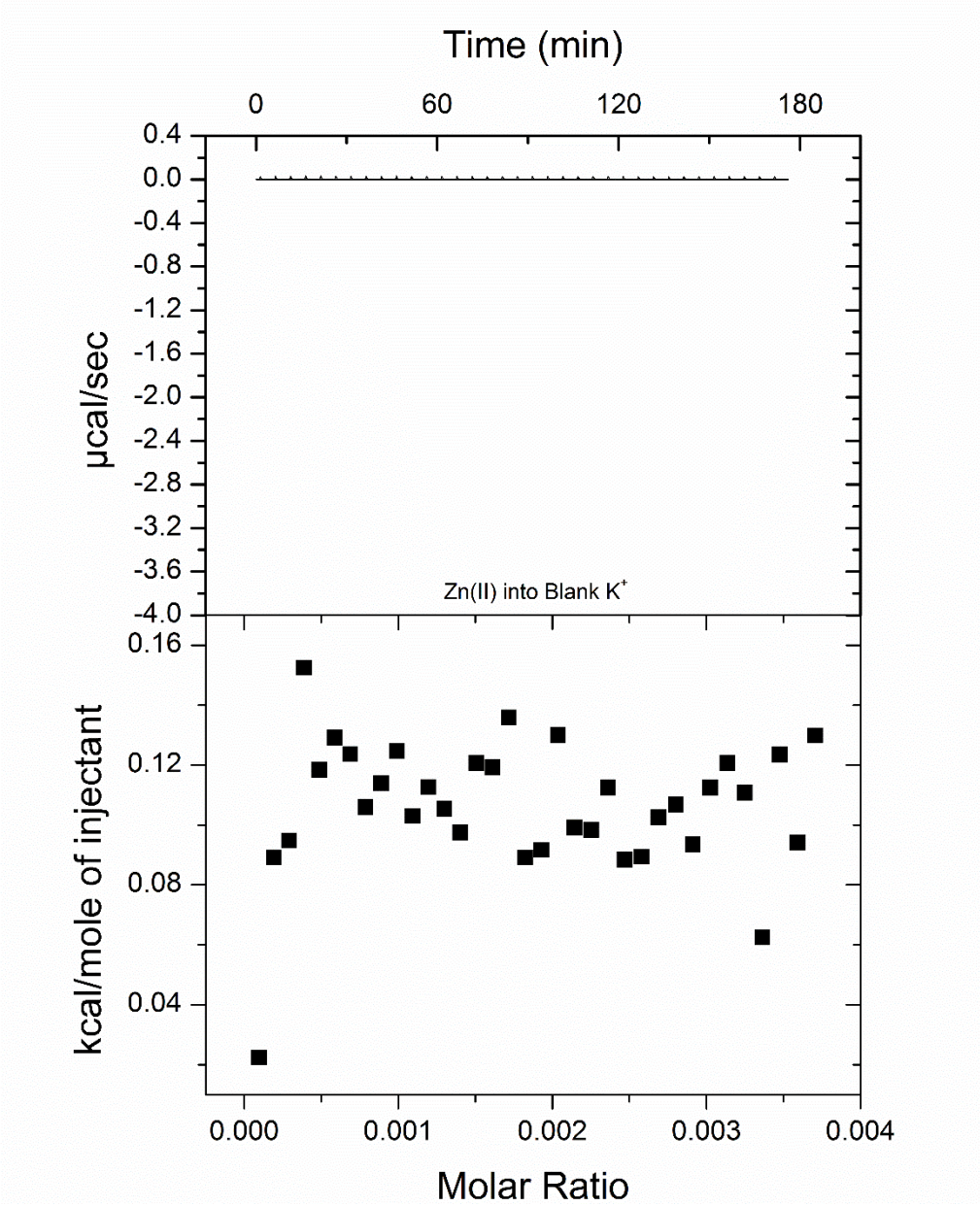

Figure A.10 Representative titration profile for the dilution of Zn-TMPyP4 in 150 mM K^+ BPES buffer. Note the low endothermic heats of dilution seen

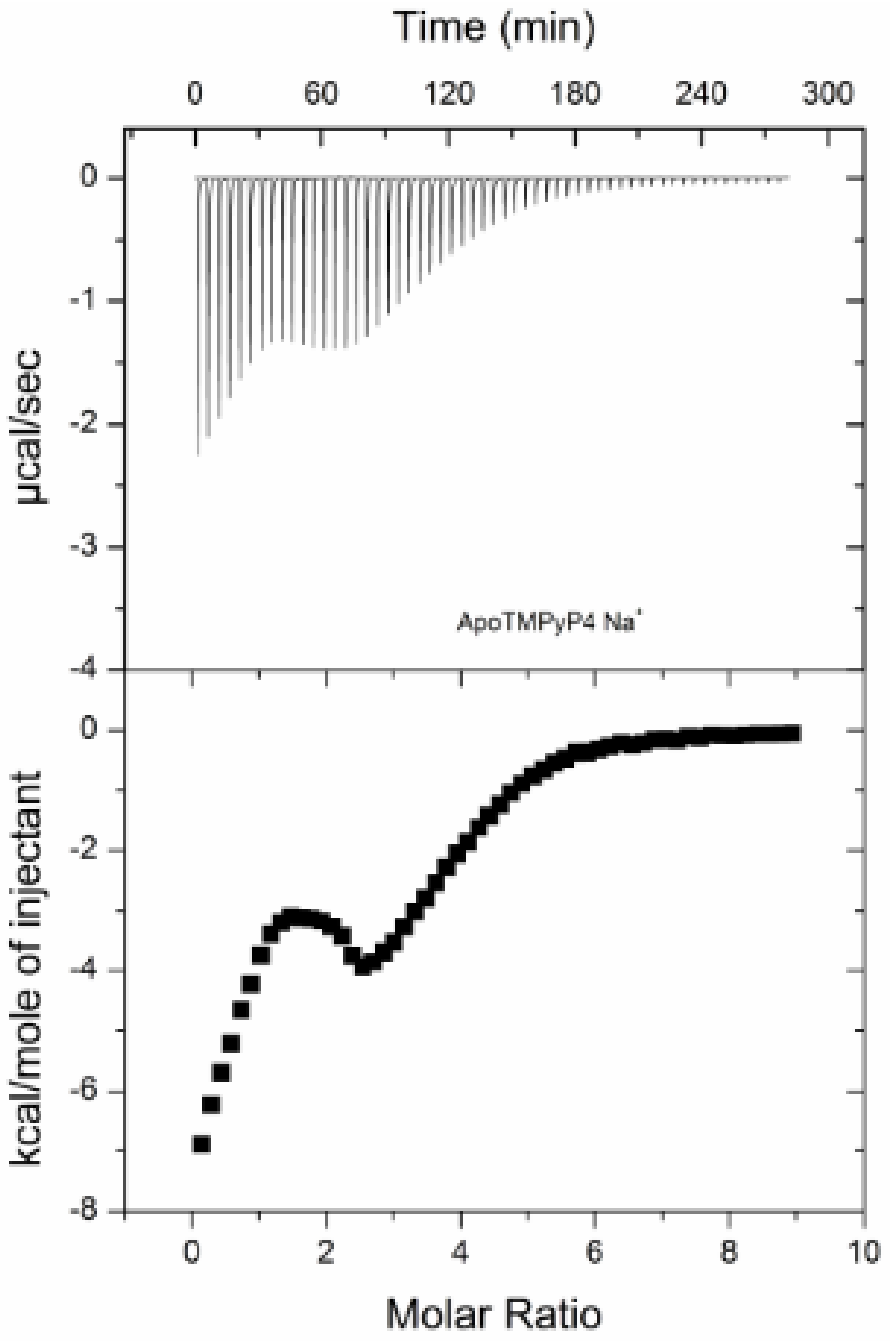

Figure A.11 Representative ITC titration profile for the titration of apo-TMPyP4 into hTel22 in 150 mM Na^+ BPES buffer.

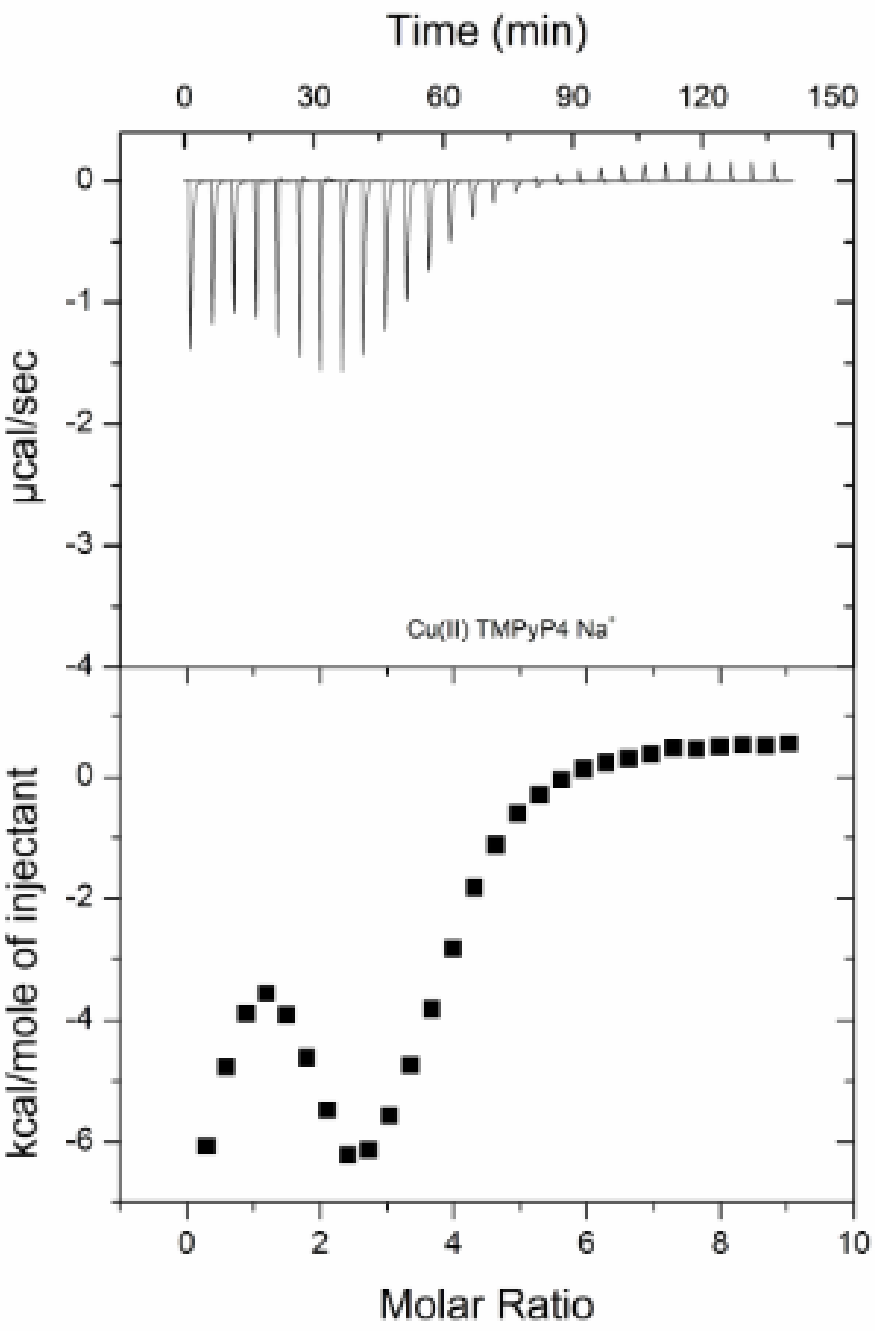

Figure A.12 Representative ITC titration profile for the titration of Cu-TMPyP4 into hTel22 in 150 mM Na^+ BPES buffer.

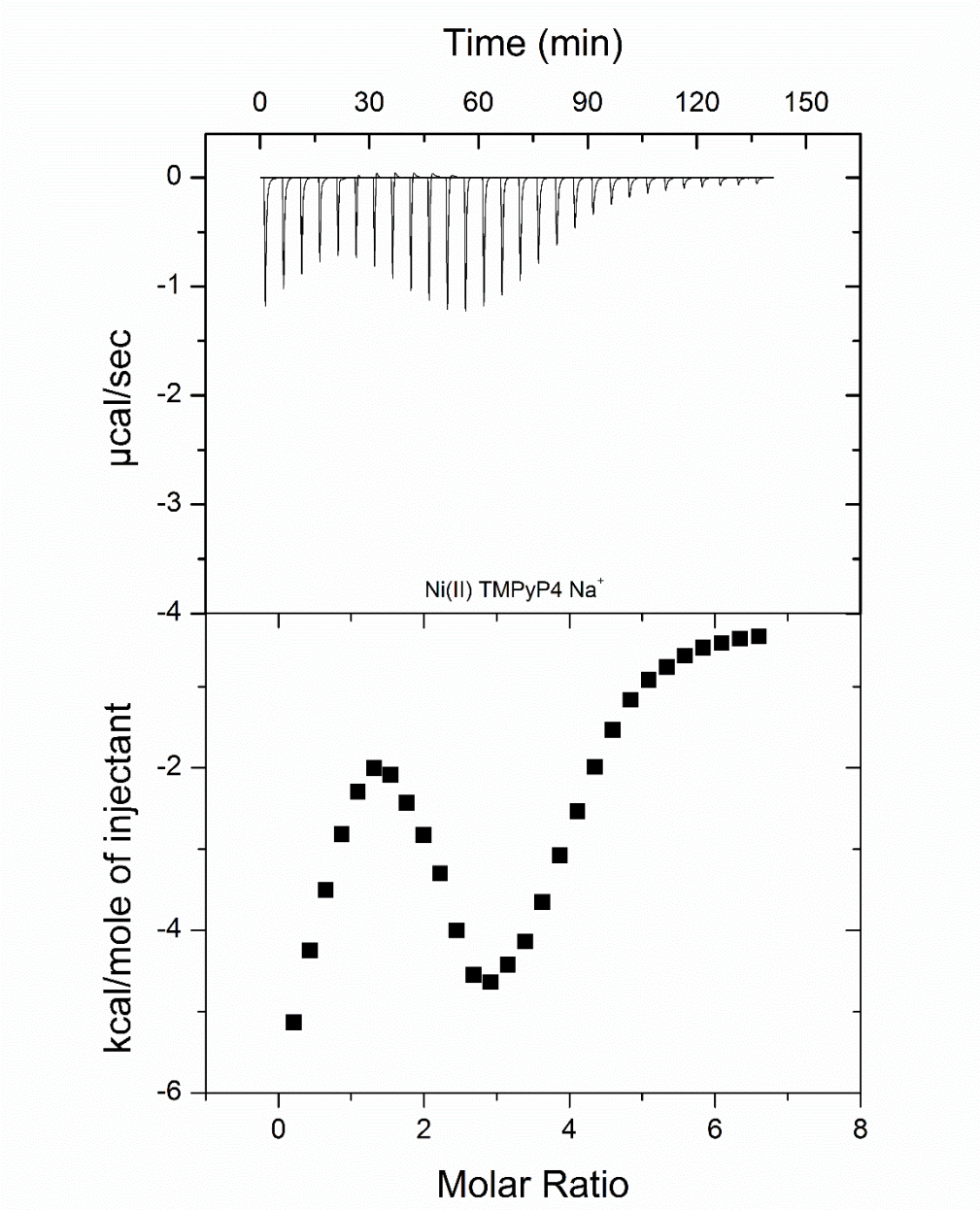

Figure A.13 Representative ITC titration profile for the titration of Ni-TMPyP4 into hTel22 in 150 mM Na^+ BPES buffer.

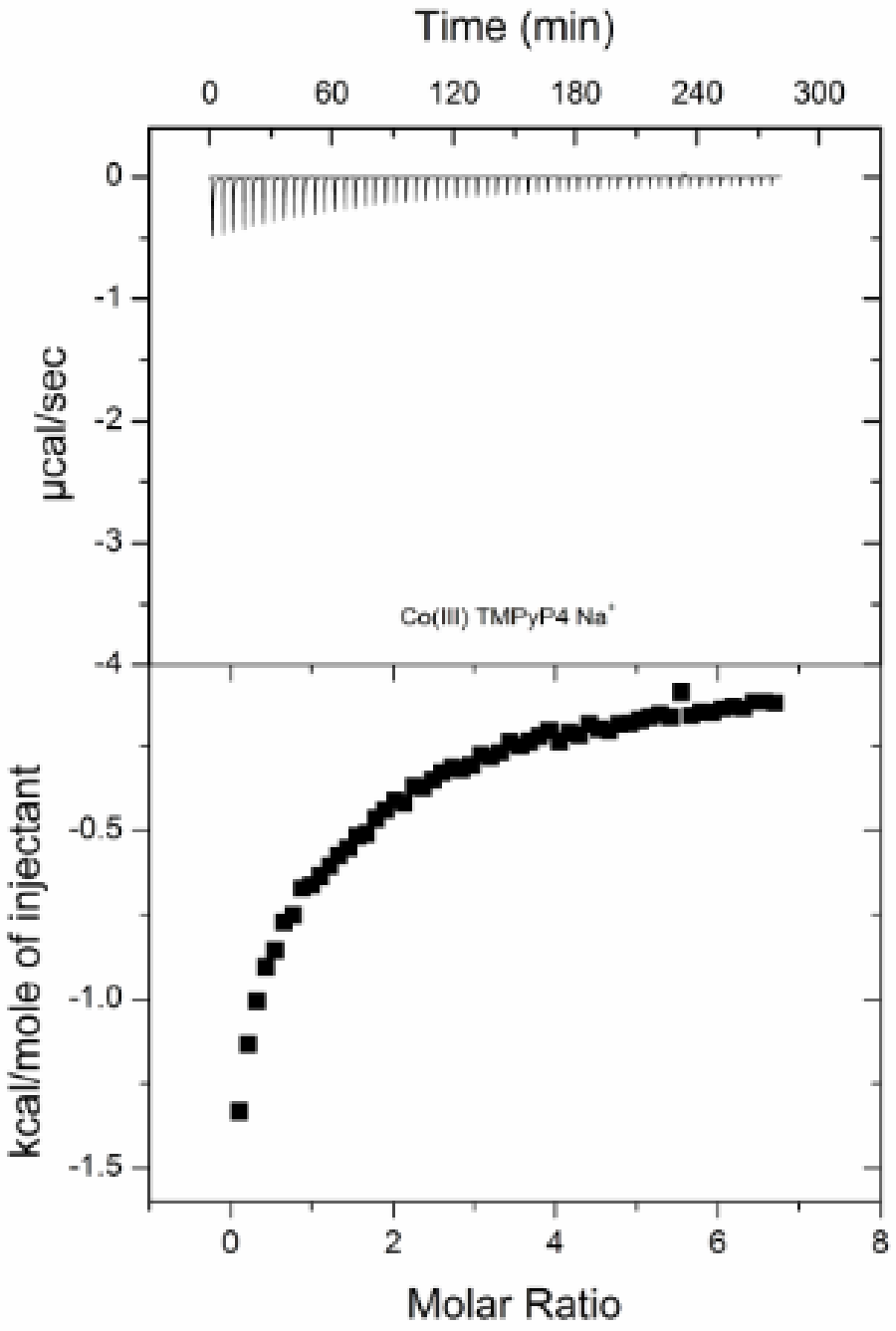

Figure A.14 Representative ITC titration profile for the titration of Co-TMPyP4 into hTel22 in 150 mM Na^+ BPES buffer.

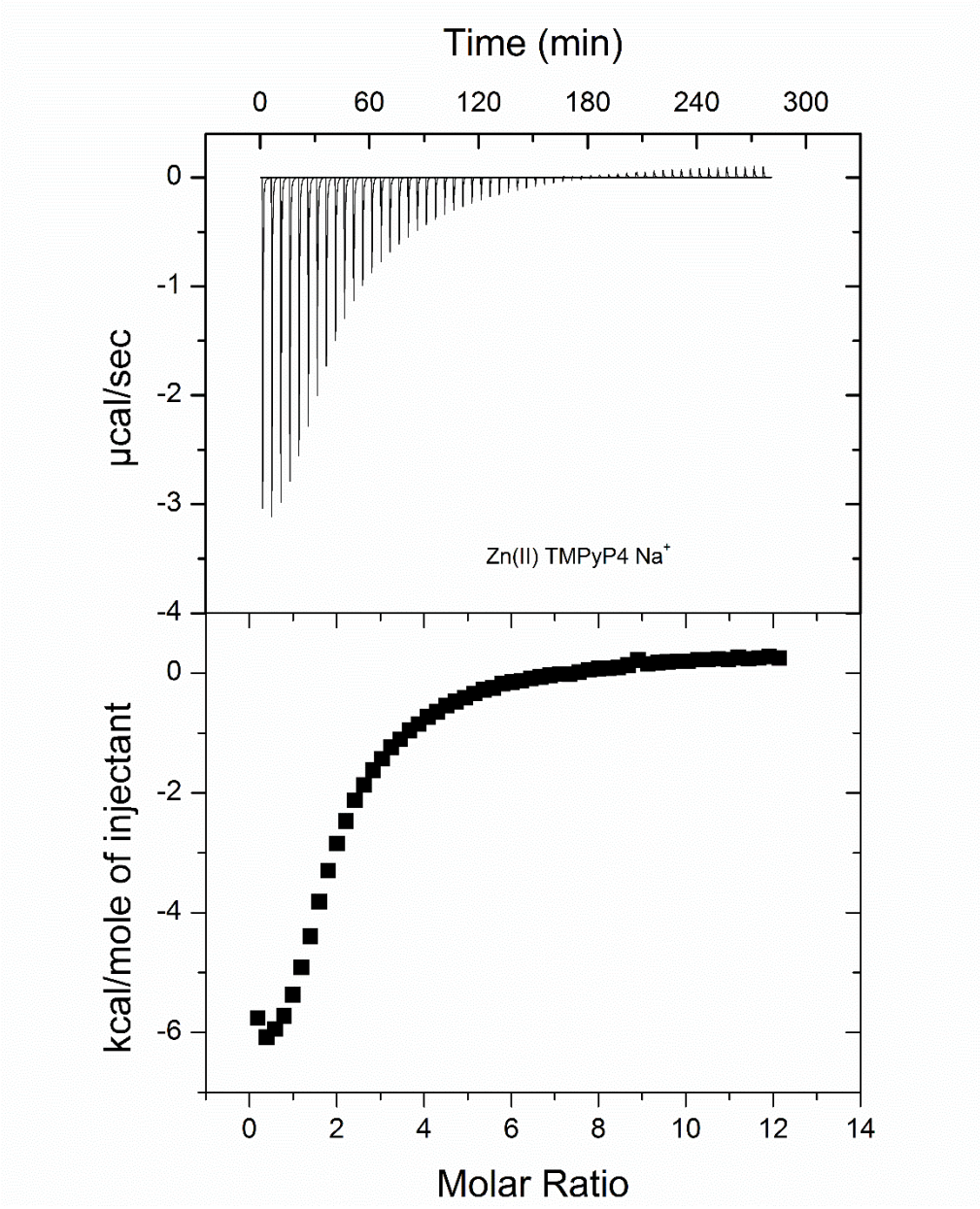

Figure A.15 Representative ITC titration profile for the titration of Zn-TMPyP4 into hTel22 and in 150 mM Na^+ BPES buffer.

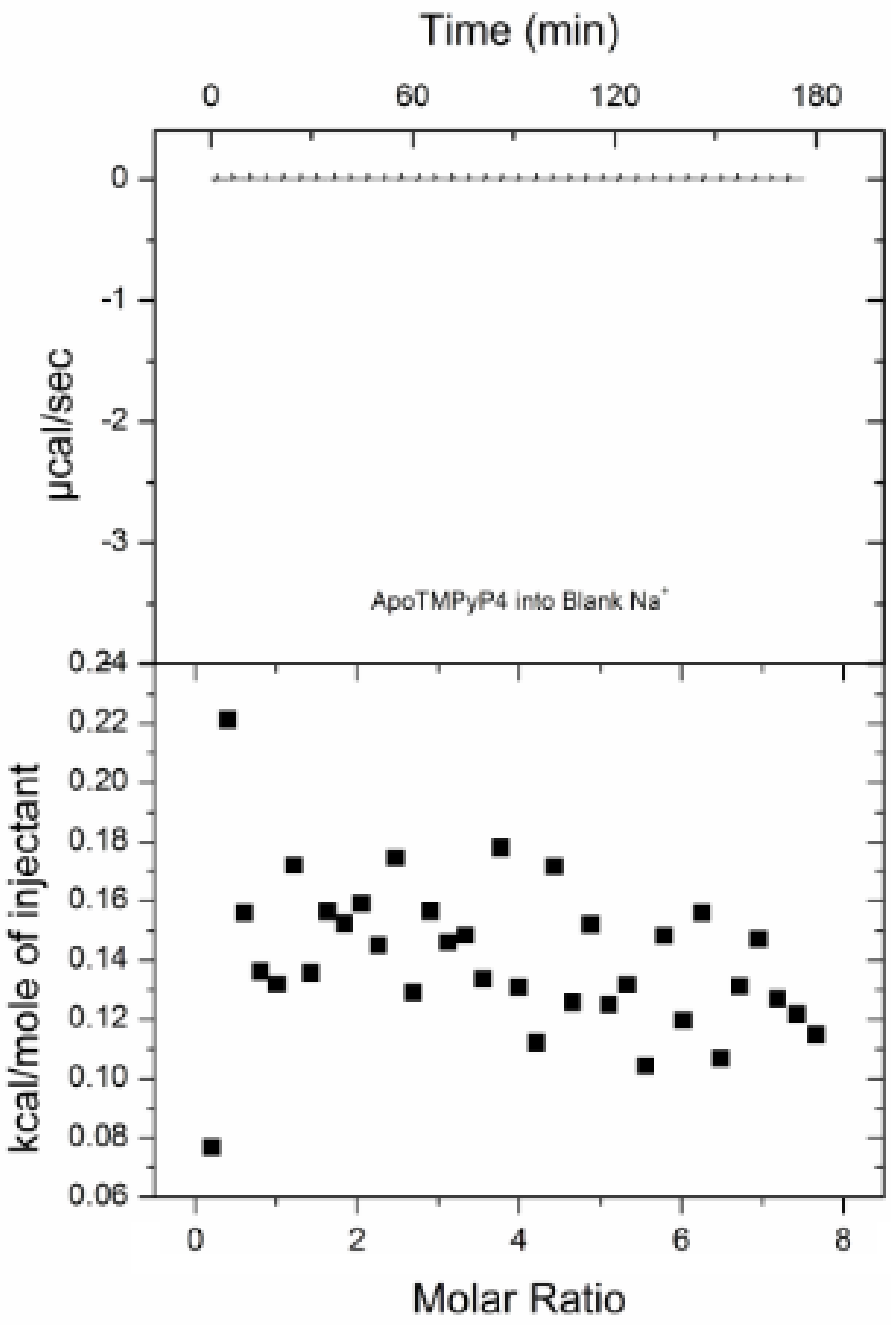

Figure A.16 Representative ITC titration profile for the dilution of apo-TMPyP4 in 150 mM Na^+ BPES buffer.

Note the low endothermic heats of dilution seen.

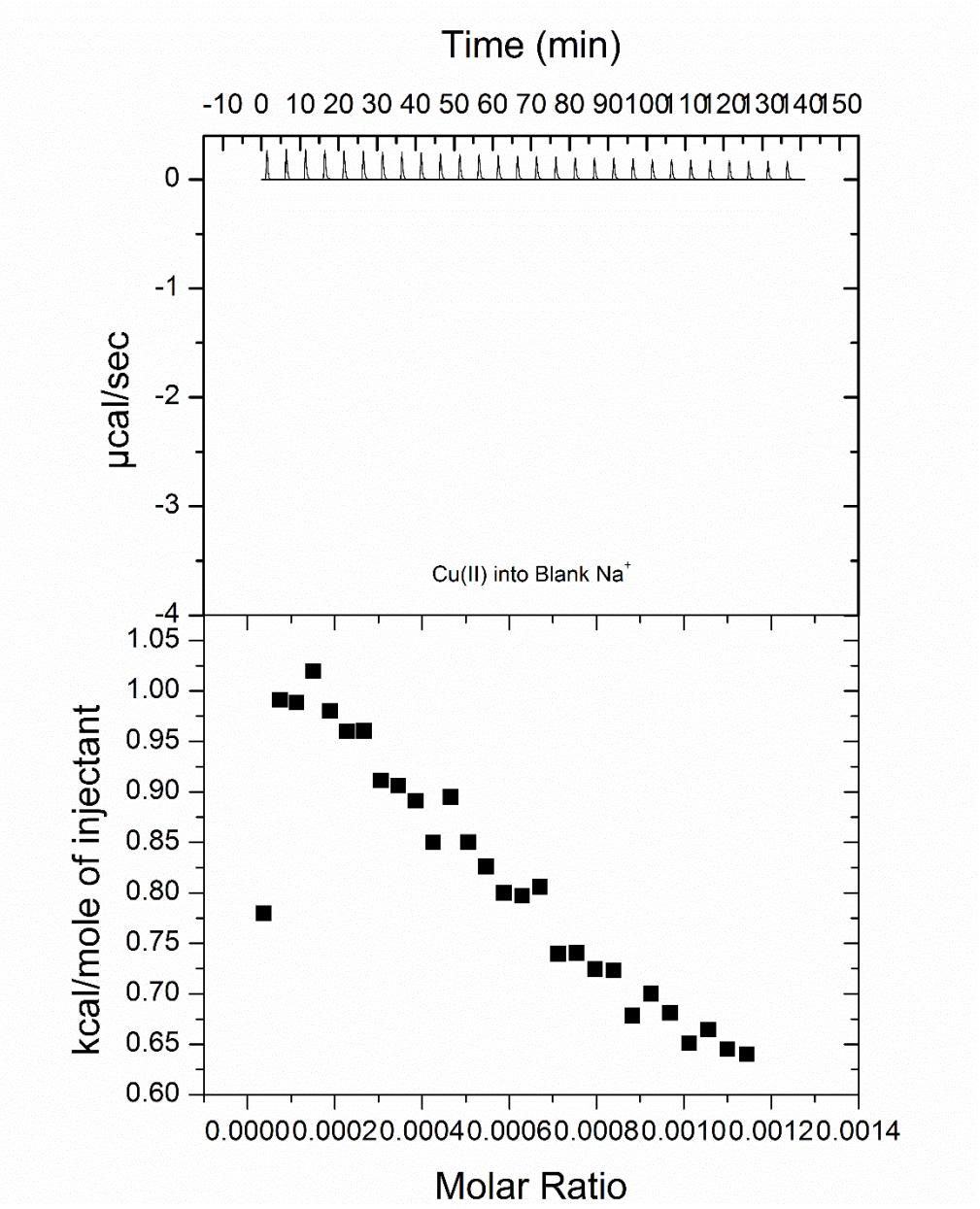

Figure A.17 Representative titration profile for the dilution of Cu-TMPyP4 in 150 mM Na^+ BPES buffer.

Note the linearly decreasing, low endothermic heats of dilution seen.

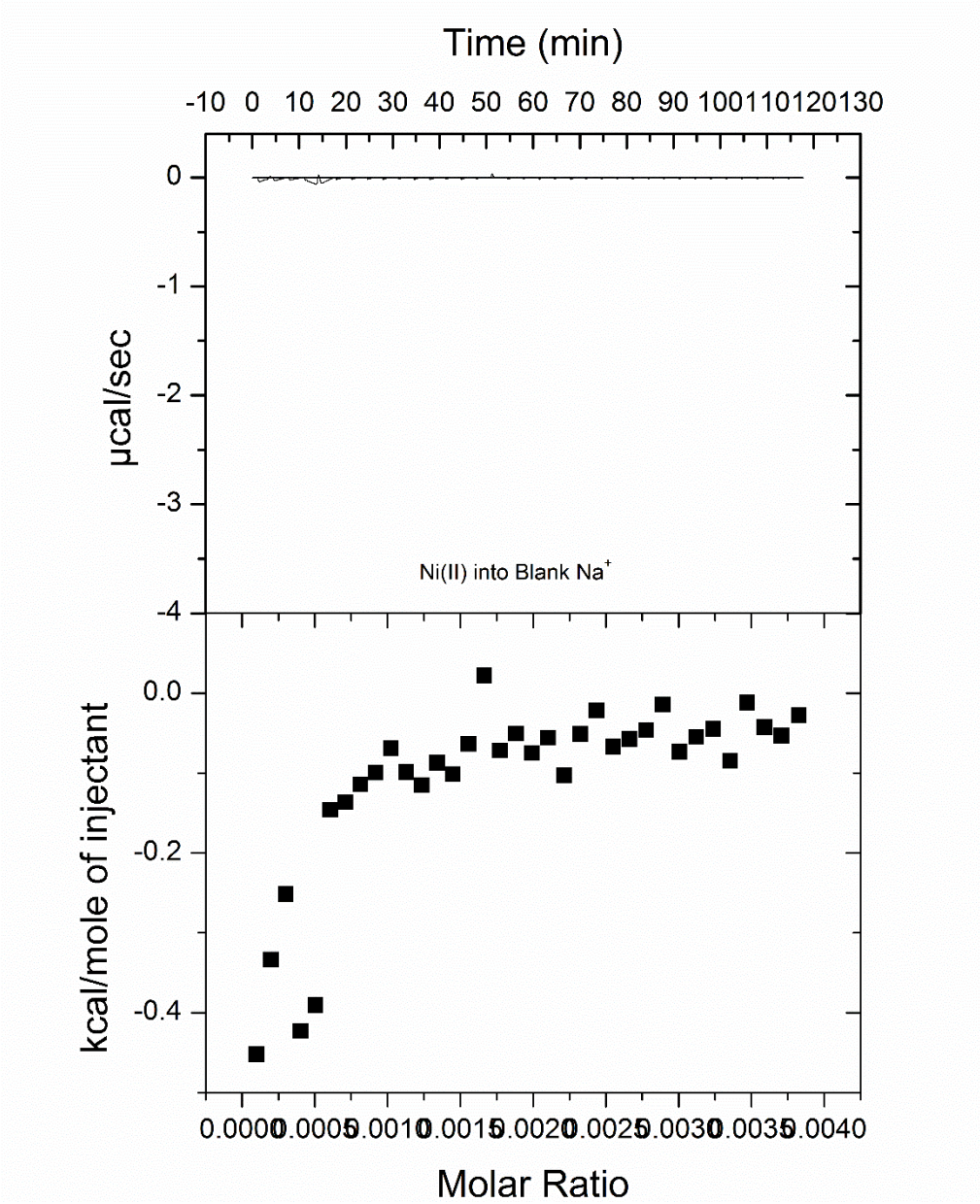

Figure A.18 Representative titration profile for the dilution of Ni-TMPyP4 in 150 mM Na^+ BPES buffer.

Note the low exothermic heats of dilution seen.

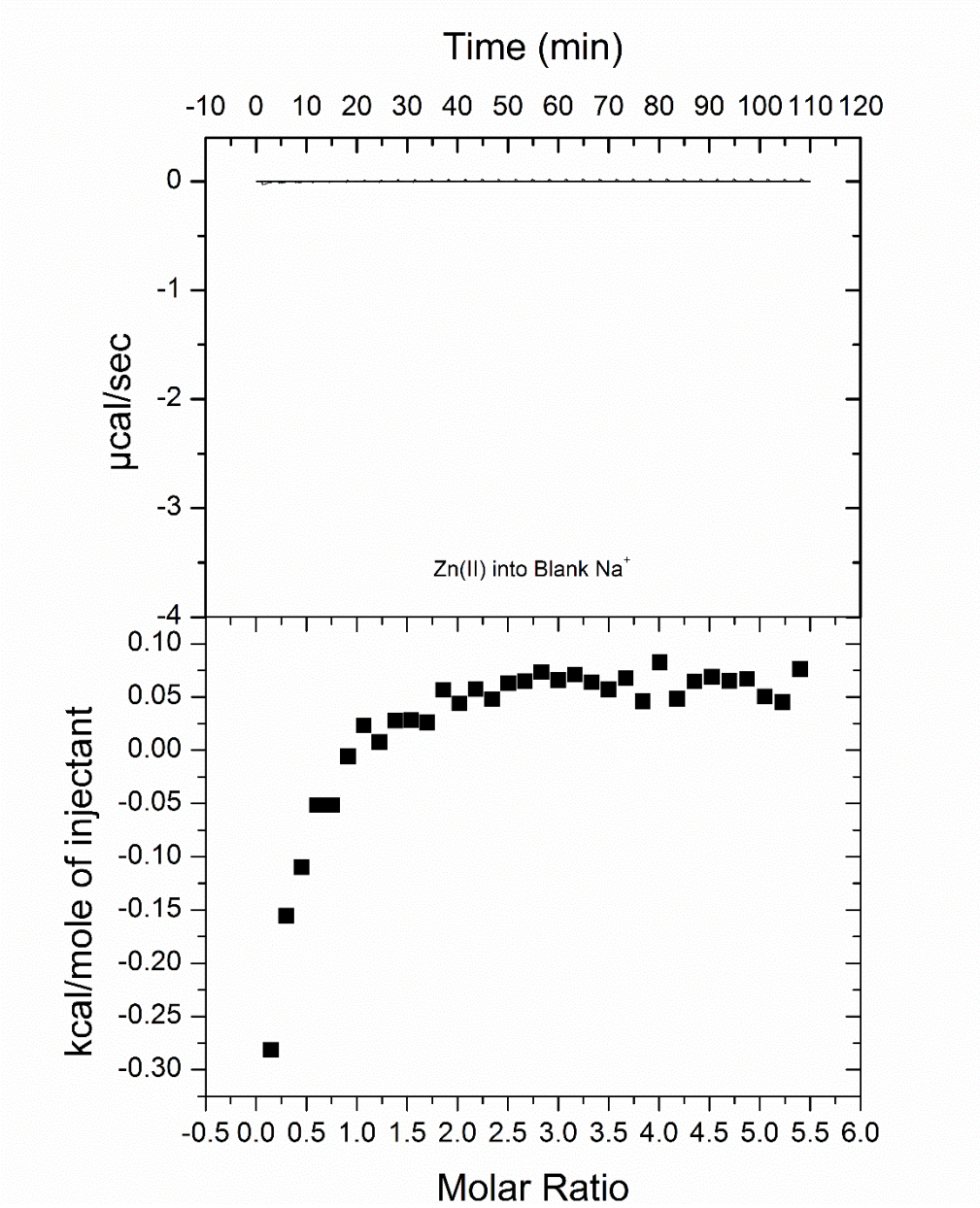

Figure A.19 Representative titration profile for the dilution of Zn-TMPyP4 in 150 mM Na^+ BPES buffer.

Note the low heats of dilution seen

A.2 Titrations at 60 mM supporting electrolyte

In addition to the published work, titrations at 60 mM supporting electrolyte concentration were performed. Below are those data compared to the published data for apo-, Cu-, and Zn-TMPyP4

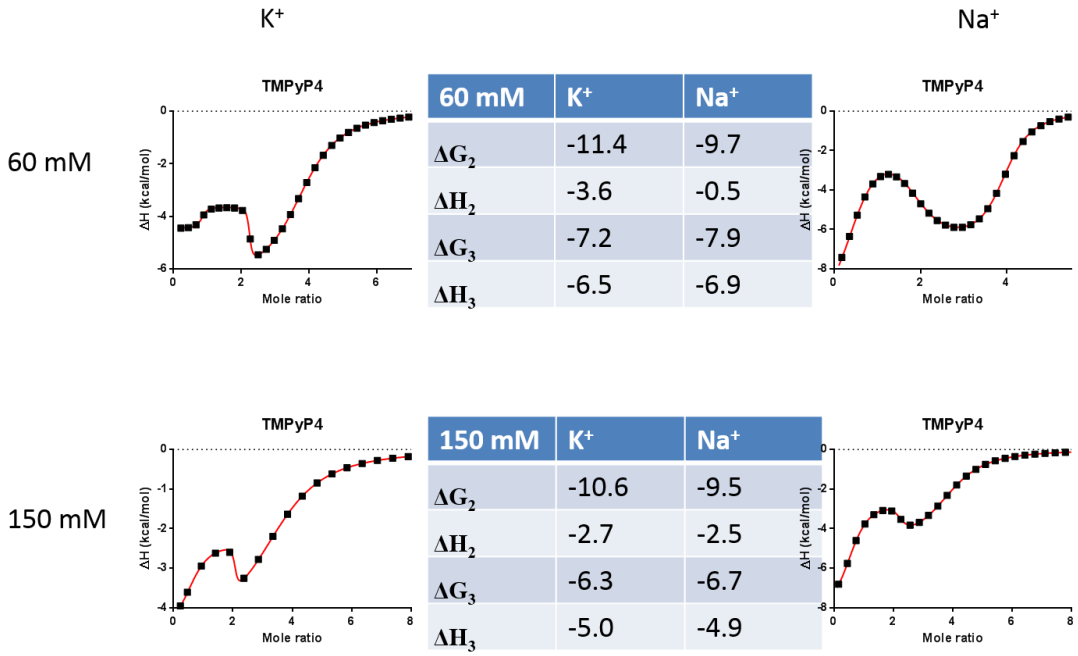

60 mM	K+	Na+
ΔG_2	-11.4	-9.7
ΔH_2	-3.6	-0.5
ΔG_3	-7.2	-7.9
ΔH_3	-6.5	-6.9

150 mM	K+	Na+
ΔG_2	-10.6	-9.5
ΔH_2	-2.7	-2.5
ΔG_3	-6.3	-6.7
ΔH_3	-5.0	-4.9

Figure A.20 Representative ITC titration enthalpogram for the titration of apo-TMPyP4 into hTel22 in 60 or 150 mM Na^+ or K^+ BPES buffer.

Changes in Gibbs free energies and enthalpies are given in kcal/mol.

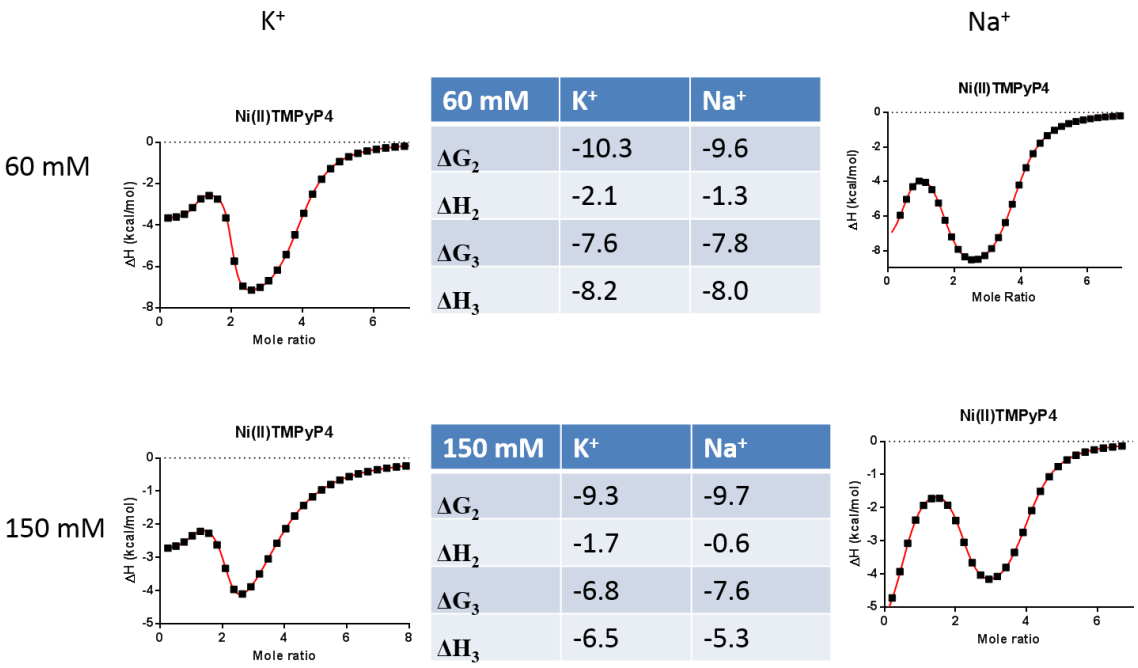

60 mM	K+	Na+
ΔG_2	-10.3	-9.6
ΔH_2	-2.1	-1.3
ΔG_3	-7.6	-7.8
ΔH_3	-8.2	-8.0

150 mM	K+	Na+
ΔG_2	-9.3	-9.7
ΔH_2	-1.7	-0.6
ΔG_3	-6.8	-7.6
ΔH_3	-6.5	-5.3

Figure A.21 Representative ITC titration enthalpogram for the titration of Ni-TMPyP4 into hTel22 in 60 or 150 mM Na^+ or K^+ BPES buffer.

Changes Gibbs free energies and enthalpies are given in kcal/mol.

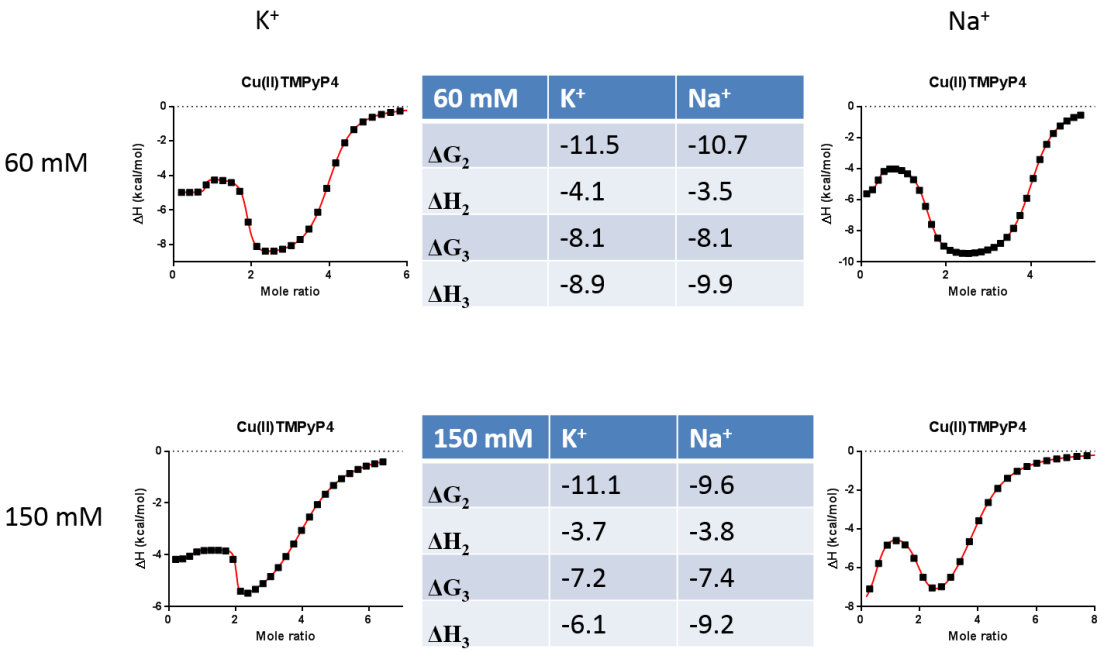

60 mM	K+	Na+
ΔG_2	-11.5	-10.7
ΔH_2	-4.1	-3.5
ΔG_3	-8.1	-8.1
ΔH_3	-8.9	-9.9

150 mM	K+	Na+
ΔG_2	-11.1	-9.6
ΔH_2	-3.7	-3.8
ΔG_3	-7.2	-7.4
ΔH_3	-6.1	-9.2

Figure A.22 Representative ITC titration enthalpogram for the titration of Cu-TMPyP4 into hTel22 in 60 or 150 mM Na^+ or K^+ BPES buffer

Gibbs free energies and enthalpies are given in kcal/mol.

A.3 Circular dichroism spectra for titrations

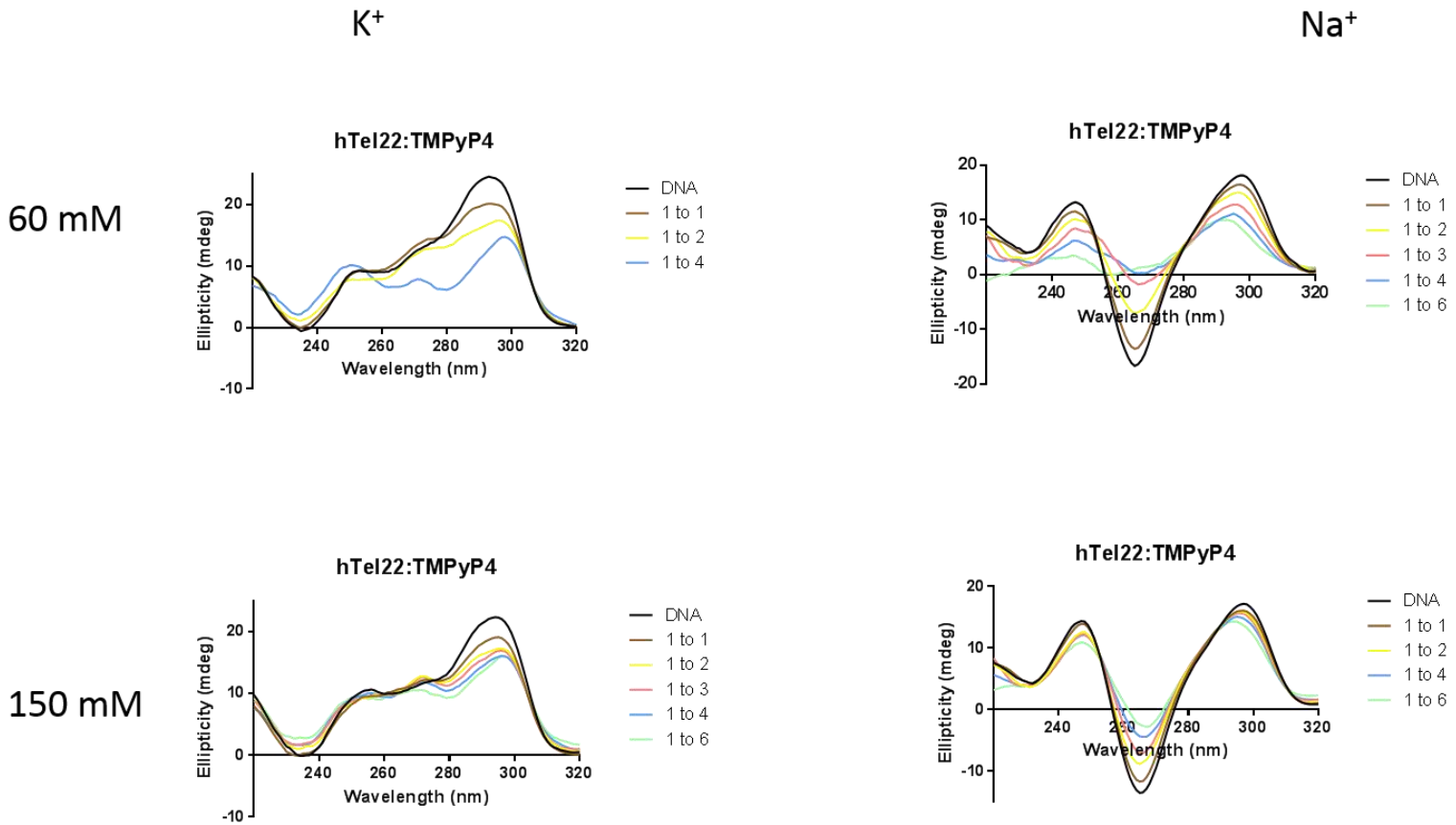

Figure A.23 CD spectra for the titration of TMPyP4 into hTel22 in either 60 or 150 mM Na^+ or K^+ BPES.

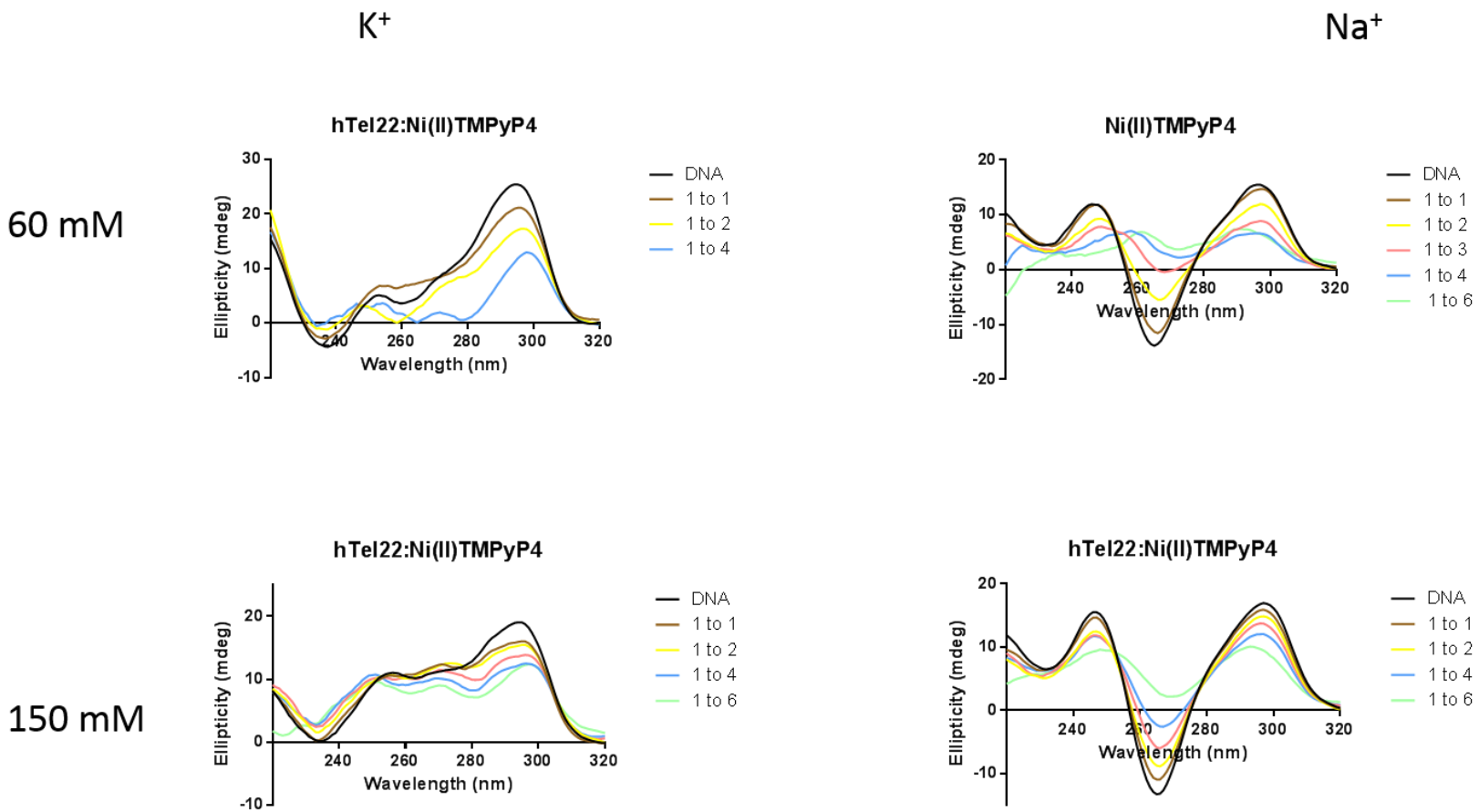

Figure A.24 CD spectra for the titration of Ni-TMPyP4 into hTel22 in either 60 or 150 mM Na^+ or K^+ BPES.

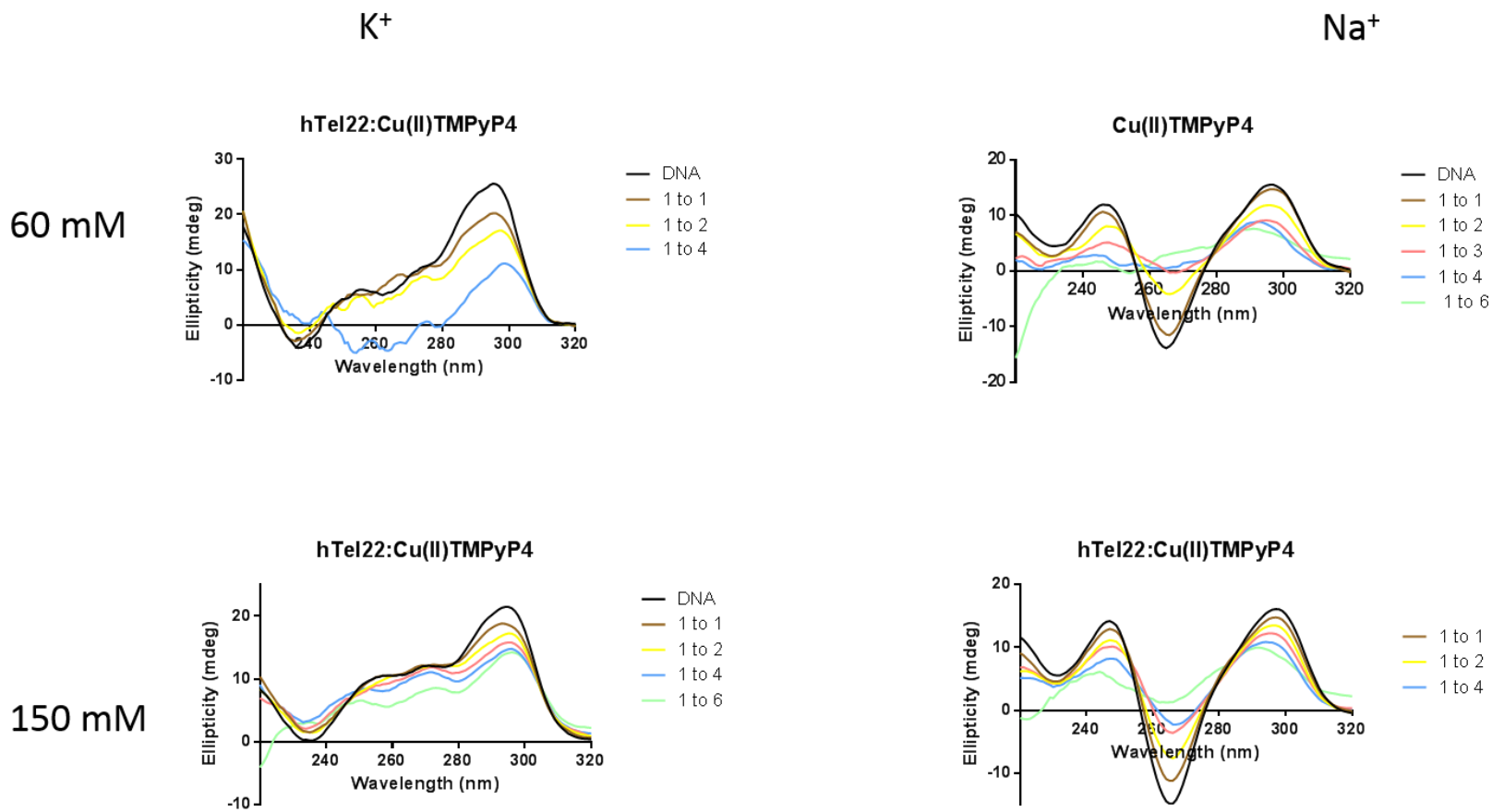

Figure A.25 CD spectra for the titration of Cu-TMPyP4 into hTel22 in either 60 or 150 mM Na^+ or K^+ BPES.

APPENDIX B

SUPPLEMENTARY INFORMATION FOR CHAPTER IV

B.1 ITC final figures

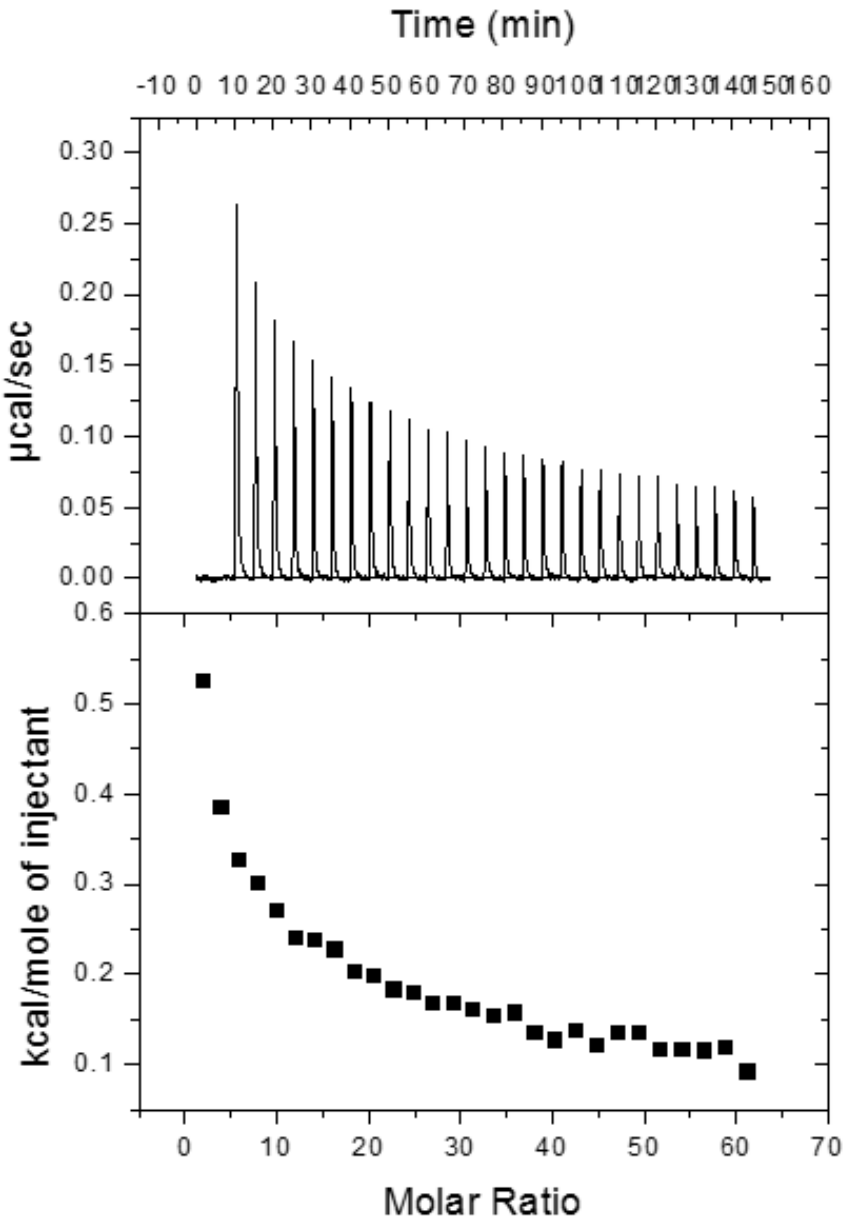

Figure B.1 Representative ITC titration profile for the titration of **MP** into tris buffer.

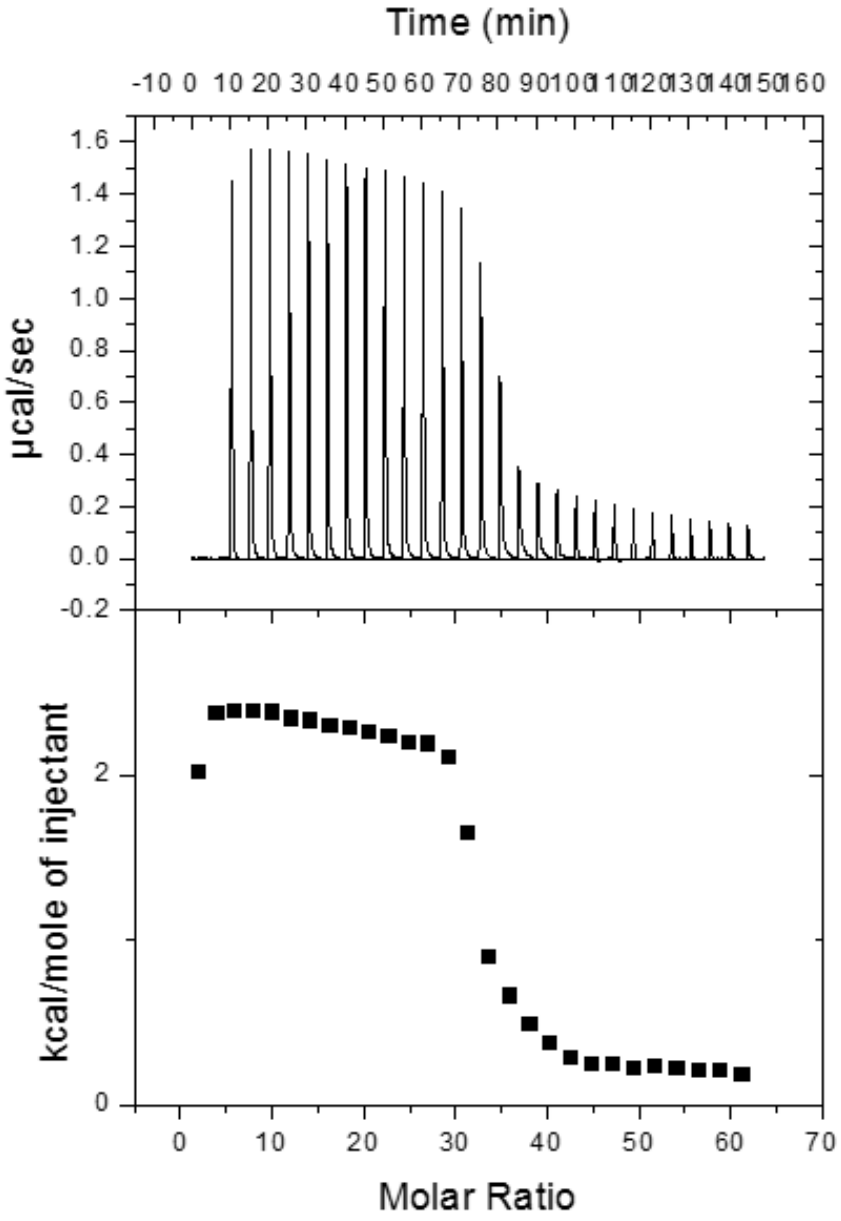

Figure B.2 Representative ITC titration profile for the titration of **MP** into 25 bp duplex DNA in tris buffer.

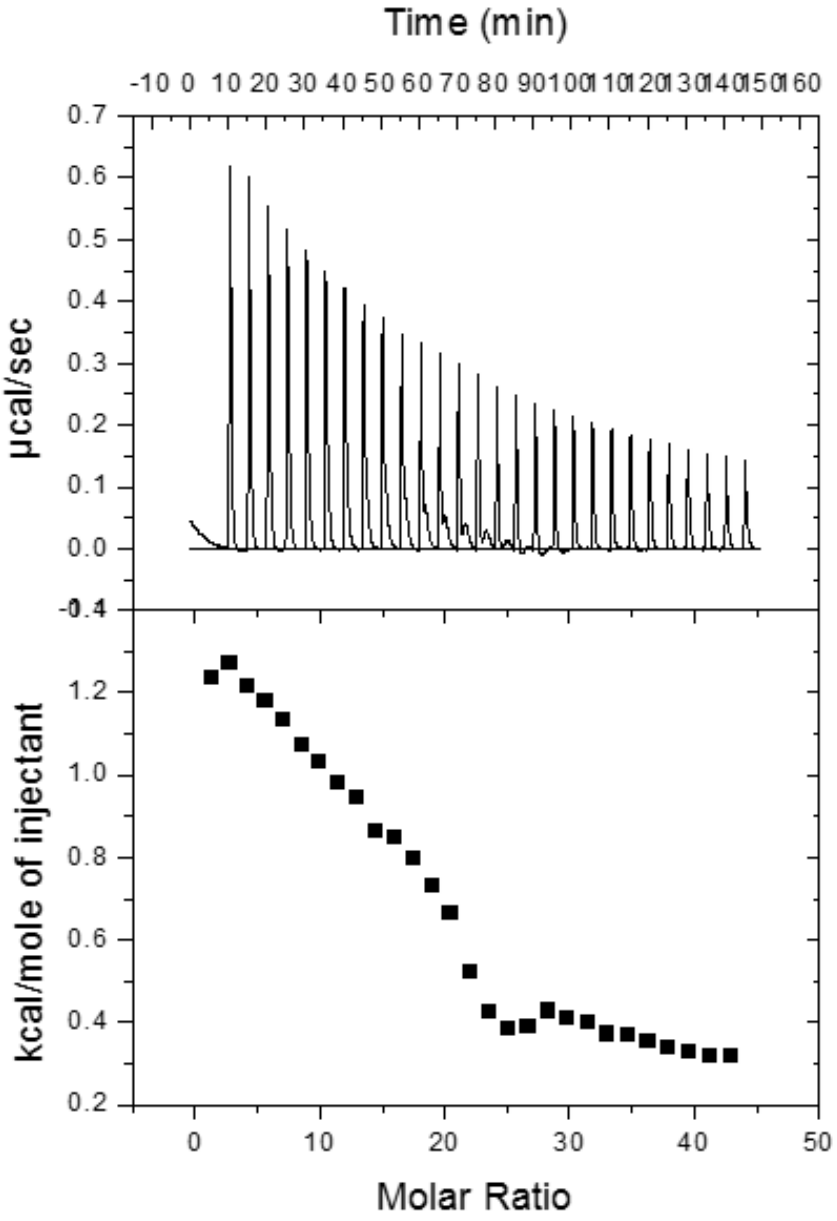

Figure B.3 Representative ITC titration profile for the titration of **Rp2d** into tris buffer.

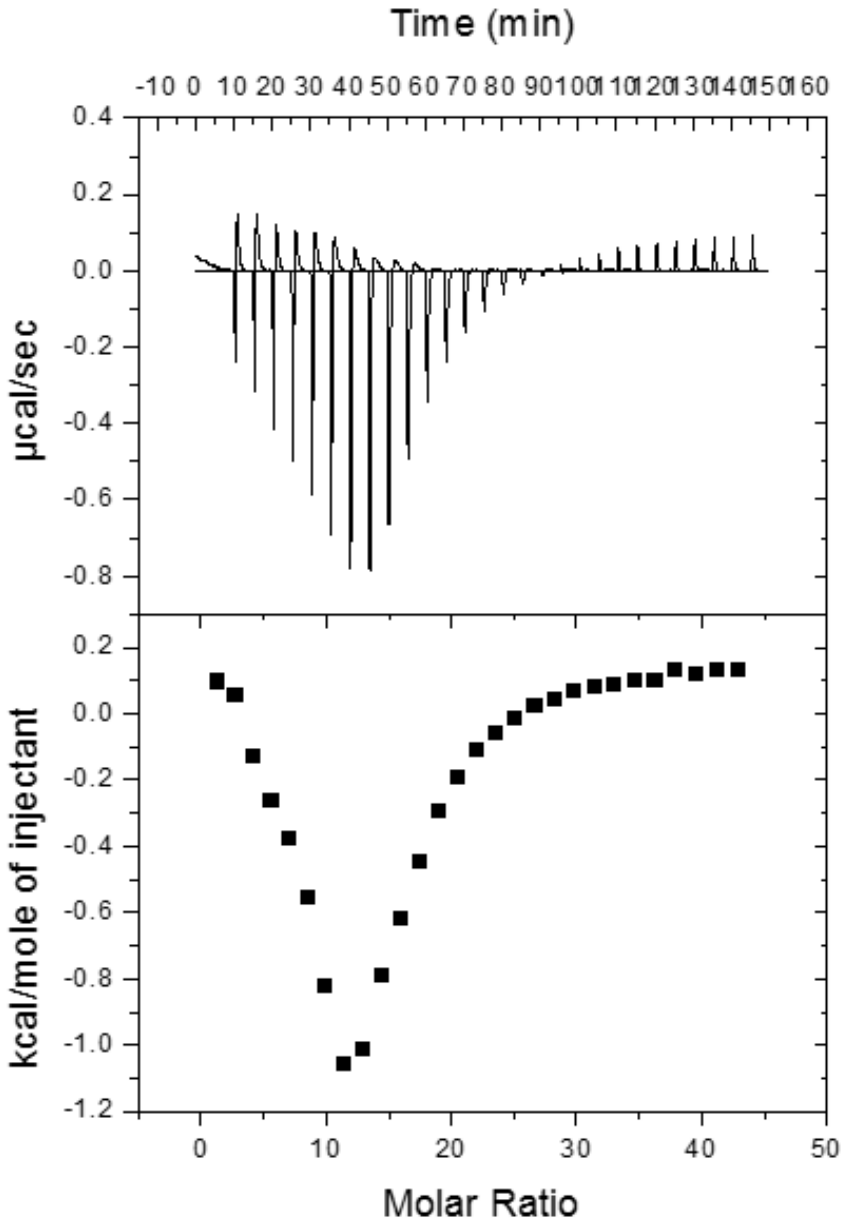

Figure B.4 Representative ITC titration profile for the titration of **Rp2d** into 25 bp duplex DNA in tris buffer.

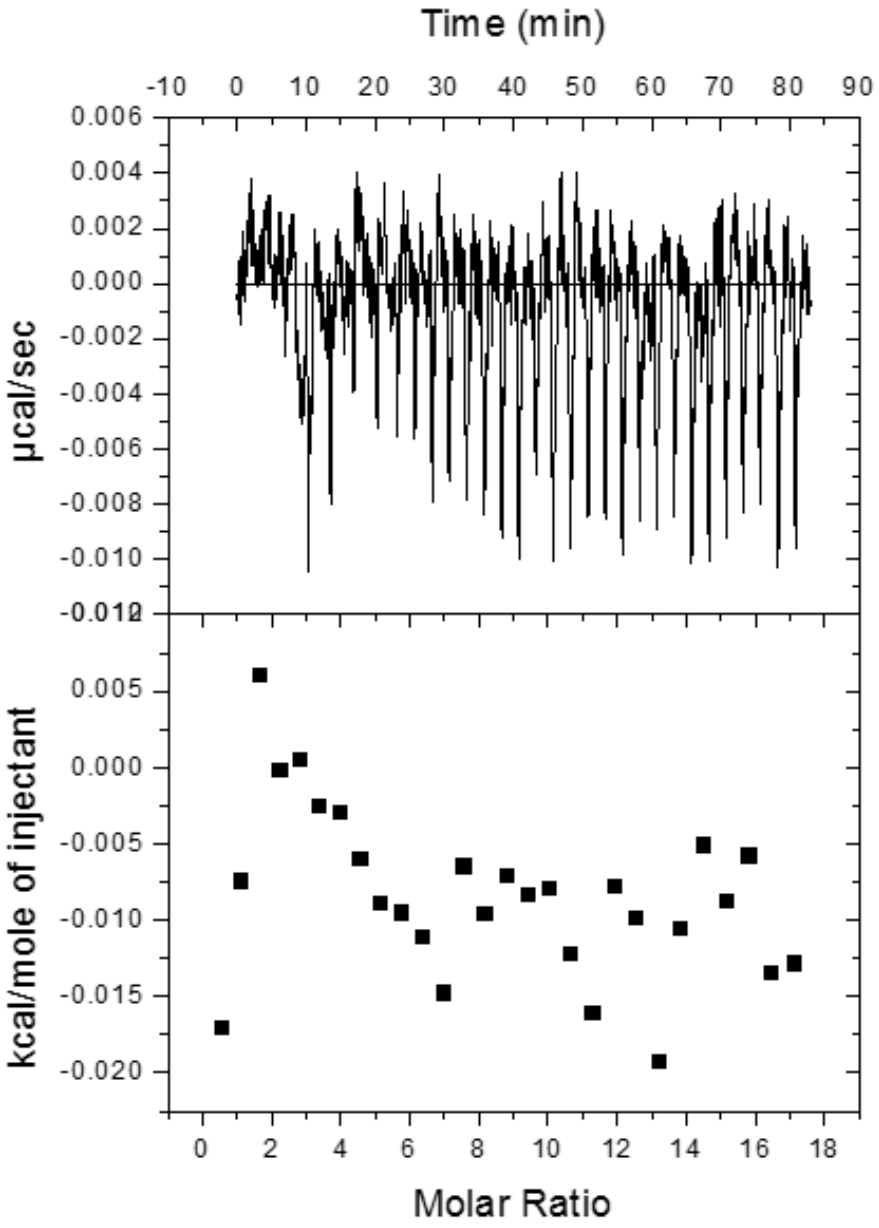

Figure B.5 Representative ITC titration profile for the titration of **Rp3** into tris buffer.

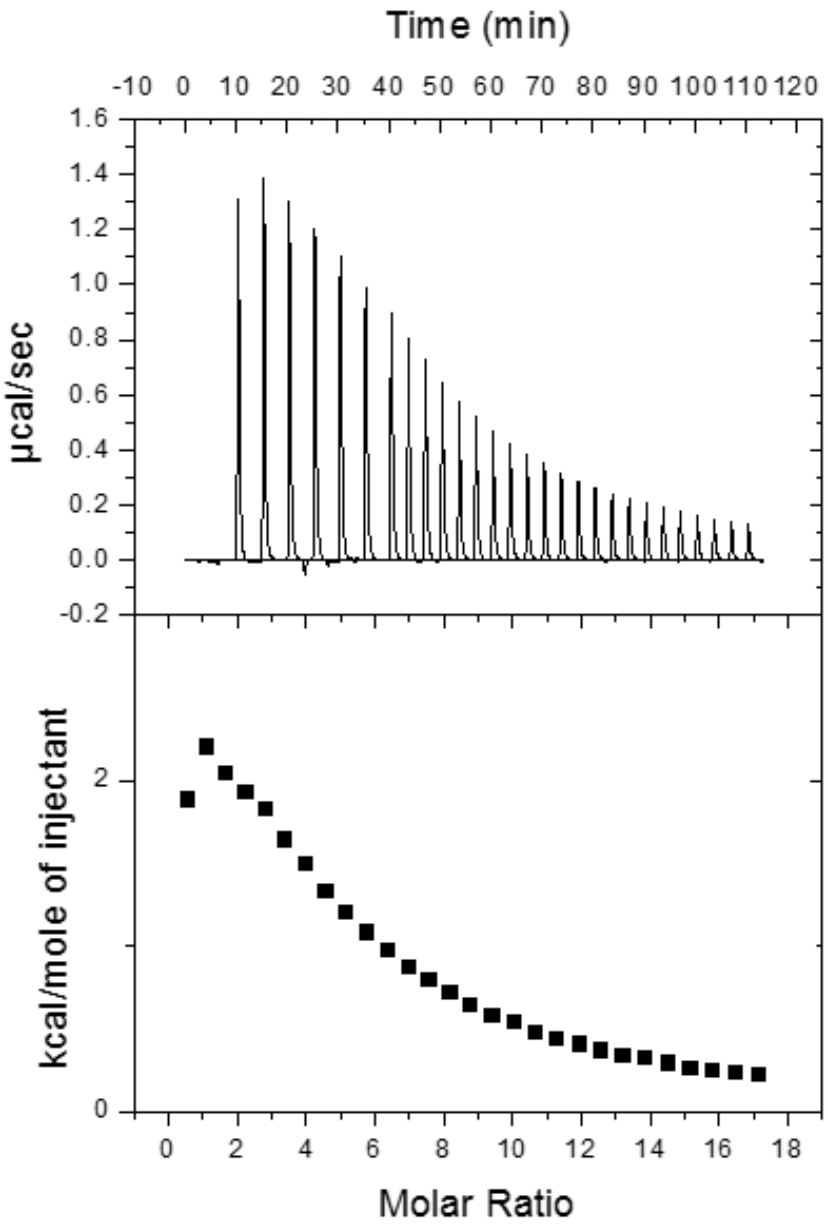

Figure B.6 Representative ITC titration profile for the titration of **Rp3** into 25 bp duplex DNA in tris buffer.

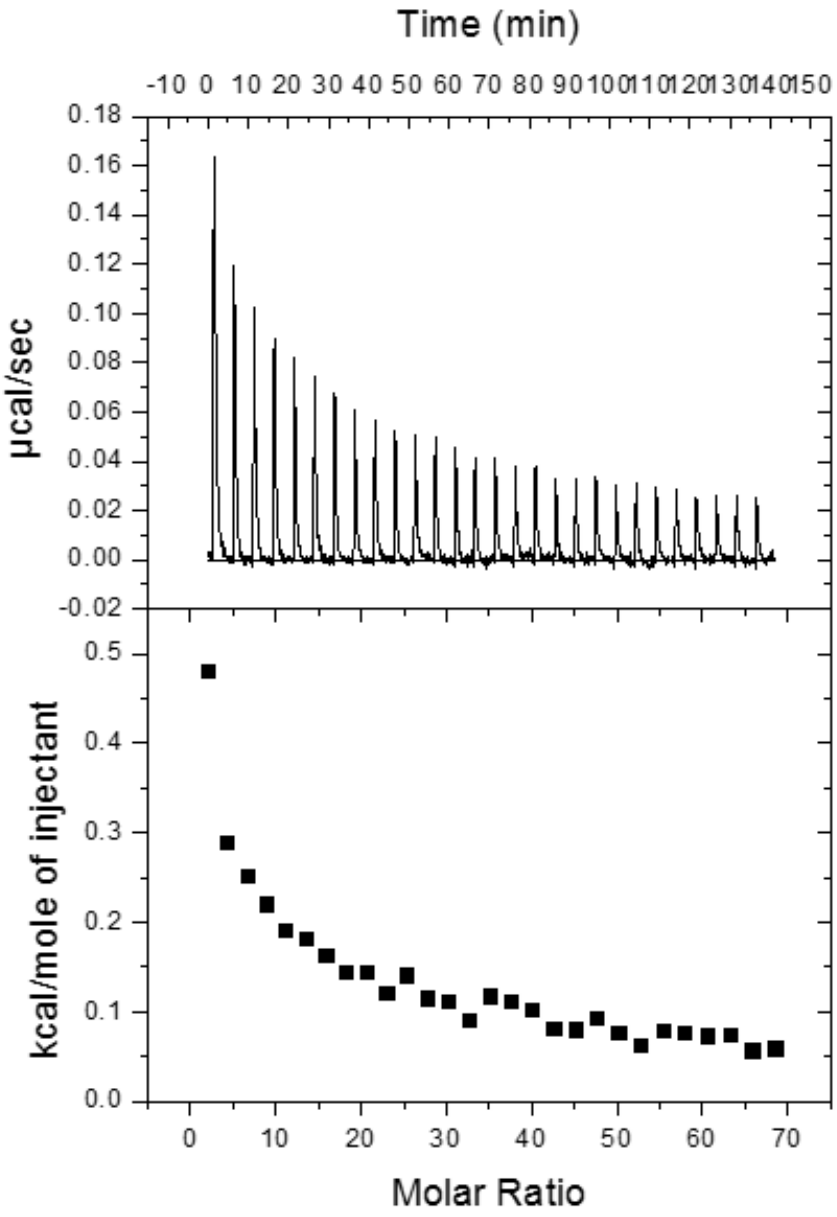

Figure B.7 Representative ITC titration profile for the titration of **MP** into Na^+ BPES buffer.

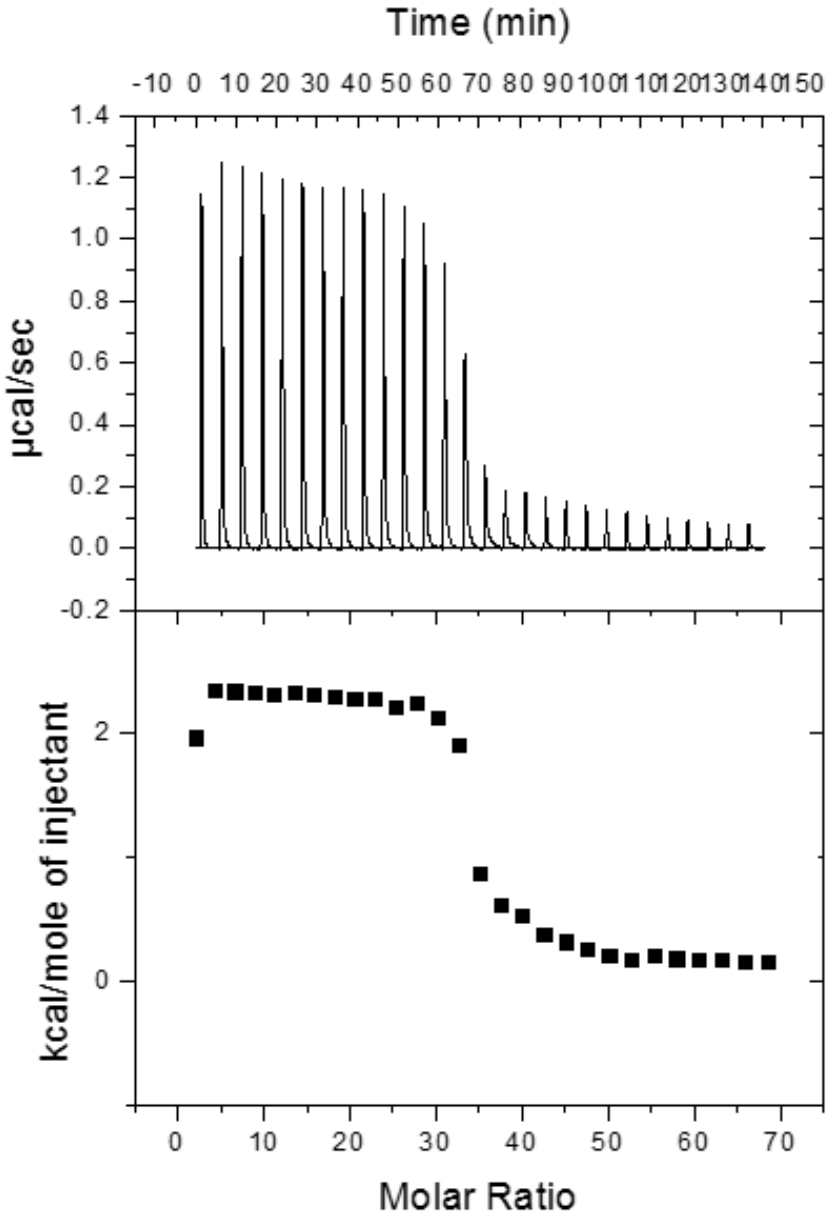

Figure B.8 Representative ITC titration profile for the titration of **MP** into 25 bp duplex DNA in Na^+ BPES buffer.

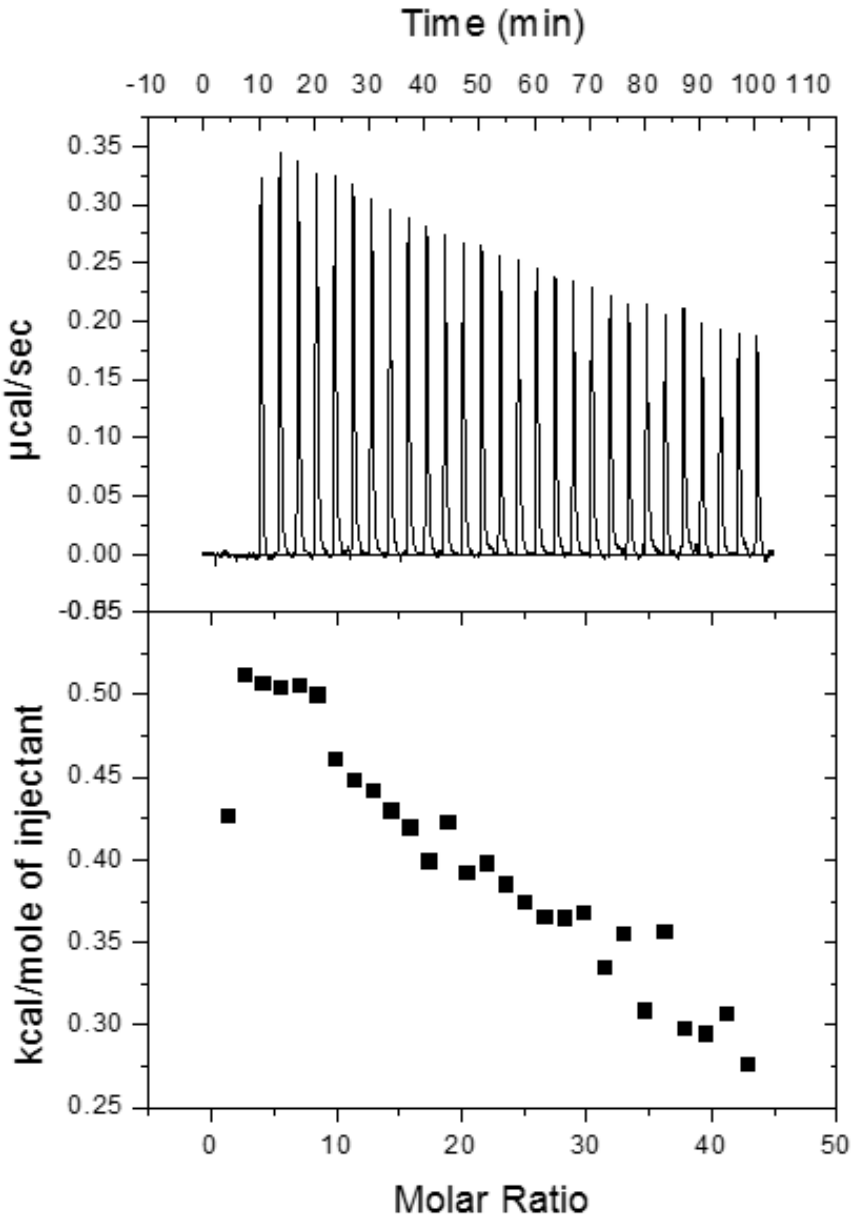

Figure B.9 Representative ITC titration profile for the titration of **Rp2d** into Na^+ BPES buffer.

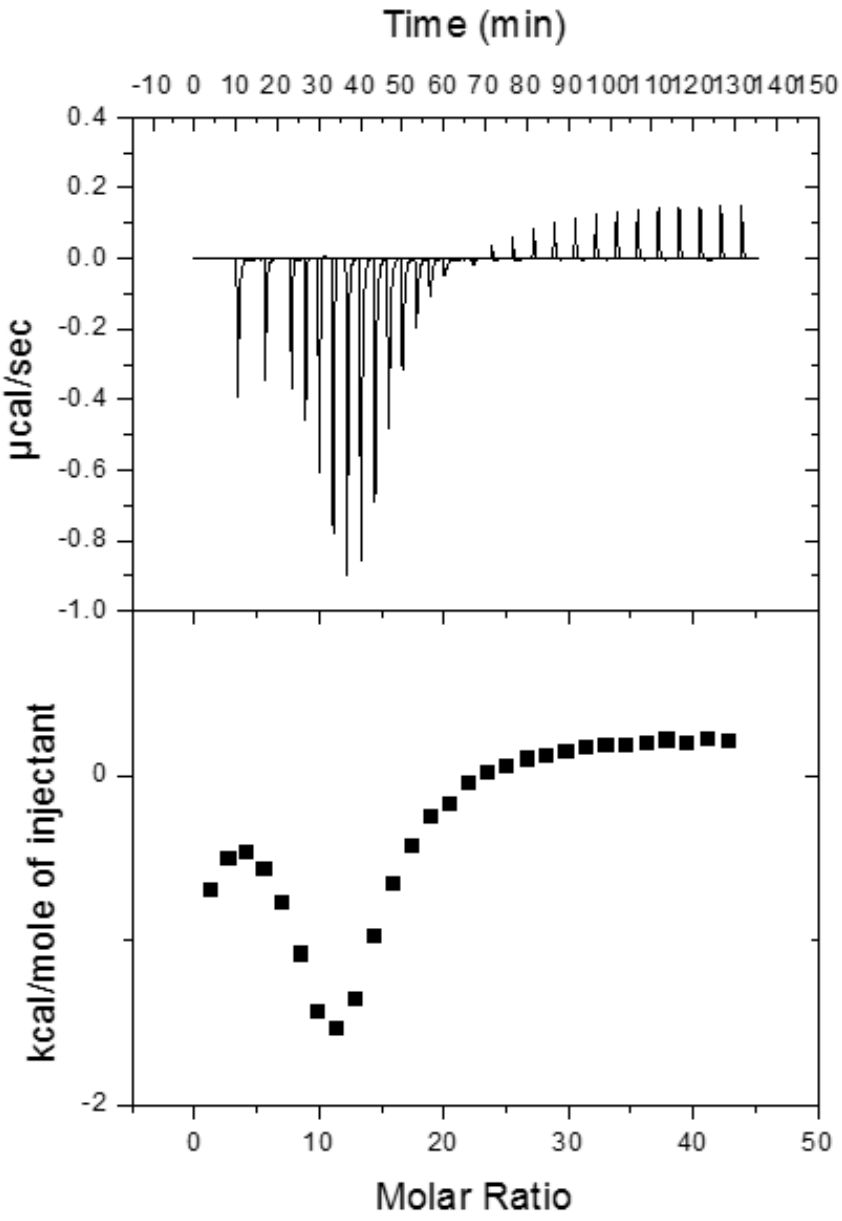

Figure B.10 Representative ITC titration profile for the titration of **Rp2d** into 25 bp duplex DNA in Na^+ BPES buffer.

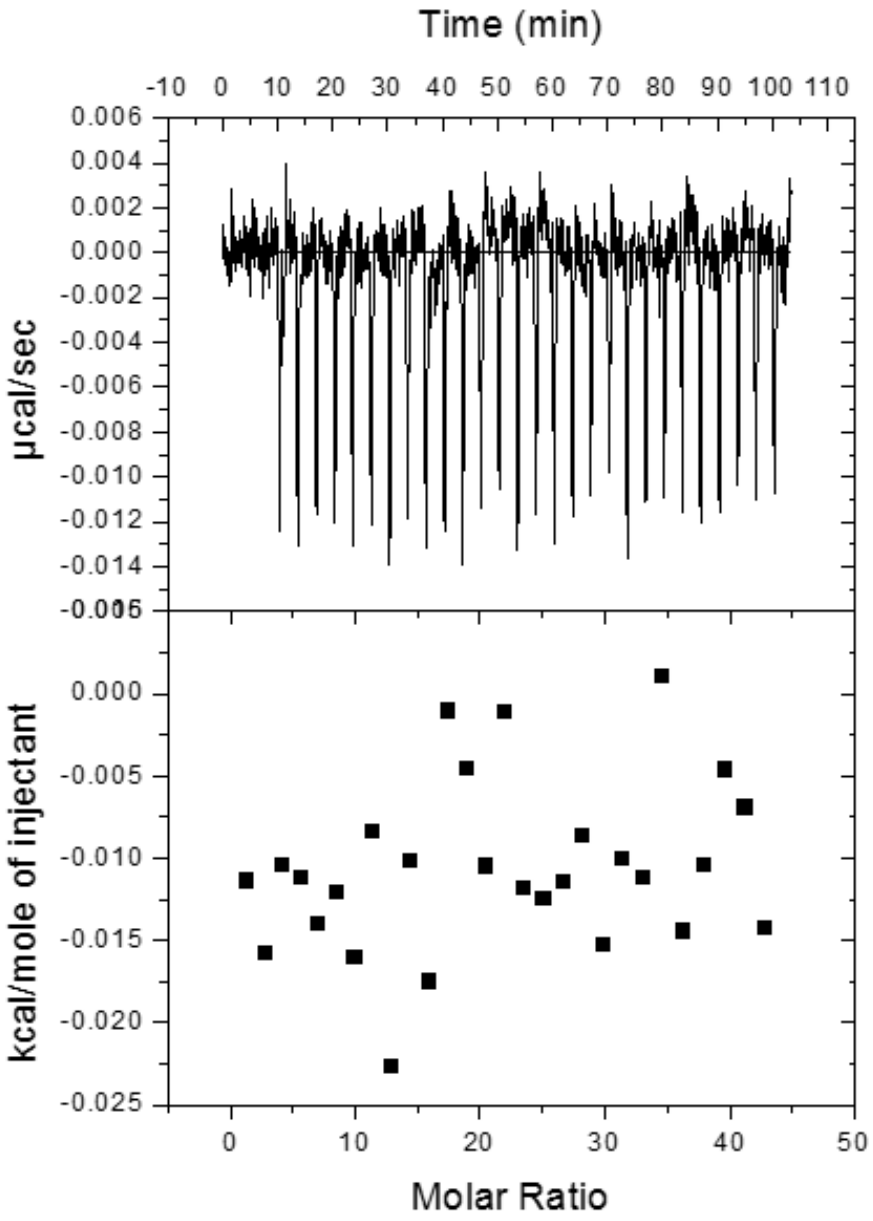

Figure B.11 Representative ITC titration profile for the titration of **Rp3** into Na^+ BPES buffer.

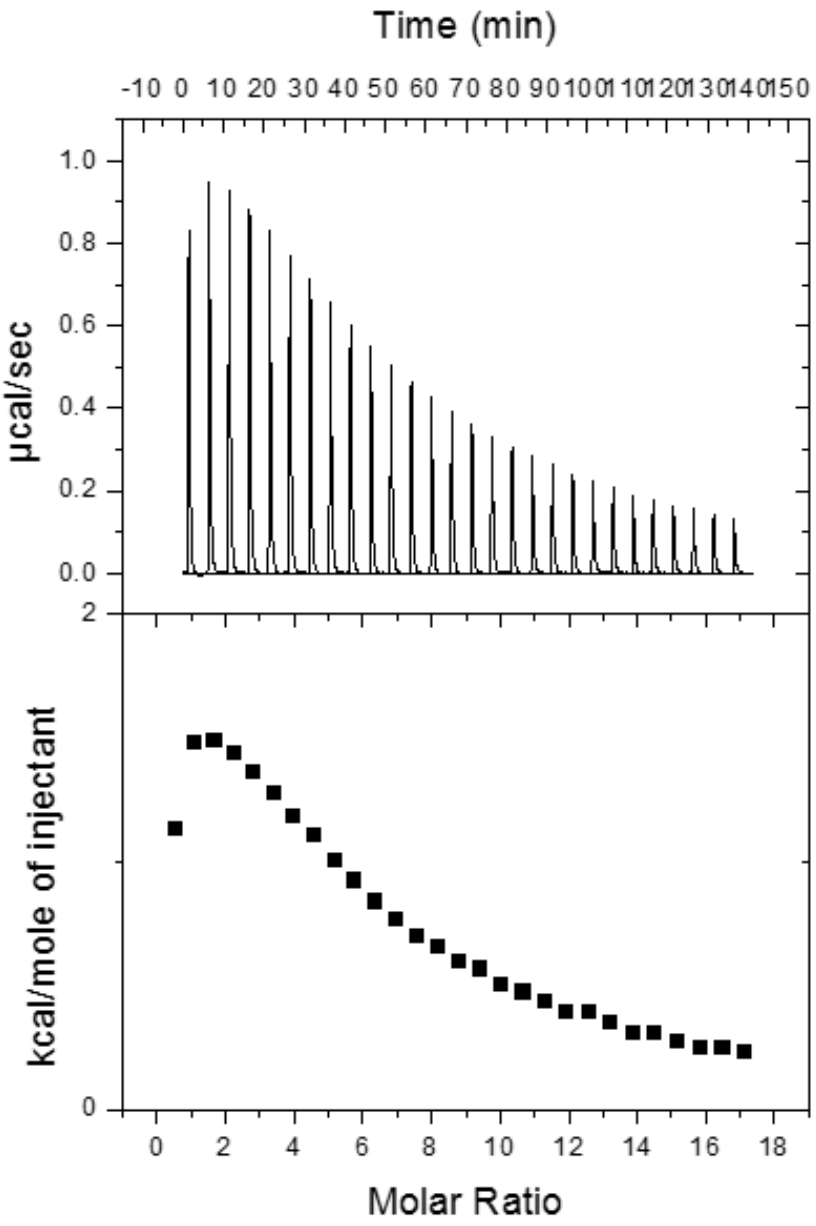

Figure B.12 Representative ITC titration profile for the titration of **RP3** into 25 bp duplex DNA in Na^+ BPES buffer.

B.2 Circular dichroism spectra for titrations

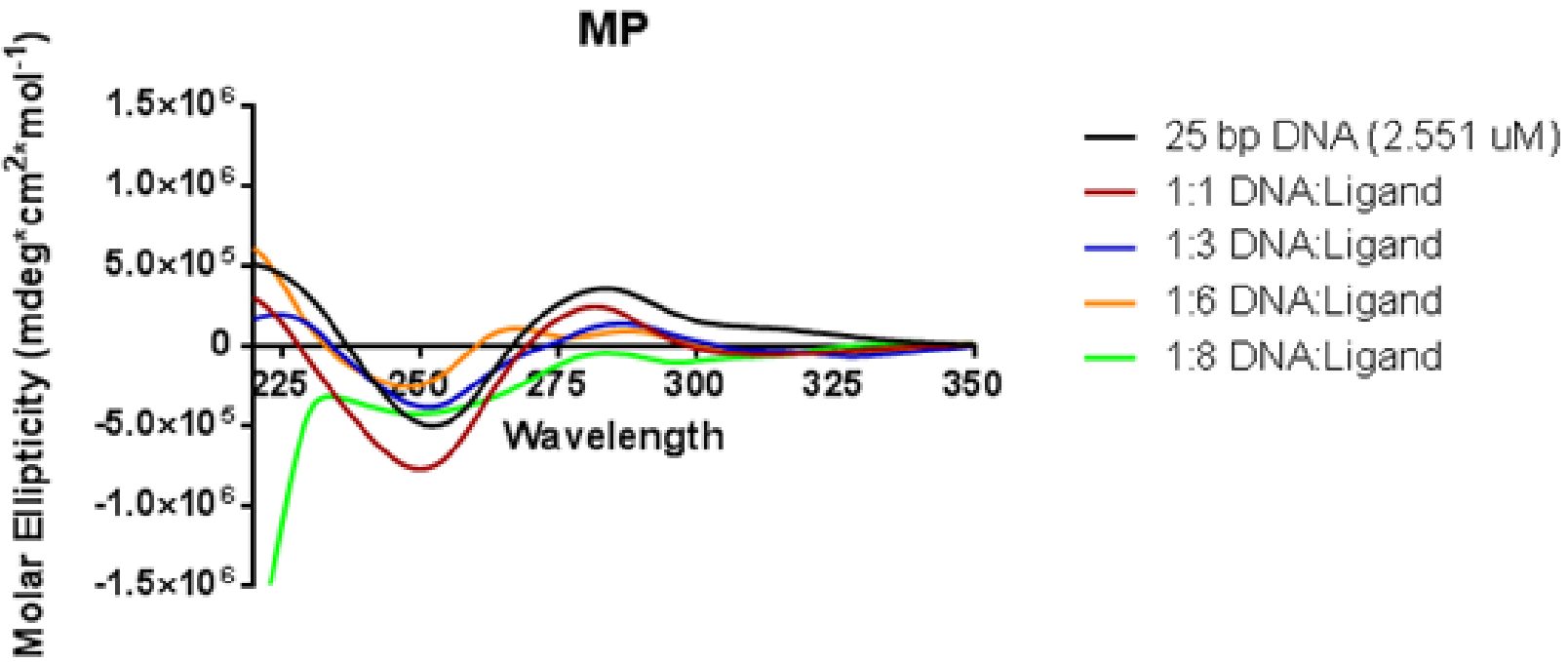

Figure B.13 CD spectra for the titration of **MP** into duplex DNA in Na^+ BPES buffer.

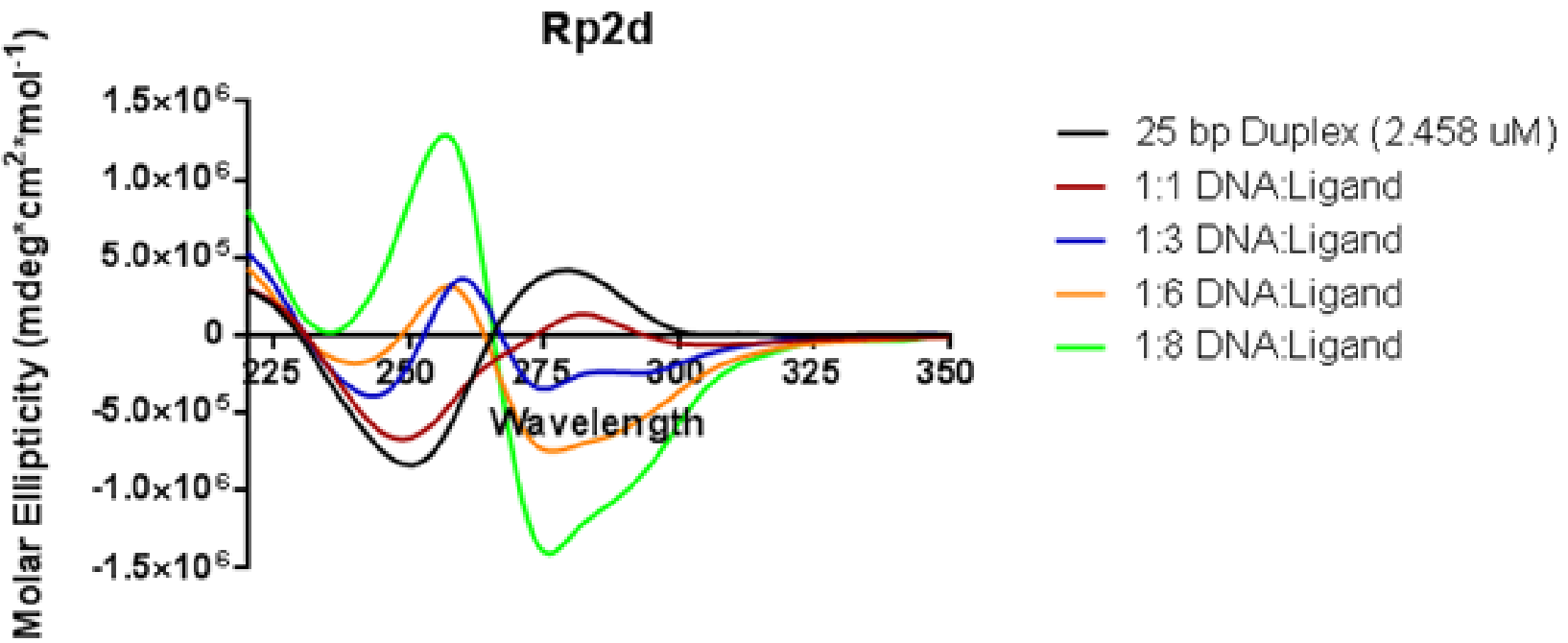

Figure B.14 CD spectra for the titration of **Rp2d** into duplex DNA in Na^+BPES buffer.

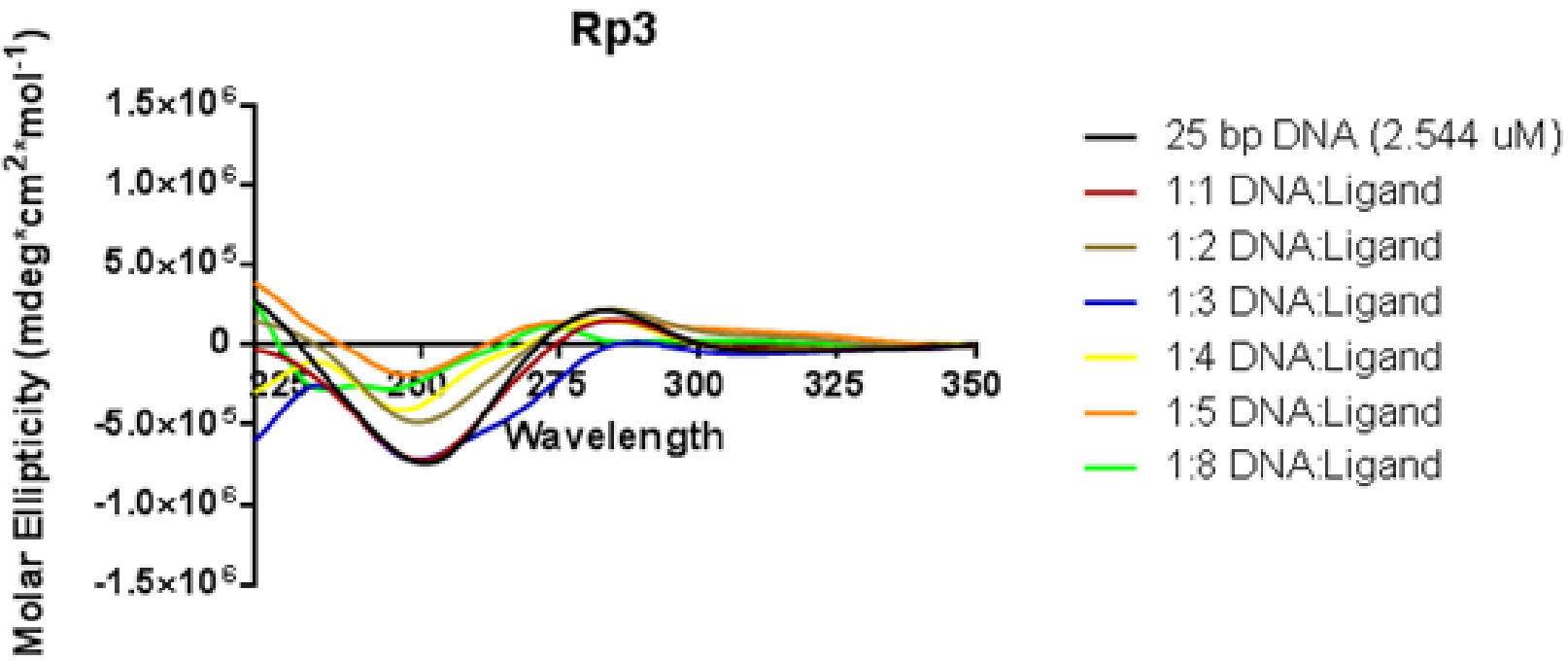

Figure B.15 CD spectra for the titration of **Rp3** into duplex DNA in Na^+BPES buffer.

Table B.1 Thermodynamic Data obtained from ITC Experiments performed at 298 K for the interactions between ligands and 25bp duplex in tris buffer.

Ligand	K_{a1} ($x10^{-5}$ M^{-1})	ΔG_1 (kcal/mol)	ΔH_1 (kcal/mol)	$-T\Delta S_1$ (kcal/mol)	K_{a2} (kcal/mol)	ΔG_2 (kcal/mol)	ΔH_2 (kcal/mol)	$-T\Delta S_2$ (kcal/mol)
MP	81 ± 9	-9.4 ± 0.1	5.3 ± 0.1	-14.8 ± 0.1				
Rp2d	13 ± 4	-8.3 ± 0.2	-1.1 ± 0.1	-7.2 ± 0.1	3.6 ± 0.6	-6.2 ± 0.1	-10 ± 2	-4 ± 3
Rp3	0.1 ± 0.01	-5.5 ± 0.1	2.5 ± 0.3	-8.0 ± 0.3				
P^{4+} (13)	1.7 ± 0.8	-7.1 ± 0.3	2.6 ± 0.4	-9.7 ± 0.7				